Unraveling Optoelectronic Properties of 2D Materials

Andreij de Carvalho Gadelha

May 2019

Universidade Federal de Minas Gerais - UFMG
Instituto de Ciências Exatas - ICEx
Programa de Pós Graduação em Física

Unraveling Optoelectronic Properties of 2D Materials

Andreij de Carvalho Gadelha

Supervisor: Prof. Dr. Leonardo Cristiano Campos
Co-supervisor: Prof. Dr. Rodrigo Gribel Lacerda

Thesis presented to UNIVERSIDADE FEDERAL DE MINAS GERAIS, as a partial requisition to obtain the Ph.D. degree in physics.
Research Field: Condensed Matter Physics.

May 2019

I dedicate this thesis to the grown-up children, that
when young, dreamed of becoming scientists.
In memory of Josué Mendes Filho.

Acknowledgements

I am grateful to the universe and its forces that shaped a beautiful existence. I am also thankful to my father who helped me so far and will persist at my side. I am grateful to my parents, Jorge Gadelha, and Izabel Carvalho. I want to thank my grandmother Maria Isabel da Silva Gadelha for all the support and care. I am thankful for Jorge Gadelha for being an example of father and friend. I am pretty grateful to Maria Lúcia for all the help, diligence and carefulness.

I am pleased to some important people that gave me crucial advices during my life, helping me choose the right path. I am very thankful to Raul Correa. In memory of Josué Mendes Filho, I have no words to thank him, who was my first example of being a scientist. He was crucial for the path that I chose.

I have now words to thank my supervisor Leonardo Campos, that is a great example of an excellent person and superb scientist. He walked beside me for the last six years in good and bad times, assisting and showing me the way of being a great scientist. I am grateful to my co-supervisor Rodrigo Gribel Lacerda for the assistance and allowing working at the Laboratório de Nanomateriais. I want to thank Sergio Oliveira for the willing of helping, for the friendship and for being a wonderful person. I am grateful to all my friends, professors and staff from UFMG.

I am thankful to Eduardo Bedê Barros, who was my first co-supervisor, and to all friends, professors, and staff from UFC.

I am pleased to Leandro Malard Moreira and Ana Maria de Paula for the excelent collaboration. I also thank Egleidson, Thonimar, Mychel, Cassiano, Hudson, Lucas, Filomeno for aiding me. I also thank Ado Jório and Luiz Gustavo Cançado for receiving me at the laboratory of nanoespectroscopy.

I am grateful to Gustavo Safar, Helio Chacham, Marcio Daldin Teodoro, and Alexandre Pachoal for examining my thesis.

I am thankful to Rafael Gontijo for being willing to collaborate and to do measurements. I am also grateful to Eliel Gomes for the friendship and for working overnight supporting me. I am pleased to Cristiano Fantini and Ariete Righi. I am thankful to Thales Fernandes, Ana Paula and Bernardo Neves for the collaboration.

I am very thankful to Klaus Krambrock, Bruno Cordeiro, Hélio Chacham and Ananias Alencar for the discussions and collaborations.

I want to thank Juan Carlos González for the discussions in physics.

I want to thank Ramon de Oliveira Aranda, Luis Rodrigues Armôa Garcia, and Marcio de Almeida Flores, for doing the WDS measurements. I want to thank Antônio de Pádua,

Thiago Perdigão Albergaria, Antônio Samuel Neves de Jesus, and Leandro Lemos Simões for the services.

I am pleased to Igor Aharonovich, who cordially invited me to stay one-month doing experiments at his lab, in UTS, Sydney (Australia). I am also thankful to Milos Toth, for the discussions in physics, and to Carlo Bradac, Mehran Kianinia, Toan Tran, Zaiquan Xu, Minh Nguyen, Ngoc My Hanh Duong, Simon White, Noah Mendelson, Blake, Jackie, and all good friends that made my visit in Australia wonderful.

I am grateful to Ingrid Barcelos and Alisson Cadore for help, advice, and guidance.

I want to thank my colleagues and friends Thiago Graziano, Ingrid Barcelos, Alisson Cadore, Cintia Lima, Natália Rezende, Edrian Mania, Gustavo Ferrari, Leonel Muniz, Igor Antoniazzi, Vinícius Ornelas, Thiago Amarante, Thiago Carvalho, Luam, Ana Paula Grabi, Maria Clara, and Marcos for the friendship.

I appreciate FAPEMIG, CAPES, CNPQ/MCT, INCT/Nanocarbono, Petrobrás, BNDS, CBPF, CCS, Pós-graduação em Física and Pró-Reitoria de pesquisa da UFMG, FAPERJ for the funding.

"The most beautiful thing we can experience is the mysterious. It is the source of all true art and science" (Albert Einstein)

"In all things of nature there is something of the marvelous" (Aristoteles)

Resumo

Os materiais 2D emergiram como uma excelente plataforma para investigar fenômenos optoeletrônicos. Por outro lado, o emprego de campos elétricos externos na matéria revela fenômenos físicos intrigantes. Neste trabalho, modificamos as propriedades optoeletrônicas de materiais 2D, MoS_2 e talco, por campo elétrico, revelando possibilidades e efeitos interessantes. No MoS_2, da ação combinada de aplicações de campos elétricos e exposições a luz, obtemos um efeito de fotomemória, que é não-volátil, ajustável com tensões de gate, e é obtida numa arquitetura simples. A fotomemória deve-se à modulação com a tensão de gate da fotocorrente persistente em transistores de MoS_2. Este efeito, por sua vez, é completamente ajustável com a tensão de gate. Desta forma, aplicamos tensões de gate, durante as exposições com luz, para "gravar" estados de memória distintos, com possibilidades para memória multiníveis. Por outro lado, nós também utilizados a tensão de gate, com a luz desligada, para ajustar os ganhos de memória. Além disso, prevemos que nossos dispositivos armazenam a informação gravada por mais de dez anos, indicando uma memória do tipo não-volátil. Também propomos um modelo fenomenológico para explicar a fotomemória e a fotocorrente persistente, as quais atribuímos a um efeito de fotodopagem. Concluímos esta parte mostrando que a fotodopagem modifica a distribuição espacial da fotocorrente. Logo após, realizamos uma investigação inovadora de emissões de defeitos no talco 2D do tipo atômica. Utilizamos o campo elétrico para controlar estas emissões por dois mecanismos. Primeiramente, deslocamos as energias das emissões por um efeito Stark linear. Ao investigar este fenômeno, nós adquirimos um entendimento da natureza dos defeitos no talco. Além disso, o campo elétrico pode controlar a intensidade das emissões, o que leva a uma aniquilação reversível de algumas destas. O efeito de aniquilação das emissões possui ricas interpretações físicas, portanto nós as discutimos e elaboramos qual mecanismo descreve melhor nossos resultados. Em resumo, nosso trabalho aborda novas e excitantes possibilidades de estudar e controlar as propriedades optoeletrônicas dos materiais 2D.

Keywords: Optoelectronics, 2D Materials, Memory devices, Persistent photocurrent, Photodoping, Photoluminescence, Defects, Stark effect, PL quenching, MoS_2, Talc

Abstract

2D materials have emerged as an exciting platform to investigate optoelectronics phenomena. On the other hand, the employment of external fields in matter reveals intriguing physical effects. Here, we tune the optoelectronic properties of 2D materials, MoS_2 and talc, by applying electric fields, unraveling interesting possibilities. In MoS_2, from the combined actions of electric field applications and laser exposures, we obtain a photomemory effect, which is non-volatile, gate-tunable, and is obtained in a simple architecture. The photomemory is due to a modulation with the gate voltage of the persistent photocurrent in MoS_2 transistors. This effect, in turn, is entirely gate-tunable. In this way, we use gate voltages, during laser exposures, to "record" distinct photomemory states, with possible applications for multilevel memories. On the other hand, we can also use the gate voltage, with the laser off, to adjust the memory gains. Furthermore, we predict that our devices store the photomemory information for more than ten years, indicating a non-volatile memory effect. We also propose a phenomenological model to explain the photomemory and the persistent photocurrent, which we ascribe to a photodoping effect. We conclude this part by showing that the photodoping modifies the spatial distribution of the photocurrent. Next, for the first time, we investigate atomic-like photoluminescence emissions from defect states in 2D talc. We use the electric field to control these emissions by two different mechanisms. First, we can shift the energies of the emissions by a linear Stark effect. By further investigating this phenomenon, we get an insight into the nature of the defects in talc. Besides, the electric field can control the intensity of the emissions, leading to a reversible annihilation of some of the photoluminescence peaks. This quenching effect has rich physical explanations, so we discuss them, and from our interpretations, we elaborate which mechanism describes better our results. In summary, our work uncovers exciting and novel possibilities to study and control the optoelectronics of 2D materials.

Keywords: Optoelectronics, 2D Materials, Memory devices, Persistent photocurrent, Photodoping, Photoluminescence, Defects, Stark effect, PL quenching, MoS_2, Talc

Contents

Resumo **I**

Abstract **II**

List of Figures **VI**

1 Introduction to the thesis **1**

I Unraveling photocurrent and photodoping effects in MoS_2 transistors **5**

2 Theory **6**

2.1 Introduction to MoS_2 . . . 6
2.2 Field effect transistors . . . 9
2.3 Photocurrent . . . 11
2.4 Memory . . . 14

3 Methods and characterizations **21**

3.1 Sample preparation . . . 21
3.2 Optical characterization . . . 25
3.3 Electrical characterization . . . 30
3.4 Photocurrent setup . . . 33

4 Results and discussion **35**

4.1 The photomemory effect . . . 35
4.2 The mechanism of the photomemory effect . . . 39
4.3 The photomemory performance . . . 42
4.4 The photodoping in the MoS_2/SiO_2 device . . . 45
4.5 Local photodoping . . . 49

5 Partial conclusions **52**

II Unraveling Stark and quenching effects of atomic-like emissions in layered talc devices **53**

6 Theory **54**
6.1 Introduction to talc 54
6.2 Photoluminescence 58
6.3 Photoluminescence under non-trivial electrostatic conditions 60
6.3.1 Stark effect 60
6.3.2 Photoluminescence quenching 62

7 Methods and characterizations **64**
7.1 Sample preparation 64
7.2 X-ray diffraction 66
7.3 Raman spectroscopy 66
7.4 Wavelength-dispersive X-ray spectroscopy 69
7.5 Photoluminescence setup 70

8 Results and discussion **72**
8.1 Atomic-like emission in talc 72
8.2 Effects of electric field applications in the photoluminescence of talc 77
8.2.1 Linear Stark splitting of the photoluminescence peaks 80
8.2.2 Quenching of the photoluminescence peaks 81

9 Partial conclusions **86**

10 General conclusions **87**

References **91**

List of Figures

2.1 Crystal structure of a TMDC . . . 7
2.2 The band structure of MoS_2 . . . 8
2.3 Field effect transistor . . . 10
2.4 Excitation and decay of photogenerated carriers . . . 12
2.5 Comparison of the photocurrent responses . . . 13
2.6 Evolution of memory over the time . . . 15
2.7 Comparing memory devices . . . 15
2.8 Memory components . . . 16
2.9 Electronic memories . . . 18

3.1 Transfer setup . . . 22
3.2 Preparing the MoS_2/BN Device . . . 23
3.3 Optial images of the devices . . . 24
3.4 AFM measurements . . . 25
3.5 Photoluminescence measurements . . . 26
3.6 Raman measurements . . . 27
3.7 Photoluminescence and Raman images . . . 29
3.8 Electrical measurements setup . . . 30
3.9 I_{SD} vs V_{SD} measurements . . . 31
3.10 σ vs V_{BG} measurements . . . 32
3.11 Setup for the photocurrent measurements . . . 33
3.12 Setup for the SPCM . . . 34

4.1 PPC and photodoping . . . 36
4.2 Gate-tunable photomemory . . . 38
4.3 Physical model for the photodoping . . . 40
4.4 Photodoping comparison using different laser excitation . . . 42
4.5 Memory parameters . . . 43
4.6 Response time . . . 45
4.7 Photodoping from the SiO_2/Si substrate . . . 46
4.8 Photodoping and the gate-insulator interface . . . 48
4.9 Spatial control of the photocurrent . . . 50

6.1 The crystal structure of a monolayer talc . . . 55

6.2 The crystal structure of talc 56
6.3 Electronic structure of talc 56
6.4 Talc crystals 57
6.5 Photoluminescence process 59

7.1 Preparing the talc device 65
7.2 Optical image of the talc device 66
7.3 X-ray characterization of talc 67
7.4 Raman spectrum of talc 67
7.5 Photoluminescence setup 70

8.1 PL emission from defect states 73
8.2 Fittings of the PL spectrum 74
8.3 PL spectra with different excitation lasers 74
8.4 Power dependence of the PL spectra 75
8.5 Electronic structure of talc with Fe impurities 76
8.6 PL spectra for different V_{BG} 77
8.7 Colormap of the normalized PL intensity as a function of V_{BG} and energy . . 78
8.8 PL energy as a function of the electric field 80
8.9 PL intensity as a function of the gate voltage 82
8.10 Prospects of an electrical photon switch application 84

Chapter 1

Introduction to the thesis

Optoelectronics is the study and application of electronic devices and systems that source, detect and control light [1]. Optoelectronic devices that source light convert electrical energy to light, for example, the semiconductor lasers and the light-emitting diodes (LEDs) [2]. On the other hand, by converting optical signals into electrical currents, the optoelectronic devices can also detect light. Photodetectors and photodiodes are examples of such devices [2]. The optoelectronics also study devices that control light, by manipulating its power, wavelength, phase or polarization with an electrical control signal. Electro-optic modulators, electroabsorption modulators, and acousto-optic modulators are examples of devices that manipulate light [2].

The optoelectronics phenomena arise when optical materials interact with electric fields, modifying their optics. The optical properties of solids are an interesting and diverse field of physics. It includes the diffraction, the refraction, the absorption, the emission, and the scattering, among others [3]. In optoelectronic devices, electric field applications modify one or more of these classical effects, unraveling new phenomena beyond them. The exciting possibilities that occur in optoelectronic devices also generate broad technological applications, as described above. In this way, optoelectronics is a fascinating research area that has impacts on science and technology.

2D materials are an attractive platform to study optoelectronics [4–6]. They are innately bidimensional systems, where their thickness is typically the size of an atom. 2D materials have a vast number of crystalline species with distinct properties, as graphene, which is a semi-metal [7], molybdenum disulfide (MoS_2), molybdenum diselenide ($MoSe_2$), tungsten disulfide (WS_2), tungsten diselenide (WSe_2), which are semiconductors [4], niobium diselenide ($NbSe_2$), that is a superconductor [8], boron nitride (BN), an insulator material [9] and chromium triiodide (CrI_3), a magnetic material [10], among others. Due to their

ultra-thin nature, the interactions of 2D materials with electric fields are strong, resulting in novel optoelectronic effects and high-performance optoelectronic devices. Besides, their mechanical properties allow the fabrication of flexible optoelectronic devices. In this direction, flexible and sensitive photodetectors, as well as flexible LEDs [11], using 2D materials have been proposed [12, 13]. Exotic optoelectronic phenomena have also been observed in 2D materials, like the valley hall effect, where an optoelectronic analog of the hall effect (a magnetic-induced voltage difference in the transverse direction of the current flow) emerges when MoS_2 devices absorb circularly polarized light [14].

In this thesis, we study two 2D materials, MoS_2 and the recently discovered 2D talc. We explore the modifications by electric field applications of the absorption and emission effects of MoS_2 and talc, respectively. In MoS_2, we detect light, converting it in memory states, which leads to a photomemory application. On the other hand, in talc, we control the light, by changing its energy and intensity, with possible applications in electro-optic modulators. We briefly discuss these aspects below, and next, we explain the structure of this thesis.

We study the absorption of photons in MoS_2 transistors, where the gate voltage produce electric fields. In this case, the MoS_2 channel is one of the elements that absorb photons in the device, generating excess electron-hole pairs, which transform into a photocurrent upon an electric field application. Furthermore, the photon absorption by the interface between the insulator and the material used for the gate (gate-insulator interface) of the MoS_2 transistor leads to a hole-trapping at this interface, which in turn generates doping in MoS_2 - a photodoping effect. We associate this effect with the persistent photocurrent effect, which origin is still under debate. To summarize, the optoelectronic properties that we study in MoS_2 are the photocurrent and the photodoping. We show that the photodoping is persistent, but we can modulate it by a simultaneous application of laser exposure and gate voltage. The modulation of the photodoping generates distinct persistent photocurrent states that are interpreted as memory states.

We apply optoelectronic properties of MoS_2 in a photomemory effect. The photomemory device is gate-tunable. In this way, we use the gate voltage, during laser exposures, to "record" photomemory states. We also show that gate voltage applications, with the laser off, can modulate the photomemory gains. Furthermore, the photomemory states are non-volatile, predicted to retain up to 50% of the "recorded" information for more than ten years. We propose a model, supported by experimental evidence, that explains the photodoping and photomemory effects. According to this model, the physics of these effects is contained in the gate-insulator interface. To reinforce this point, we show that by using MoS_2 in a different transistor, we continue observing a photodoping effect. So, the theory that we propose generalizes the photodoping and photomemory effects to other transistors, using different materials. Finally, we show how the photodoping generation in the gate-insulator interface controls the photocurrent generation in the MoS_2 channel spatially.

2D talc is a recent discovered two-dimensional insulator [15]. Here, we study emissions properties in this material under electric field applications. Because talc is an insulator, we stimulate emissions in this material by photoexciting it with photon energies smaller than its band gap energy. These subgap excitations induce electronic transitions in defect states

from talc. The decay of electrons in these states generates photoluminescence emissions that resemble atomic emissions. By applying transverse electric fields in talc, we manipulate the energy and intensity of these atomic-like emissions. The modification in the energy is due to a linear Stark effect. By inspecting these phenomena, we evaluate the dipole moments of the defects in talc and get a better understanding of their nature. In addition to the Stark effect analysis, we show some density functional theory calculations, revealing which atomic impurity can give emissions similar to the observed experimentally.

The electronic manipulation of the intensities of the emissions in talc leads to a reversible quenching of some of them. There are rich physical explanations for the photoluminescence quenching effect. We inspect each quenching mechanism and analyze which one better describe the results of talc. We also connect the quenching and Stark splitting effects. We show that there is a relation between the dipole moments of the defects in talc, evaluated from the Stark effect, and the possibility that their emissions are quenched or not with electric field applications. Finally, we argue that we can use the quenching effect to implement talc in photon switching devices.

The thesis has two parts. In part I, entitled "Unraveling photocurrent and photodoping effects in MoS_2 transistors", we describe the photocurrent and photodoping effects in MoS_2, with applications in a photomemory effect. In part II, entitled "Unraveling Stark and quenching effects of atomic-like emissions in layered talc devices", we present the Stark splitting and photoluminescence quenching of the atomic-like emissions in 2D talc, with possible applications in electro-optic modulators. Both parts have a theory chapter, which provides the background to understand the respective part. There are methods and characterizations chapters, which exposes the experimental methods, tools, and characterizations of the materials. We also show results and discussion chapters, where we present and analyze the experimental results of the parts. At the end of each part, we present a partial conclusions chapter, that show the conclusions of the respective work. Finally, at the end of the thesis, we present the general conclusions.

Chapter 2 presents the theory of part I. We start by introducing MoS_2, which is the primary 2D material that we study in this part. Then, we comment on the operation of the field effect transistor, which is the device where we explore optoelectronics of MoS_2. Next, we elaborate on the photocurrent effect, which is the essential optoelectronic phenomenon of part I. Latter, we explain the memory effects and operations, because we apply optoelectronics of MoS_2 in memory devices.

Chapter 3 presents the methods and characterizations of part I of the thesis. We start by describing the sample preparation, followed by the optical and electrical characterizations of the devices. We finish this chapter by explaining the optoelectronic setups that we use for the measurements.

Chapter 4 presents the results and discussion of part I. We start by showing the results of the photodoping and photomemory effects. Next, we present a possible physical mechanism that explains the photodoping and persistent photocurrent effects. Then, we elaborate on technical issues of the photomemory device, studying its performance. We also generalize the photomemory effect on other field effect transistors. Thus we also present photomemory

results of a different MoS_2 device. Finally, we show that the photodoping is a local effect, enabling a spatial control of the MoS_2 photocurrent.

Chapter 5 concludes part I of the thesis.

Chapter 6 presents the theory of part II of this thesis. We begin this chapter by introducing talc. Then, we explain the photoluminescence, which is the principal optical property that we study in part II. Finally, we discuss the Stark effect and the photoluminescence quenching, which are the optoelectronic effects that arise in our devices.

Chapter 7 shows the methods and characterizations of part II. We start by describing the preparation of talc devices. Then, we discuss the techniques that we use to characterize talc, which are the X-ray diffraction, the Raman spectroscopy, and the wavelength-dispersive X-ray spectroscopy. We finish this chapter by describing the setups that we use for the photoluminescence measurements.

Chapter 8 presents the results and discussion of part II. We begin this chapter by characterizing the atomic-like emissions in talc. After describing these photoluminescence emissions, we show how they modify upon electric field applications. Next, we investigate the Stark splitting of the emissions. Finally, we inspect the quenching of the photoluminescence peaks.

Chapter 9 presents the partial conclusions of part II of this thesis.

Finally, chapter 10 concludes this thesis.

Part I

Unraveling photocurrent and photodoping effects in MoS_2 transistors

Chapter 2

Theory

In this chapter, we explore the essential aspects needed to comprehend the part I of this thesis. First, we present a brief description of MoS_2, which is the crucial material of part I. Next, we expose the operation of the field effect transistor (FET) using 2D materials because the FET is the architecture of the photomemory effect. Later, we show some physical mechanisms that may explain the photocurrent generation in MoS_2, including the photoconductivity and some aspects of the persistent photocurrent (PPC). Finally, we deliberate on the memory phenomenon and some electronic devices that operate as memory devices.

2.1 Introduction to MoS_2

MoS_2 is a layered crystal from the transition metal dichalcogenides family (TMDCs). The materials belonging to this family have the chemical formula MX_2 - where M is a transition metal from the family IV, V or VI, from the periodic table, and X is a chalcogenide (S, Se or Te). The chemical bonding of these elements are of the type X-M-X, see Fig. 2.1. Members of the TMDCs possess a wide range of electronic properties. They can be conductors, superconductors, semiconductors, semimetals, among others [4–6]. In particular, the dichalcogenides that contain Molybdenum and Tungsten in its formula are semiconductors with a band gap that varies from the visible to the infrared [4]. The Bulk of the TMCDs have several types of crystal structures, regarding the relative positions of the atomic layers. Nonetheless, the unit cell of the monolayer can have two configurations: trigonal prismatic, 2H, and octahedral, 1T, see Fig. 2.1 [16, 17]. The TMCDs monolayers, however, are predominately found at the 2H configuration. Fig. 2.1 present a picture of the crystal structure of a TMDC on its 2H configuration, and also the unit cell of the 1T configuration. Fig. 2.1 also shows the interlayer spacing for MoS_2, which is 0.65 nm.

Due to the 2D nature of MoS_2, its electronic structure and its band gap are modified by

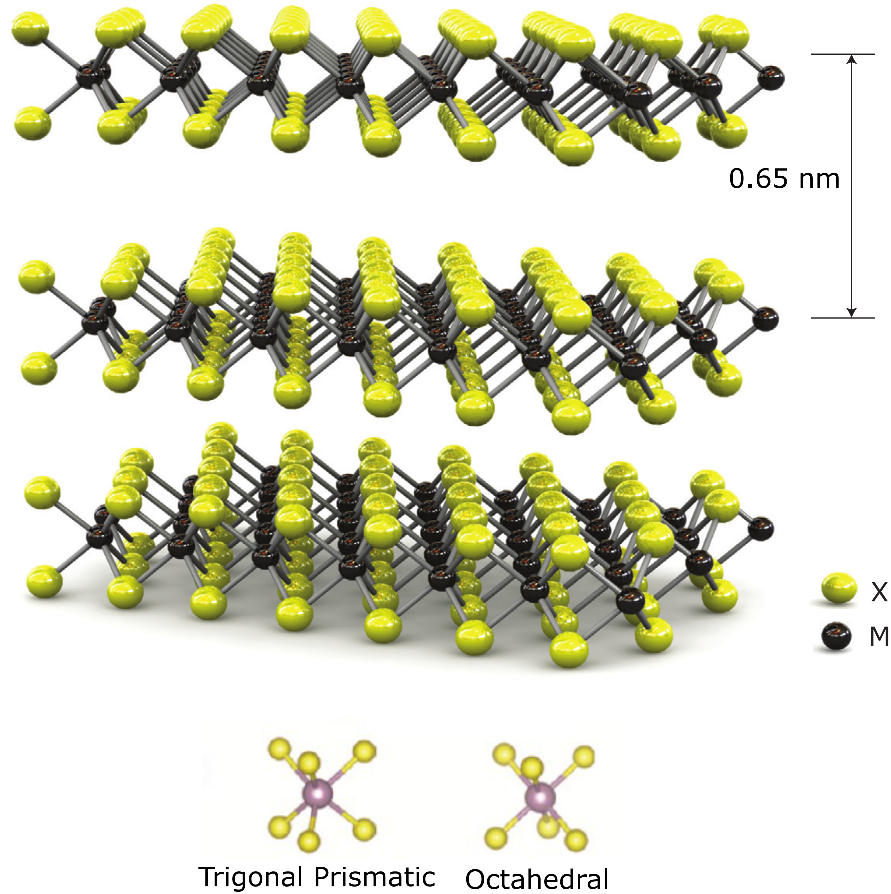

Figure 2.1: **Crystal structure of a TMDC**. Taken from [16, 17].

the quantum confinement. For example, from the bulk to the monolayer, the band gap goes from indirect, with energy 1.29 eV, to direct, with energy 1.9 eV [18]. In bulk MoS_2, the maximum of the valence band (VB) is on the Γ point, while the minimum of the conduction band (CB) is between the Γ and K points [19], see Fig. 2.2(a). The states of the CB in the K point are due to the orbital d from the Mo atom, which are slightly affected by the interlayer interactions. On the other hand, the states of the CB close to the Γ point are a result of the hybridization of the orbitals p_z, from the S atom, and d, from the Mo atom. These orbitals are affected by interlayer interaction. In this way, decreasing the number of layers increases the energies of the states of the CB close to the Γ point, while near of the K point, the states remain constant. This asymmetry in the modification of the CB states under quantum confinement leads to the direct band gap of the MoS_2 monolayer [19–22], see Fig. 2.2. Some theoretical [22, 23] and experimental [24, 25] works report that excitons influence on the optical transitions in the few layers MoS_2, instead of band-to-band transitions. In absorption and photoluminescence measurements, it is possible to identify two excitonic peaks, A and B, which physical explanation is a spin-orbital breaking of the degeneracy of the top of the valence band in two states [24]. Beyond the strong excitonic effects in MoS_2, other interesting multi-body phenomena are still observable in this material, like biexcitons [26] and trions [27, 28], which are out of the scope of this thesis.

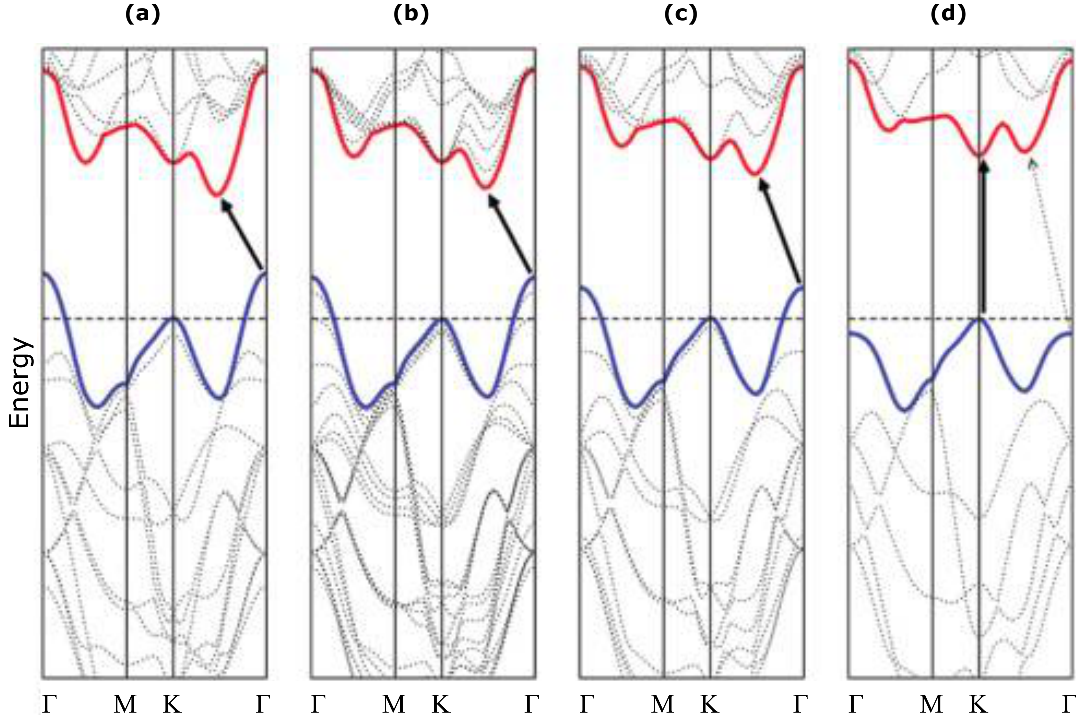

Figure 2.2: **The band structure of MoS_2.** The figure **(a)** is from the bulk, while the **(b)**, **(c)**, and **(d)**, correspond to the tri, bi, and monolayer, respectively. Taken from [19].

The direct band gap of MoS_2, the excitonic properties, and the ultra-thin nature make MoS_2 an interesting platform to study electronics, optics and optoelectronics [6, 29–32]. In MoS_2 electronics research field, the most common architecture is the field effect transistor (FET). MoS_2 FETs show ultra-high values of current on/off ratio (10^8) [16] and high mobility of 34,000 $cm^2V^{-1}s^{-1}$ that allows the observation of quantum transport [33]. MoS_2 transistor are predominantly n-type, due to a Fermi level pinning close to the conduction band, attributed to intrinsic vacancies in MoS_2 [34, 35]. However, ambipolar transport [36], as well as p-type transistors [37–39], have also been demonstrated. Most recently, some works have proposed utilizing a thin capping hexagonal boron nitride (BN) layer between the MoS_2 and the metal electrode to make a tunneling contact. This procedure prevents the influence of surface defects on the electrical contact, reducing the Fermi level pinning and Schottky barriers [40, 41]. Moreover, the development in the electronics of the 2D materials allowed the creation of memory devices using MoS_2 [42–47].

Due to its direct band gap, and its ultra-thin nature that allows the formation of Van der Waals heterostructures, MoS_2 possess a vast range of interesting optoelectronics phenomena. It has been reported photodetectors with a high sensitivity of $R \sim 10^3$ A/W [13, 48], where R is the ratio of the generated photocurrent and the laser power. Also, laser exposures close to the interface between MoS_2 and the electrode create temperature gradients, generating an electric output tension that can power external devices, revealing a photothermoelectric effect [49]. Furthermore, by transferring a p-type WSe_2 on MoS_2 it is possible to obtain a high photovoltaic effect with high external quantum efficiencies exceeding 50 %, with applications for solar energy. [50]. MoS_2 is also an exciting material to study light emission, so electro-

luminescence devices using MoS_2 have been explored [51, 52]. Finally, the optoelectronic properties of MoS_2 have also been used to develop an optical memory [53], where the memory states are recorded by exposing the device to light.

2.2 Field effect transistors

Due to the ultra-thin nature of the 2D materials, with an associated high surface-area-to-volume ratio, their optoelectronic properties are profoundly affected by substrate interactions and external fields [4, 16, 33, 54]. Amongst them, the electric field is a powerful tool to tune the optoelectronic properties of the 2D materials. The most common device structure used for applying electric fields is the field effect transistor. By using MoS_2 in a FET device, it is possible to control MoS_2 conductance [16], photocurrent generation [55] and excitonic properties [28]. In part I of this thesis, the electric field applications in MoS_2 FETs enables a controllable modification of the persistent photocurrent in these devices, which lead to a gate-tunable photomemory effect. Thus, it is essential to describe the FET operation. Fig. 2.3(a) shows a sketch of a 2D FET architecture. It is composed of three elements: the channel, the gate, and the insulator. The channel is the material (mainly a semiconductor) where the electrical current flows. The gate is the electrical terminal where electrostatic potentials are applied (V_{BG}), generating an electrical field across the insulator into the channel. Three electrodes are contacting the FET. The source (S) and drain (D) electrodes make electrical contacts in the channel. Generally, we connect a voltage source to the source, and we ground the drain. In this way, applying a drain bias (V_{SD}) to the source enables a current flow in the channel. Finally, we connect the third electrode to the gate.

A transistor can operate as a current amplifier or as a switcher. By applying a fixed V_{SD} in the source relative to the drain of the FET, it is possible to flow an electrical current in the channel, named drain current (I_{SD}), see Fig. 2.3(a). The V_{BG} application modulates I_{SD}, see Fig. 2.3(b), which shows a I_{SD}vsV_{BG} curve, also called transfer curve. If the channel is an n-type semiconductor, as for MoS_2, the application of $V_{BG} > 0\,V$ electrostatic induces negative charges in the channel. The drain is grounded, so the electrostatic induction injects electrons from the drain to the channel, increasing I_{SD}, see the red region on Fig. 2.3(b). The transistor is on its "ON" state when a current flows on its channel, see red region on Fig. 2.3(b). By applying $V_{BG} < 0\,V$, the negative gate bias expels the electrons from the channel towards the drain, reducing I_{SD}. Below a specific gate voltage, the conduction band of the semiconductor is empty of electrons, "OFF" state, preventing that a current flows in the channel, see the blue region on Fig. 2.3(b). The specific value of V_{BG} that switches between the states "OFF" and "ON" is called threshold voltage (V_{th}), see Fig. 2.3(b).

Real-world transistors are not ideal, so divergences from the theoretical transistor model may occur. For example, the current in the "OFF" state may not be absolutely zero. Another example is that the transition between the "OFF" and "ON" states are not abrupt as shown in Fig. 2.3(b). For this last case, we evaluate V_{th} from the intercept of the extrapolation of the linear part of I_{SD}, in the "ON" state, with the V_{BG} axis, see Fig. 2.3(b). Another important physical quantity extracted from a transfer curve is the transconductance (g_m)

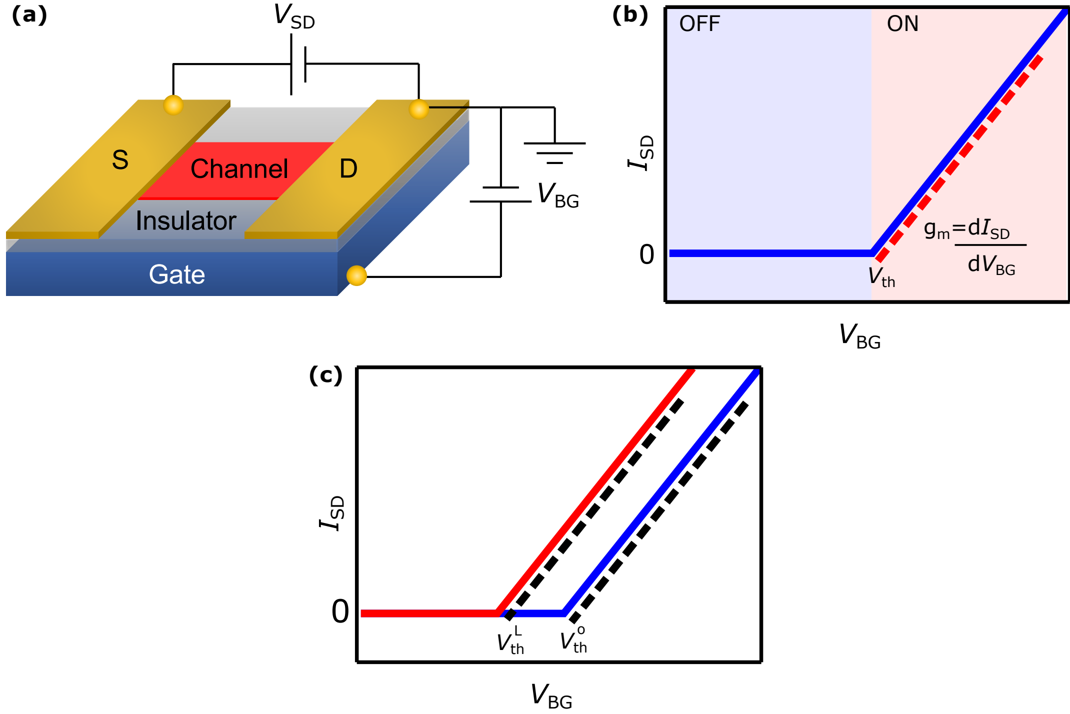

Figure 2.3: **Field effect transistor**. **(a)**, Sketch of a field effect transistor. **(b)**, transfer curve of a field effect transistor. **(c)**, transfer curves before, blue curve, and after, red curve, laser exposure.

given by the slope of the transfer curve ($g_{\mathrm{m}} = \frac{dI_{\mathrm{SD}}}{dV_{\mathrm{BG}}}$). Both V_{th} and g_{m} have important physical significance since from V_{th} it is possible to extract the intrinsic and induced dopings in the channel and from g_{m}, the mobility μ of the semiconductor.

To estimate the density of charge induced by V_{BG} we can use a parallel plate capacitor model. From this model, we have:

$$Q = C(V_{\mathrm{BG}} - V_{\mathrm{th}}) = nAe, \tag{2.1}$$

where Q is the induced charge in the channel, n is the density of free charges, C is the capacitance, A is the area of the plates of the capacitor, and $V - V_{\mathrm{th}}$ is the effective voltage applied on the channel. Equation 2.1 is valid for $V_{\mathrm{BG}} - V_{\mathrm{th}} > 0\,\mathrm{V}$, whether for $V_{\mathrm{BG}} - V_{\mathrm{th}} < 0\,\mathrm{V}$, $Q = 0$. C has the following expression:

$$C = \frac{\epsilon_0 A \epsilon_{ox}}{d}, \tag{2.2}$$

where ϵ_0 is the vacuum permittivity, which is $8{,}85 \times 10^{-12}$ $\mathrm{C^2N^{-1}m^{-2}}$, and ϵ_{ox} is the dielectric constant of the insulator. Finally, d is the thickness of the insulator. From equations 2.1 e 2.2, we get:

$$n = \frac{\epsilon_0 \epsilon_{ox}}{e\,d}(V_{\mathrm{BG}} - V_{\mathrm{th}}) = D_0(V_{\mathrm{BG}} - V_{\mathrm{th}}). \tag{2.3}$$

which gives an expression for the density of charges, units in $\mathrm{cm^{-2}}$, that is a function of V_{BG} and V_{th}. In chapter 4, we present transfer curves before and after exposures of MoS_2

to a laser. Comparing these curves, we argue that laser exposures change the doping of our devices, so equation 2.3 is very important to describe our results. To exemplify how we get to this conclusion, we show in Fig. 2.3(c) transfer curves of a fictional transistor. We first evaluate a transfer curve before laser exposure, blue curve in Fig. 2.3(c). From the blue curve, we evaluate the threshold voltage before laser exposure ($V_{\mathrm{th}}^{\mathrm{o}}$). Then, we perform a laser exposure on the fictional transistor. After this procedure, we repeat a transfer curve and extract the new threshold voltage ($V_{\mathrm{th}}^{\mathrm{ph}}$), see the red curve in Fig. 2.3(c). Inspecting the red and blue curves, we conclude that their threshold voltages are different, which is evidence for laser-induced doping. We can evaluate the change of the density of charges induced by laser exposure through the following equation:

$$\Delta n_{\mathrm{L}} = n_{\mathrm{ph}} - n_{\mathrm{o}} = D_0(V_{\mathrm{th}}^{\mathrm{ph}} - V_{\mathrm{th}}^{\mathrm{o}}). \tag{2.4}$$

Finally, from Fig. 2.3(b), we can evaluate the mobility of the FET, which is measured by the following equations:

$$\mu = \frac{g_{\mathrm{m}}}{V_{\mathrm{SD}}} \frac{l}{wC_{ox}} \tag{2.5}$$

$$g_{\mathrm{m}} = \frac{dI_{\mathrm{SD}}}{dV_{\mathrm{BG}}} \tag{2.6}$$

$$C_{ox} = \frac{\epsilon_0 \epsilon_{ox}}{d}, \tag{2.7}$$

where l and w are the length and the width of the channel, respectively.

2.3 Photocurrent

In this section, we approach photocurrent, which is the main optoelectronic effect of part I of this thesis. Photocurrent is any process where the absorption of photons in materials generates electrical currents. Many mechanisms produce a photocurrent, as the photovoltaic effect [50], the photothermoelectric effect [49], the photodoping effect [56] and the photoconductivity effect [55]. In the photovoltaic effect, a built-in electric field, in a pn junction, for example, separates photoexcited electron-hole pairs, generating a photocurrent. For the photothermoelectric effect, the laser exposure close to the interface between two materials with different Seebeck coefficients generates a temperature gradient that drifts carriers. In the photodoping effect, the photocurrent is due to the alteration of the threshold voltage of the device with laser exposure. Finally, the photoconductivity effect is due to the separation of the photoexcited electron-hole pairs by an external electric field. For a detailed explanation of these mechanisms, please see the reference [57]. The MoS_2 FETs in chapter 4 present both the photodoping and the photoconductivity effects. Next, we better analyze these effects. For the photoconductivity effect, photons excite electrons from the valence to the conduction bands of the material, generating excess electrons and holes. So, an electric field transforms these excess carriers in an electric current before they recombine. The

conductivity of a conductor is given by:

$$\sigma = e\mu_n n + e\mu_p p \tag{2.8}$$

where e is the electron charge and p is the concentration of holes. Here, we have assumed that the mobility for electrons and holes are different. After the moment that the device absorbs photons, there are excess carriers δn and δp. $\delta n = \delta p$, because the electron-hole pairs are created simultaneously. Then, adding the terms of the excess carrier in equation 2.8 leads to:

$$\sigma = e(\mu_n + \mu_p)\delta n + e\mu_n n + e\mu_p p \tag{2.9}$$

So, if we subtract equations 2.8 and 2.9, we get an equation for the photoconductivity:

$$\delta\sigma = e(\mu_n + \mu_p)\delta n. \tag{2.10}$$

Now, we describe in more details the dynamics of the excitation and decay of the photogenerated carriers. When the semiconductor absorbs photons with energy larger than the gap of the material, it creates electron-hole pairs, see Fig. 2.4(a).

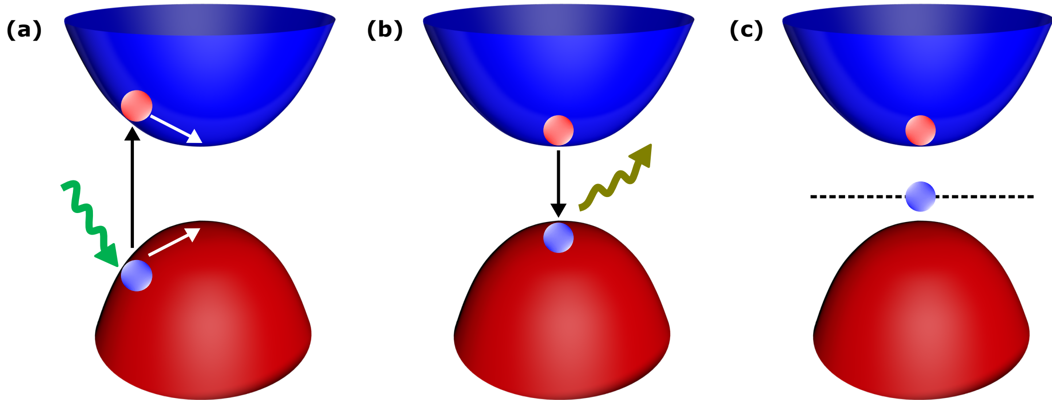

Figure 2.4: **Excitation and decay of photogenerated carriers.**

The photogenerated carriers relax to the bottom and top of the conduction and valence bands, respectively, see Fig. 2.4(a). Generally, the relaxation process is due to carrier-carrier and carrier-photon scatterings, which imposes a fast response of the order of femtoseconds [58]. After relaxation, the excess carriers recombine emitting a photon with the energy of the gap, see Fig. 2.4(b). The time for the recombination of the excited electron-hole pairs (lifetime) has a characteristic value of τ_d. τ_d varies from picoseconds to nanoseconds [58], which is longer than the time for relaxation (femtoseconds). So, the carriers relax first, in a fast process, to subsequently recombine. The equation of the time-evolution of the excess carriers is given by:

$$\frac{d\,\delta n}{dt} = \Phi - \frac{\delta n}{\tau_d}, \tag{2.11}$$

where Φ is the photon flux. An expression for Φ is $\Phi = \eta P_l \lambda / Ahc$, where η is the quantum

efficiency, P_l is the power of the laser, λ is the wavelength of photons, h is the Plank constant, c is the speed of the light and A is the area of the incident light. For stationary conditions, we have that $\frac{d\delta n}{dt} = 0$, so equation 2.11 becomes:

$$\delta n = \Phi\tau_d. \tag{2.12}$$

We expect that the photocurrent response is as fast as the lifetime of the electron-hole pairs (nanoseconds). However, if the crystal has defects on its structure or interacts with the substrate strongly, the lifetime may be prolonged. This fact occurs because these effects generate mid-gap states that trap the carriers preventing them from recombining and increasing the response time of the photocurrent, see Fig. 2.4(c). Sometimes, the response time of some semiconductors is too slow that we name the photocurrent retained after we turn the laser off by persistent photocurrent (PPC). PPC is undesirable for photodetection operations [55], nonetheless in chapter 4 we show that we can use PPC for memory applications.

PPC is important in MoS_2 phototransistors, so we should describe better this effect. Fig. 2.5 presents I_{SD} vs Time measurements for a device without, Fig. 2.5(a), and with, Fig. 2.5(b), PPC. The plots in Fig. 2.5 are not from real measurements; we present them only to explain the PPC better. In Fig. 2.5, the regions denoted by OFF means that the laser is off, while the regions ON means that the laser is on. For a device free of PPC, see Fig. 2.5(a), the response time is fast, as it is limited by the lifetime of the excited electron-hole pairs. In this way, the current increases and saturates very rapidly after we turn the laser on and decays very fast after we turn the laser off. So, we commonly observe very sharp square curves in devices that do not present PPC, see Fig. 2.5(a). On the other hand, for devices with PPC, the response time is prolonged. In other words, the photocurrent takes too long to saturate and to decay, so the I_{SD} vs Time curves resemble a sawtooth profile, see Fig. 2.5(b). In chapter 4, the I_{SD} vs Time curves of MoS_2 transistors have a response which is a mixture of both Fig. 2.5(a) and Fig. 2.5(b), and we ascribe this behavior to the coexistence of the photoconductivity and photodoping effects.

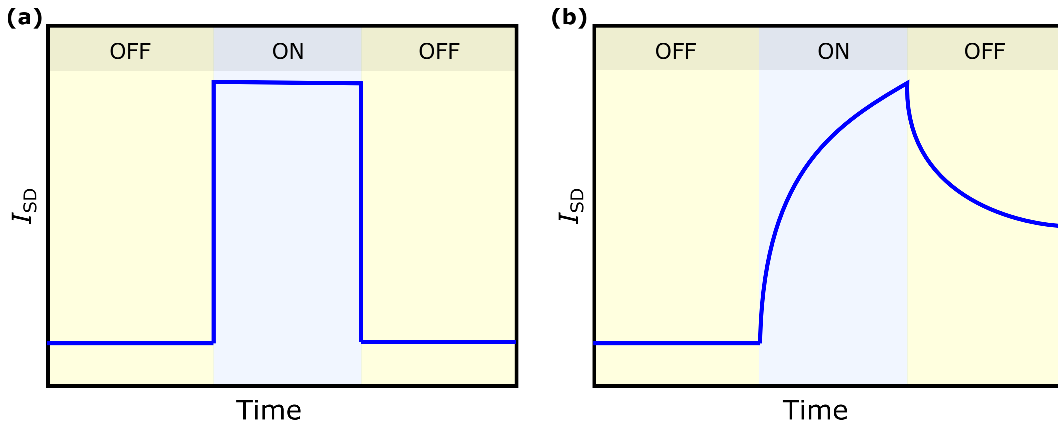

Figure 2.5: **Comparison of photocurrent responses**. I_{SD} vs Time measurement for a device without, **(a)**, and with, **(b)**, PPC.

To estimate the response time of I_{SD} vs Time curves, like in Fig. 2.5, we can apply an

exponential fitting for the decay of the photocurrent, which formula is $y = A + B \times exp\left(-\frac{t}{\tau}\right)$. From this formula we can estimate τ. However, for MoS_2 devices, it is not possible to fit the I_{SD} vs Time curves with this last equation, so it needs a correction, which is called the stretched exponential, see the following equation:

$$y = A + B \times exp\left(-\frac{t}{\tau}\right)^{\gamma}, \tag{2.13}$$

where A is the reminiscent photocurrent, B is a multiplication factor, τ is the decay time and γ is a dimensionless parameter. In chapter 4 we apply PPC in a memory effect. Thus, we can use equation 2.13 to estimate the reminiscent memory percentage (RMP (%)), evaluated by the expression.

$$\text{RMP}\,(\%) = 100 \times \frac{y(t \to \infty)}{y(t = 0)} = 100 \times \frac{A}{A + B}. \tag{2.14}$$

Many reports in MoS_2 phototransistors present a strong PPC effect [13, 54, 59]. On the other hand, some MoS_2 transistors present a very sharp photocurrent behavior as Fig. 2.5(a) [55,60]. So far, it is not clearly understood the mechanism responsible for the PPC in MoS_2. MoS_2 is a 2D material, where the interfaces strongly affect its properties, so it is hard to say if the PPC comes from MoS_2 itself or the interfaces. Indeed, some works associate the PPC to a photodoping process that is attributed to the charge transference from the adsorbed gases to MoS_2 [56]. On the other hand, some papers argue that the PPC is due to the interactions between the MoS_2 channel and the substrate [54,61]. Another report claim that PPC is due to some mid-gap states in MoS_2 that increase the recombination time of the electron-hole pairs [48]. The reference [54] presents a profound and rich experimental study that compares a freestanding device with a supported one. The authors show that the supported device presents PPC, while the freestanding do not. In this way, the substrate beneath MoS_2 plays an essential role in the photocurrent response. In this thesis, we give a step forward to the understanding of the PPC in MoS_2 transistors. Thus, we show in chapter 4 that the PPC is due to a photo-assisted trapping of holes in the gate-insulator interface - a photodoping process. We also show that we can modulate the PPC with simultaneous applications of the gate voltage and laser exposure, which in turn give rise to a photomemory effect. Hence, to better understand our photomemory effect we discuss some critical points regarding the memory phenomenon in the next section.

2.4 Memory

Since the beginning of the information era, the production of data has increased exponentially. So, the need to store information, by developing memory devices, have become crucial. In this way, it is progressively desirable and demanded memory devices with high storage capability. Furthermore, obtaining small devices is also a concern for memory technology. These facts are highlighted in Fig. 2.6(a), where it shows a gigabit/in^2 vs year curve [62]. Fig. 2.6(a) depicts that the storage capacity of memory devices increases over the years, with a simultaneous reduction of the size of the devices. However, storage capability and

miniaturization are not the only desired features for actual memory devices. The cost is also significant for the production of new technologies for memory devices. In fact, Fig. 2.6(b) shows a USD/MB vs year curve [63], which indicates that the cost of a megabit is becoming increasingly low.

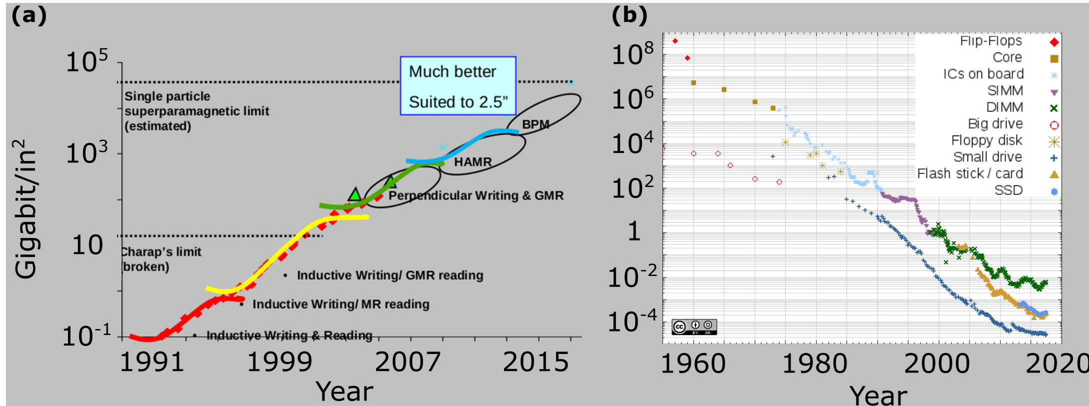

Figure 2.6: **Evolution of memory over the time**. **(a)**, a gigabit/in^2 vs year curve. Data taken from [62]. **(b)**, a USD/MB vs year curve. Data taken from [63].

To better elucidate the evolution of memory devices, Fig. 2.7 compares two devices. Fig. 2.7(a) shows a picture of the IBM 305 Ramac model [64], a memory device from 1956 which has a storage capacity of 5 Mb with a price of 10000 USD/Mb. On the other hand, Fig. 2.7(b) shows an image of the Samsung 16TB SSD memory device from 2016 [65]. This device has a storage capacity of 16 Tb, with a price of 0.001 USD/Mb. To compare the size of the devices, Fig. 2.7(a) also present the picture of a man whose height is similar to the primitive device, while Fig. 2.7(b) shows a cartoon of a finger with almost the size of the present-day device.

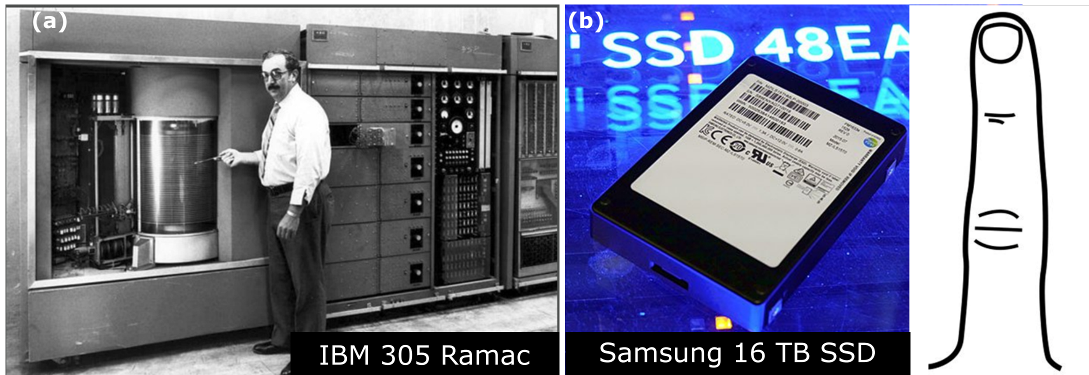

Figure 2.7: **Comparing memory devices**. **(a)**, an IBM 305 Ramac device, taken from [64]. **(b)**, a Samsung 16 TB SSD device, taken from [65].

To summarize, the required features (figures of merit) for actual memory devices include the miniaturization capability, the power consumption (high memory on/off ratio), the operation speed, the memory retention time and the cost. To understand these aspects, we need to describe what are memory devices. A memory device is an object able to store information using power supply. There are two types of memory devices: volatile and non-volatile. The

volatile memory device loses information after we turn the power supply off. On the other hand, the non-volatile memory devices store the information even after we turn the power supply off. Modern memory devices use digital electronics. The digital electronic uses the binary system, thus digital memory devices stores information through "0" and "1" codes. Before we discuss the memory figures of merit in details, lets first describe the components of a memory device shortly.

A memory device is composed of a memory keeper, which is a physical object that stores the information, see Fig. 2.8. The memory keeper has some physical property that has binary configurations. For example, spins in a ferromagnetic device (hard disk drive) or burned dye spots on a CD-R [66]. Also, the memory system needs a writer, which is a physical element that manipulates the physical properties of the memory keeper in "0"s and "1"s, "recording" the desired information. The writer can be a magnet or a laser, for example. Furthermore, the memory system needs a reader, which is a physical element that "reads" and exports the information. This brief description of memory devices is quite general and abstract. However, to develop memory devices in the modern era, we need to have in mind the required figures of merit for their application.

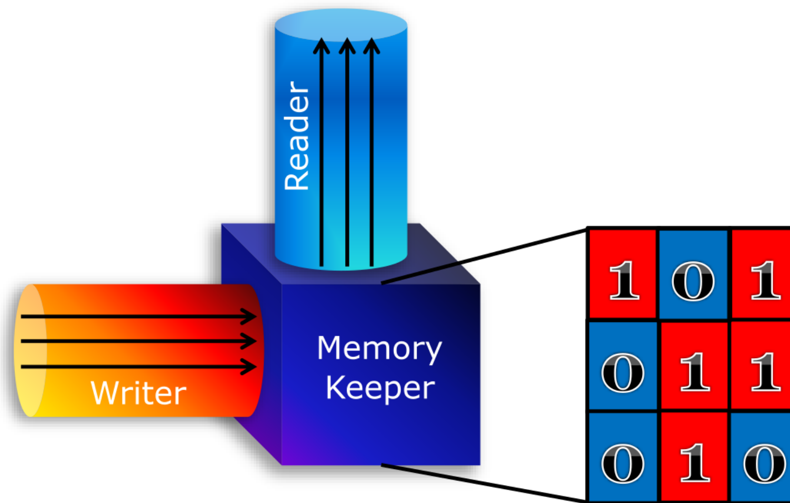

Figure 2.8: **Memory components.**

The memory power consumption is the effort needed to read the memory states. So, as much distant the "0" and "1" states are, the easier it is to read the memory states. Frequently, memory device papers use the memory on/off ratio as the quantity that measures the power consumption of the memory device. The on/off ratio is the ratio of the physical quantity (used for memory storage) of the memory keeper in the "1" and "0" states, respectively. The memory retention time is also an important parameter to evaluate a memory device, as it measures the memory loss over ten years. A method to measure this quantity is by evaluating the reminiscent memory percentage, which is the quotient (%), between the estimated value after ten years and the initial value of the physical quantity used for memory storage. The operation speed is the time to switch between the "1" and "0" states, or in other words the time to record the memory information. The miniaturization capability, in turn, is the

ability to decrease the size of the components from the memory device. 2D materials are innately small, so they are excellent candidates to develop miniaturized memory devices. Nevertheless, to compare the cost of nanotechnology devices is straightforward, as nowadays it is tough to infer the real price of these products. Hence, we are not going to discuss the cost feature of memory devices in this thesis. To exemplify memory operations, we describe in Fig. 2.9 three types of electronic memories. We start by describing the flash memory device, which is an electronically erasable programmable read only memory (EEPROM). The flash memory consists of the semiconductor channel, with the source and drain contacting it; the tunnel insulator, which is a thin insulator layer (thickness less than 10 nm [67]) that enables tunneling; the floating gate, which is not connected electrically; the gate insulator, that is a thick insulator that avoids tunneling (typical thickness of 30 nm [67]); the control gate, which is contacted electrically, see Fig. 2.9(a). By applying V_{SD} in the source relative to the drain, a current flows in the channel. On the other hand, the application of $V_{\text{BG}} > 0\,\text{V}$ tunnels electrons from the channel through the tunnel insulator, reaching the floating gate, where they are trapped, storing the memory information, see Fig. 2.9(a). When this happens, the channel is in its low current regime, and the device is referred to be in its "programmed" state. Besides, by applying $V_{\text{BG}} < 0\,\text{V}$, electrons from the floating gate tunnels through the tunnel insulator and reach the channel, erasing the memory information, see Fig. 2.9(b). In this configuration, the channel is in its high current regime, and the device is referred to be in its "erased" state. Making an analogy of flash devices with Fig. 2.8, the "writer" element is the gate voltage, the "reader" element is the current of the channel, and the memory keeper is the trapped electrons in the floating gate. The flash devices have advantages of high memory operation speed, moderate memory on/off and retention time values. Yet, a bottleneck of this architecture is that it requires many elements into a complex structure.

Two-terminal floating-gate tunneling devices have been proposed to overcome the complexities issues of the flash architecture [42, 43, 68]. These simpler architectures use fewer elements than flash devices and need only two terminals. They are also referred to as two-terminal tunneling random access memory (TRAM). The TRAM consists of a floating gate, a tunnel insulator and a semiconductor channel contacted by the source and drain electrodes [42], see Fig. 2.9(c). The TRAM devices use an intense electric field, by applying $V_{\text{SD}} < 0\,\text{V}$, to tunnel electrons from the channel, close to the source electrode, through the tunnel insulator, reaching the floating gate, see Fig. 2.9(c). The floating gate traps the electrons, storing the information. On the other hand, by applying a large $V_{\text{SD}} > 0\,\text{V}$, electrons from the floating gate tunnels through the tunnel insulator and reach the channel, erasing the memory information, see Fig. 2.9(d). To "read" the memory information, the TRAM requires a small V_{SD}, because a large bias tunnels the carriers through the tunnel insulator, disturbing the memory information. Making an analogy of TRAM devices with Fig. 2.8, the "writer" element is the V_{SD}, the "reader" element is the current of the channel, and the memory keeper is the trapped electrons in the floating gate. Although the TRAM device shows ultra-high memory on/off ratio and has a simple architecture, it lacks ultra-high time-stability. This last fact is due to the thin insulator barrier that also allows tunneling without applying a bias. Furthermore, the TRAM requires a specific insulator thickness to obtain

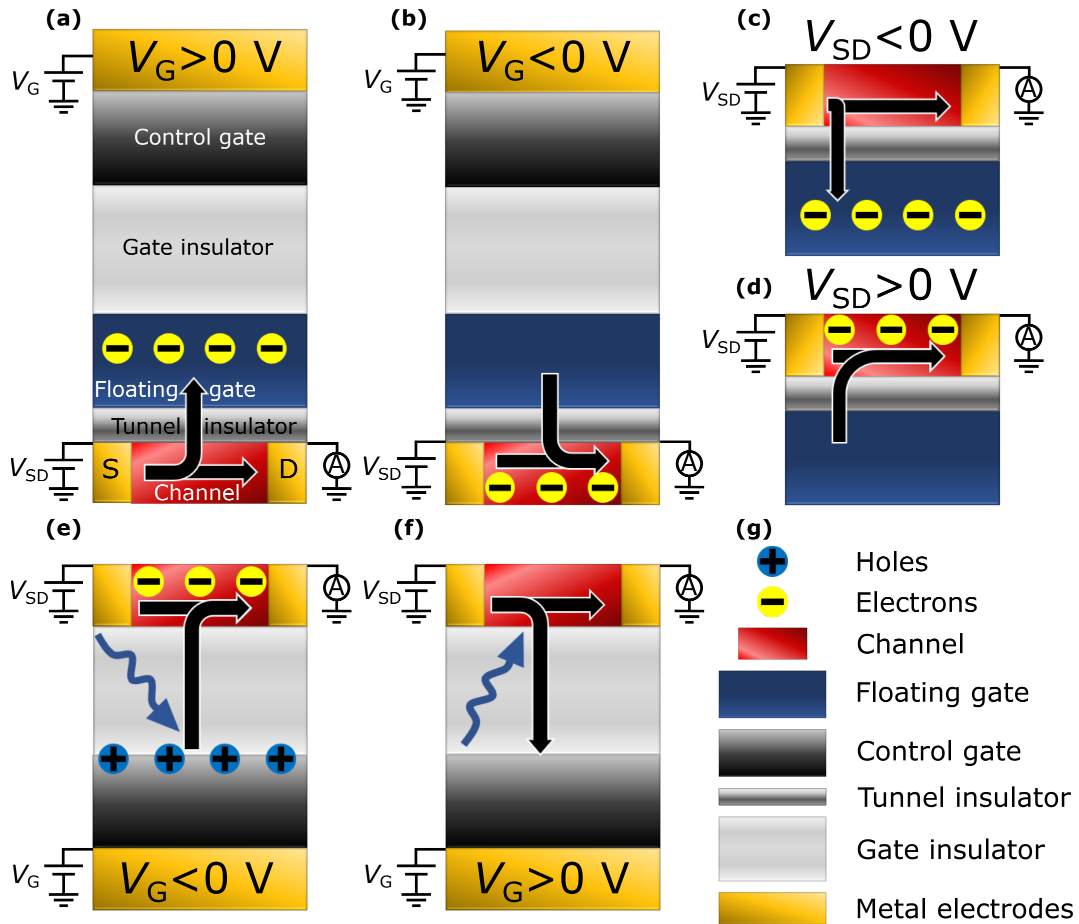

Figure 2.9: **Electronic memories**. Flash memory for $V_G > 0\,V$, **(a)**, and for $V_G < 0\,V$, **(b)**. TRAM memory for $V_G < 0\,V$, **(c)**, and for $V_G > 0\,V$, **(d)**. Photomemory for $V_G < 0\,V$, **(e)**, and for $V_G > 0\,V$, **(f)**. Legend of the components, **(g)**.

high a memory on/off ratio and reasonable time-stability, which can be a bottleneck for implementation in memory devices. In addition to this fact, the TRAM devices have limited possibilities of memory operations, because it uses a single terminal to simultaneously "read" and "record" the memory information.

We describe in Fig. 2.9(e) and Fig. 2.9(f) the operation of the photomemory device that we present in chapter 4. The photomemory is a standard FET, so it has a control gate, a gate insulator, and a semiconductor channel. As we discussed above, the gate insulator is thick, which prevents tunneling. However, the photomemory is due to a photoassisted charge trapping at the gate-insulator interface. By a simultaneous application of $V_{\text{BG}} < 0\,\text{V}$ and laser exposure, electrons from the gate-insulator interface are photoemitted to the conduction band of the insulator and are drifted by the electric field from the gate voltage towards the channel. The photoemitted electrons leave behind trapped holes that store the memory information. On the other hand, by applying $V_{\text{BG}} > 0\,\text{V}$ and laser exposure simultaneously, photons excite electrons from the channel to the conduction band of the insulator. Next, the electric field drifts the photoexcited electrons to the gate-insulator interface, where they recombine with the trapped holes. Hence, this process "erases" the memory information. By making an analogy of photomemory devices with Fig. 2.8, the "writer" is the combined actions of V_{BG} and laser exposure, the "reader" is the current of the channel and the memory keeper is the trapped holes in the gate-insulator interface. The photomemory has the advantage that we can apply large biases (V_{SD} and V_{BG}), without destroying the memory information, because the thick gate insulator prevents tunneling. In photomemory devices, the applications of laser exposure, V_{SD} and V_{BG} work as independent terminals, which combination gives novel and diverse memory operations. One example of these operations is the possibility to use the gate voltage to "read" and "record" the memory information independently. In addition, the photomemory has high memory on/off ratio and ultra-high time-stability.

After describing the memory operation of some architectures (see Fig. 2.9), we review the implementation of 2D materials in memory devices shortly. Many types of research have made efforts to apply the 2D materials in memory devices. However, to date, no reported simple memory devices are using 2D materials that cover most of the required features, notably the memory retention time [42–47, 53, 67–76]. The most common architecture to study electronic memory effects in MoS_2 is the flash architecture [44–46, 67]. As we argued before, the flash devices have advantages of high memory operation speed, moderate memory on/off and retention time values . Yet, a bottleneck of this architecture is that it requires many elements into a complex structure. Two-terminal floating-gate tunneling devices using 2D materials have been proposed to overcome the complexities issues of the flash architecture, [42, 43, 68]. They are simple devices with ultra-high memory on/off ratio, but they lack ultra-high time-stability. Hence, the development of alternative, high-performance, simpler memory architectures are strategical. Toward this direction, some reports have investigated a thermally assisted memory effect [69] and an optical memory effect [53] in a MoS_2 field effect transistor (FET) that is also a simpler architecture than flash devices. Nonetheless, in the first case, the memory effect has a drawback of not operating at room temperature

and both cases [53, 69] showed low memory on/off and short memory retention time values.

In chapter 4, we show that we can obtain a non-volatile photomemory effect with high on/off ratio and retention time in a MoS_2 FET architecture. Our photomemory effect is quite unusual compared to the memory effects described in the literature. Besides, the FET architecture, which is a simpler and more common structure than the standard memory architectures, hosts our photomemory effect. In chapter 4 we describe the photomemory effect in details. However, in advance, we propose a photomemory effect in MoS_2 FETs that expands the possibilities of memory application beyond conventional memory architectures.

Chapter 3

Methods and characterizations

In this chapter, we describe the methods and characterizations used in part I of the thesis. We start with the preparation of MoS_2 transistors. Next, we consider the optical characterizations of MoS_2, which are the photoluminescence and Raman spectroscopies. Then, we present the electrical characterizations of the MoS_2 transistors. Finally, we present the photocurrent setups that we use for the measurements of chapter 4.

3.1 Sample preparation

For part I of this thesis, we build two types of MoS_2 FETs. The first is a Van der Waals heterostructure consisting of a monolayer MoS_2 supported on a high-quality Boron Nitride crystal (BN). In this case, we use a graphite crystal to provide a flat back gate electrode. This device is referred to MoS_2/BN. The second device is a MoS_2 FET composed of a monolayer MoS_2 on a SiO_2/Si substrate where a highly n-type doped Si wafer is used as a back gate terminal. We name this device of MoS_2/SiO_2. Before explaining the preparation of the devices, we first comment on the transfer setup that we use to make the Van der Waals heterostructures. The transfer setup is composed of an optical microscope, see Fig. 3.1(a), a CCD camera, three micro-manipulators (xyz) that holds a glass slide and a stage with a heater.

The stage with a heater holds a substrate that keeps the flake after the transference. The substrate in the stage with a heater can also possess flakes on its surface. The glass slide holds a membrane, which supports the flake that we want to transfer. This membrane has different compositions depending on the procedure we want to do. For example, if we intend to do a single transference, we can make a membrane consisting of polydimethyl-siloxane (PDMS), then an adhesive tape and methyl methacrylate (MMA). The PDMS is just a support substrate, and we need the tape to adhere the MMA to the PDMS. After we

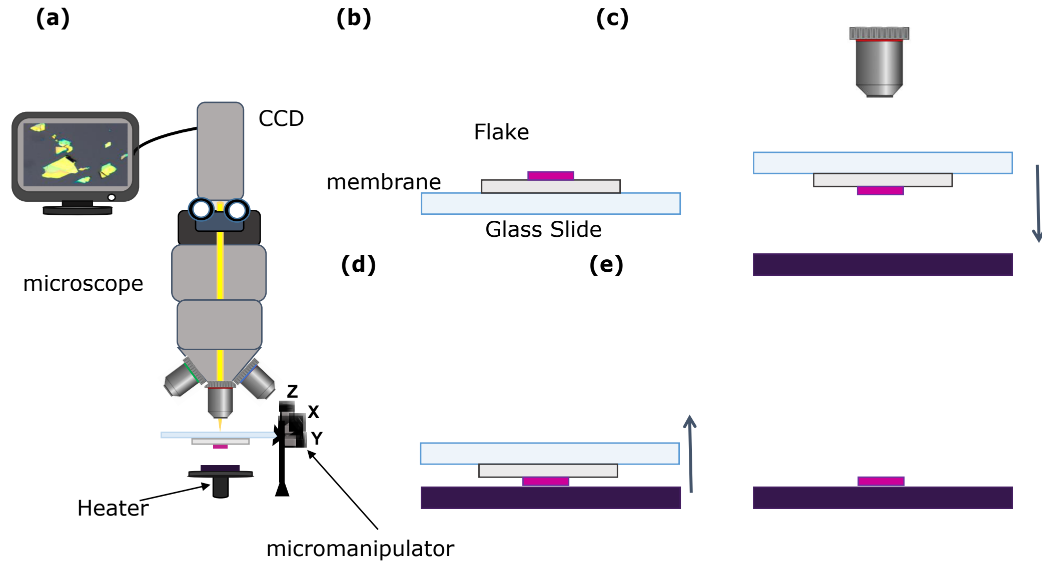

Figure 3.1: **Transfer setup**. Credits to Natalia Rezende.

prepare the membrane, we exfoliate the desired crystal with a blue tape (Blue Medium Tack, Semiconductor Equipment Corp.). Afterward, we transfer few-layer flakes from the tape to the membrane, see Fig. 3.1(b). We scan the area of the membrane, looking for specific flakes. Then, we load the membrane to the transfer setup, as in Fig. 3.1(c), and align the flake from the membrane with the flake from the stage with a heater. We approach the flakes, and after they touch each other, we heat the samples up to 135 °C, so the flake from the membrane transfer to the flake from the substrate [9]. To remove the MMA residue, we insert the substrate with the transferred flake in an acetone bath for a period of eight hours, or in boiling acetone (60 °C) for fifteen minutes. After the acetone bath, we rinse in isopropyl alcohol (IPA) and blow dry with argon. To make the layer of MMA, we spin coat MMA EL9 following the recipe: first ramp of 1000 rpm for 10 s, then the second ramp of 1500 rpm for 45 s followed by hotplate at 100 °C for 2 min. We can do another type of transference by using only the PDMS as the membrane [77]. For this case, it is not necessary to warm up the membrane to transfer the flakes in Fig. 3.1(d); physical contact is enough to accomplish that. We use the PDMS from the SYLGARD® 184 SIL ELASTOMER. The advantages of using the PDMS in the transference procedure are the acquisition of large area flakes, and the absence of polymer residues, because it is a dry procedure that does not require heating the samples [77]. However, this method allows transference of a limited number of materials, as TMDCs and talc. On the other hand, using MMA as a membrane allows transference of most 2D materials, but it is a wet procedure (leaving residues on the surface of the samples) and it demands to heat the flakes.

Now that we have commented on the transfer setup, we describe the preparation of the MoS_2/BN device. We do the following procedure to prepare the MoS_2/BN devices: graphite is mechanically exfoliated on a silicon wafer with a thermally grown oxide with 285 nm thickness (SiO_2/Si). Then, hexagonal boron nitride (BN) crystal is exfoliated on a membrane containing MMA. Afterward, a BN flake with $\approx$ 28 nm thickness is transferred to

a ≈ 20 nm graphite flake, see Fig. 3.2(a), by common wet transference procedure described in Fig. 3.1.

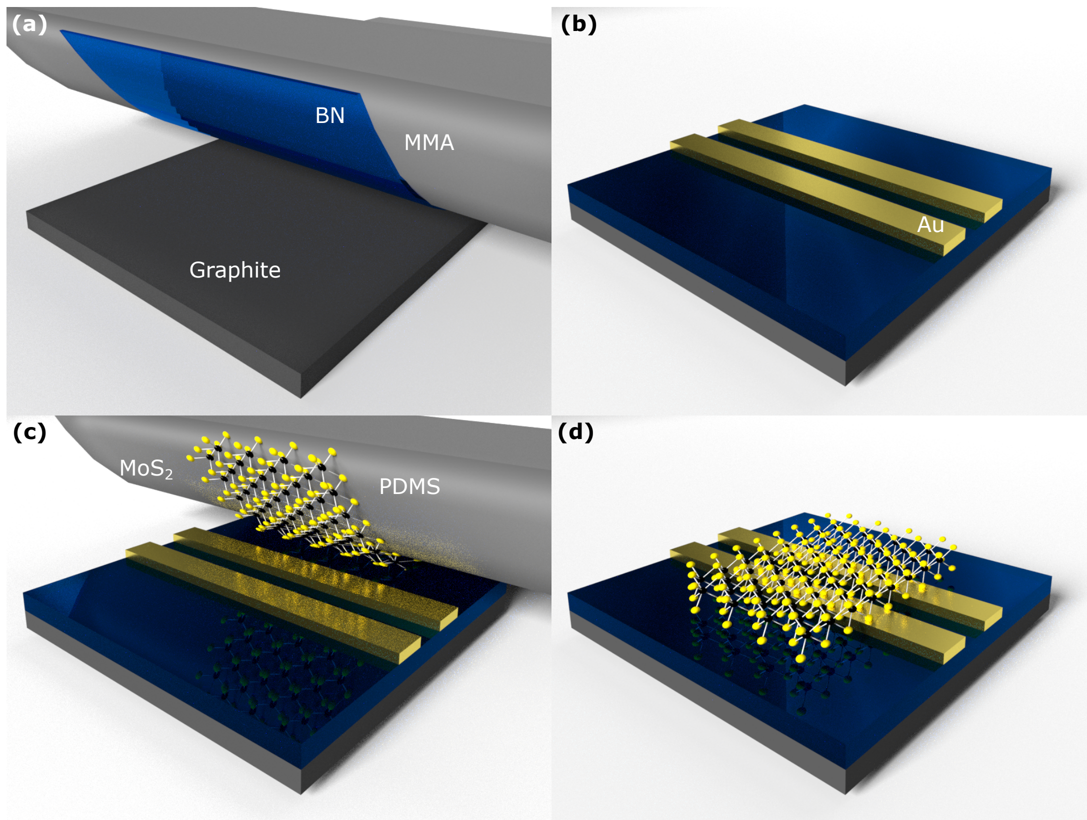

Figure 3.2: **Preparing the MoS_2/BN Device**.

We use the geometry of underneath contacts in our FET devices, so the electrodes are beneath MoS_2. The e-beam lithography technique is used to define source and drain electrical contacts on BN, and the gate electrode on graphite. We do not describe the e-beam lithography here, but the reader can find a detailed description in [57]. After writing the electrical contacts with the e-beam lithography, we develop the PMMA with a solution of deionized water (DI H_2O) and isopropanol (IPA) in the proportion 1:3 at 0°C for two minutes and rinse in (IPA). Next, we deposit by thermal evaporation a chromium sticking layer (thickness less than 1 nm) followed by a deposition of a layer of gold with 50 nm thick, see Fig. 3.2(b). At this point, the metal residue is removed by a lift-off procedure: boiling acetone (60 °C) bath for fifteen minutes and rinse in isopropanol followed by a nitrogen blow dry. Intending to remove PMMA and organic residues, we clean the sample in a tube furnace using Ar/H_2 flow (300 sccm/700 sccm) at 350 °C for three hours (ramp from room temperature to 350 °C of one hour). We exfoliate MoS_2 on the PDMS substrate, and then transfer it to the Metal/BN/graphite hetero-structure (see Fig. 3.2(c)) so forming the MoS_2/Au/BN/graphite heterostructures we label as MoS_2/BN, see Fig. 3.2(d). In this way, MoS_2 is directly contacted to the gold electrodes, which show linear response in I_{SD} vs V_{SD} curves [16]. In part I of this thesis, we study two MoS_2/BN devices, named MoS_2/BN-1 and MoS_2/BN-2. We deposit a second 20 nm gold layer on top of MoS_2 to improve electric contact in the MoS_2/BN-1 device. In addition to MoS_2/BN devices, we also study

MoS_2/SiO_2 devices. For the MoS_2/SiO_2 preparation, MoS_2 is exfoliated directly on SiO_2/Si substrate, the electrical contacts are again defined by e-beam lithography, and a 70 nm gold layer is deposited by thermal evaporation, then a lift-off procedure is done. Both MoS_2/BN and MoS_2/SiO_2 devices are transistors, and they present the photodoping effect. However, in chapter 4 we use the MoS_2/BN device to demonstrate the photomemory effect. On the other hand, we demonstrate that the photodoping in the MoS_2/SiO_2 device is local, allowing a spatial control of the photocurrent in this device.

Fig. 3.3 shows optical images of the devices under study. On Fig. 3.3 we highlight the elements of the devices. For the MoS_2/BN-1 device, see Fig. 3.3(a), the channel width (w) is 10 μm while its length (l) is 1 μm. For the MoS_2/BN-2 device, see Fig. 3.3(b), $w = 6$ μm and $l = 2$ μm. For the MoS_2/SiO_2 device, see Fig. 3.3(c), $w = 1$ μm and $l = 8$ μm.

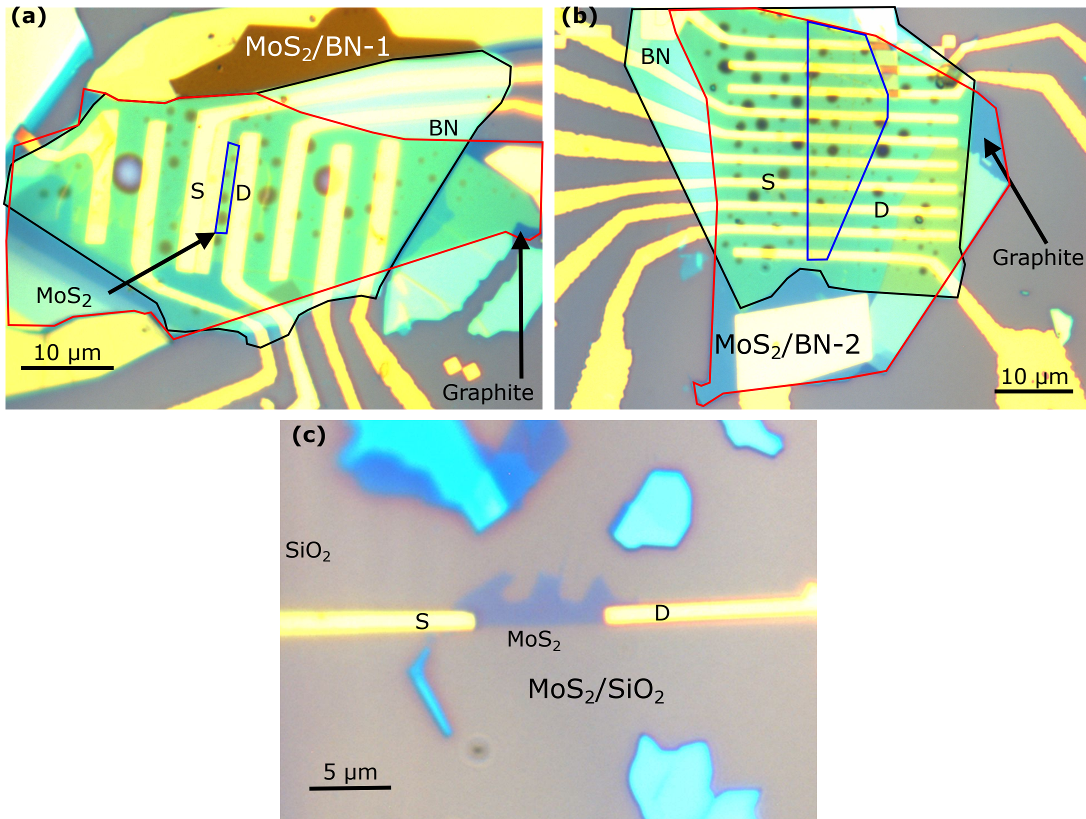

Figure 3.3: **Optical images of the devices**. Optical Images of the MoS_2/BN-1, **(a)**, MoS_2/BN-2, **(b)** and MoS_2/SiO_2, **(c)**, devices.

We can use the atomic force microscopy (AFM) to investigate the topography and surface cleanness of the devices. Fig. 3.4(a) and 3.4(b) show AFM phase images of the MoS_2/BN-1 and MoS_2/BN-2 devices, respectively. We did the measurement of Fig. 3.4(a) before the second 20 nm gold layer deposition on the MoS_2/BN-1 device. The figures show how the devices are clean due to the dry transference procedure and flat in most of the device area, despite there are a couple of regions with bubbles and wrinkles in MoS_2. As the MoS_2/BN devices are clean and flat in most of its area, the probability of scattering processes in the electronic transport decreases, improving the mobility of the device.

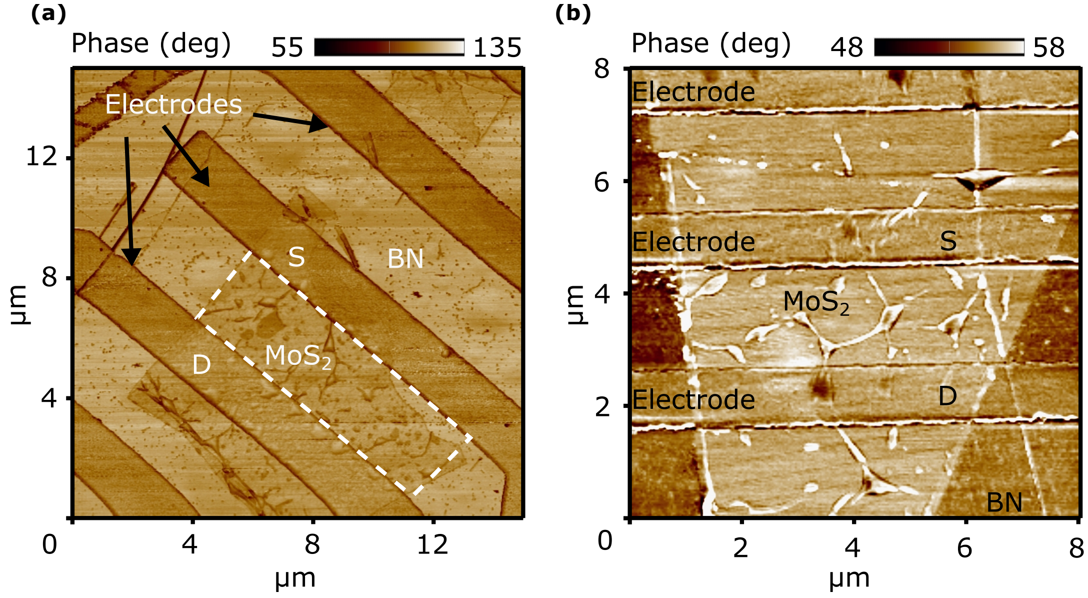

Figure 3.4: **AFM measurements**. AFM phase images of the MoS_2/BN-1, **(a)**, and MoS_2/BN-2, **(b)**, devices.

3.2 Optical characterization

Photoluminescence is the luminescence via photon absorption process. In semiconductors, the absorption of photons promotes excitations of electrons from the valence to conduction bands, see Fig. 2.4(a). The photoexcited electron-hole pairs relax to the botton and top of conduction and valence bands, respectivelly, and recombine emitting a photon with the energy of the gap of the semiconductor, see Fig. 2.4(b). Thus, the photoluminescence spectroscopy can provide relevant informations of materials, like the energy and type of their band gap, as well as the presence of excitonic effects. Monolayer MoS_2 is a direct band-gap semiconductor, so it exhibits strong photoluminescence (PL) emission with the existence of excitons at room temperature [19, 24]. For more than one layer, the band-gap of MoS_2 is indirect, and its PL is not so strong as for its monolayer counterpart. The PL spectra of the monolayer show two excitonic peaks at 1.8-1.9 eV and 2 eV, named A and B, respectively [19, 24]. Thus, by investigating MoS_2 with PL spectroscopy, it is possible to obtain crucial information regarding this material. Fig. 3.5 shows PL spectra of the MoS_2/BN-1, Fig. 3.5(a), MoS_2/BN-2, Fig. 3.5(b), and MoS_2/SiO_2, Fig. 3.5(c), devices. These figures show emissions that correspond to the A and B excitons, and also show the energy position of the A exciton which is 1.85 eV for the MoS_2/BN-1 device, and 1.83 eV for the MoS_2/BN-2 and MoS_2/SiO_2 devices, which correspond to a monolayer MoS_2 [19,24]. Because we do not study photoluminescence as the primary effect in part I, we do not explore this effect profoundly. Here, we only use the photoluminescence spectroscopy to characterize the monolayer MoS_2. However, in section 6.2 of part II we provide more details of the photoluminescence effect.

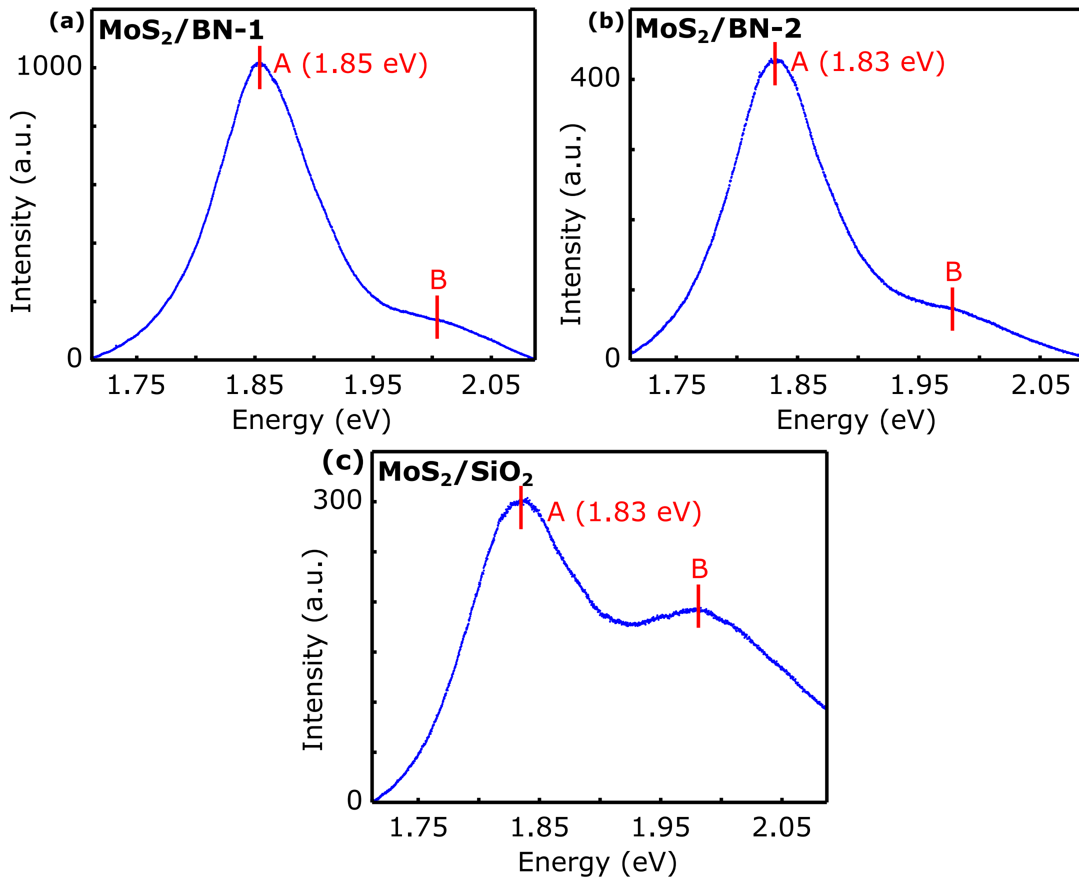

Figure 3.5: **Photoluminescence measurements**. Photoluminescence spectra of the MoS_2/BN-1, **(a)**, MoS_2/BN-2, **(b)** and MoS_2/SiO_2, **(c)**, devices. The measurements are done with a 457 nm laser ($\approx 1\ \mu$m spot size) and fluence of 340 $\mu W/\mu m^2$.

The Raman spectroscopy studies the vibrations in crystals and molecules that inelastically scatter light. Thus, by measuring the spectrum of this light, we can get pieces of information about the vibrational modes of the materials. More precisely, we can identify the Raman active vibrational modes by peaks in the Raman spectrum. As vibrations in systems are unique, we can consider the Raman spectrum as a "fingerprint". For example, the Raman spectroscopy can identify MoS_2, and the number of layers in a MoS_2 crystal. Here, we measure Raman spectra of MoS_2 to identify monolayer crystals. Among several Raman modes in MoS_2, E' and A' are the most important to identify the number of layers. The Raman peak of E' for monolayer is located around 384.5 cm^{-1} and is due to asymmetric in-plane vibrations of the S-Mo-S atoms. The A' mode, located around 403 cm^{-1}, is due to the out-of-plane vibrations of the sulfur atoms. As the number of the layer increases, the E' peak suffers a redshift, while A' peak suffers a blueshift. So the difference between the positions of these peaks is a good indicator for the number of layers [78, 79]. To identify the number of layers of the devices, Fig. 3.6 shows Raman spectra of the MoS_2/BN-1, Fig. 3.6(a), MoS_2/BN-2, Fig. 3.6(b) and MoS_2/SiO_2, Fig. 3.6(c), devices. The blue dots correspond to experimental data, and the red line represents Lorentzian fittings of the E' and A' peaks. The difference between the position of these peaks is 19 cm^{-1}, for the MoS_2/BN-1 device, 18.9 cm^{-1}, for the MoS_2/BN-2 device and 16.7 cm^{-1}, for the MoS_2/SiO_2 device. These values are in the range acceptable for a monolayer sample [78, 79].

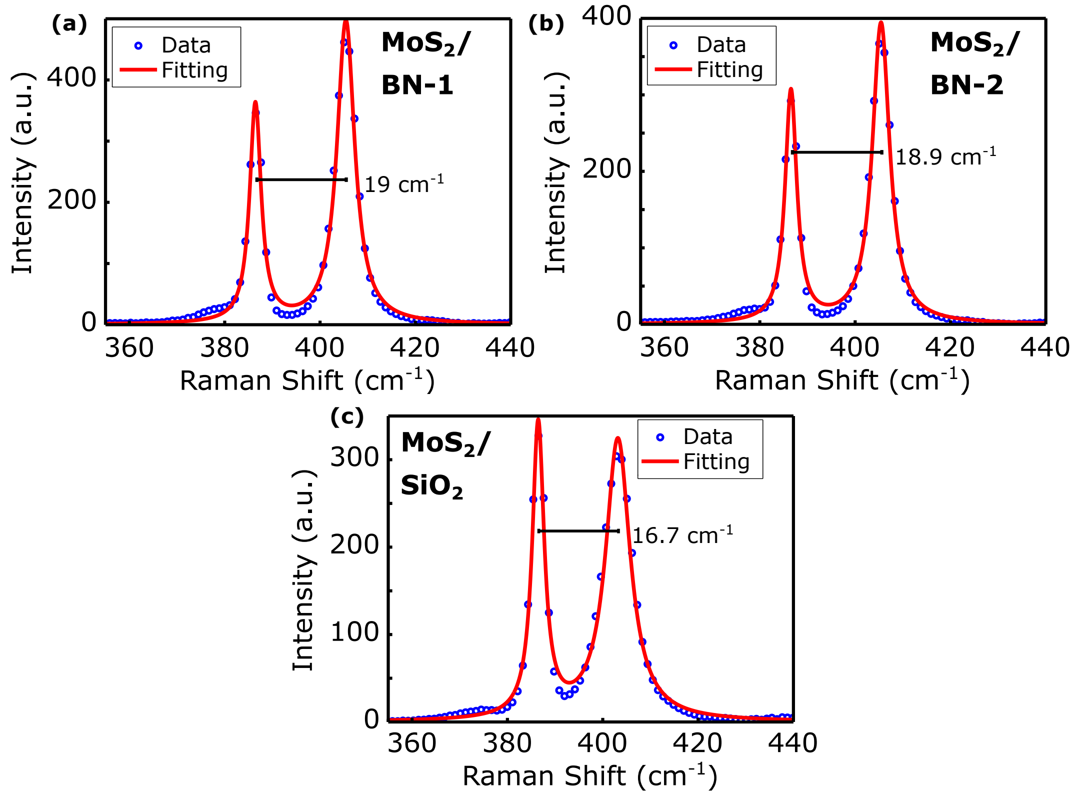

Figure 3.6: **Raman measurements**. Raman spectra of the MoS_2/BN-1, **(a)**, MoS_2/BN-2, **(b)** and MoS_2/SiO_2, **(c)**, devices. The dots are the data from the A' and E' peaks and fittings with two Lorentzians are represented by the red line. The measurements are done with a 457 nm laser (≈ 1 μm spot size) and fluence of 340 $\mu W/\mu m^2$.

To investigate the spatial distribution of the photoluminescence, Fig. 3.7(a) shows a PL image from the integrated area of the exciton A peak of the MoS_2/BN-1 device. Observe that the whole device emits photoluminescence uniformly with high quantum yield. In the bubbles regions, however, the emission is higher. To study how the Raman spectra distribute spatially, Fig. 3.7(b) shows a Raman image from the integrated area of the A' peak, again this peak is uniform throughout the device, except in bubbles regions. Fig. 3.7(c) shows the PL image of the MoS_2/BN-2 device, and its emission is more uniform than the emission from the MoS_2/BN-1 device. For the MoS_2/BN-2 device, the MoS_2 is above gold electrodes, so in Fig. 3.7(c) it is possible to observe PL emission in the contact region, but with lower intensity. Fig. 3.7(d) shows a Raman image of the A' peak for the MoS_2/BN-2 device. The A' intensity barely varies throughout the device except in bubbles regions. Finally, Fig. 3.7(e) and Fig. 3.7(d) show PL and Raman images of the MoS_2/SiO_2 device, which intensities are very uniform throughout the device in both figures. Interestingly, the PL emission is higher for the MoS_2/BN devices than for the MoS_2/SiO_2 device.

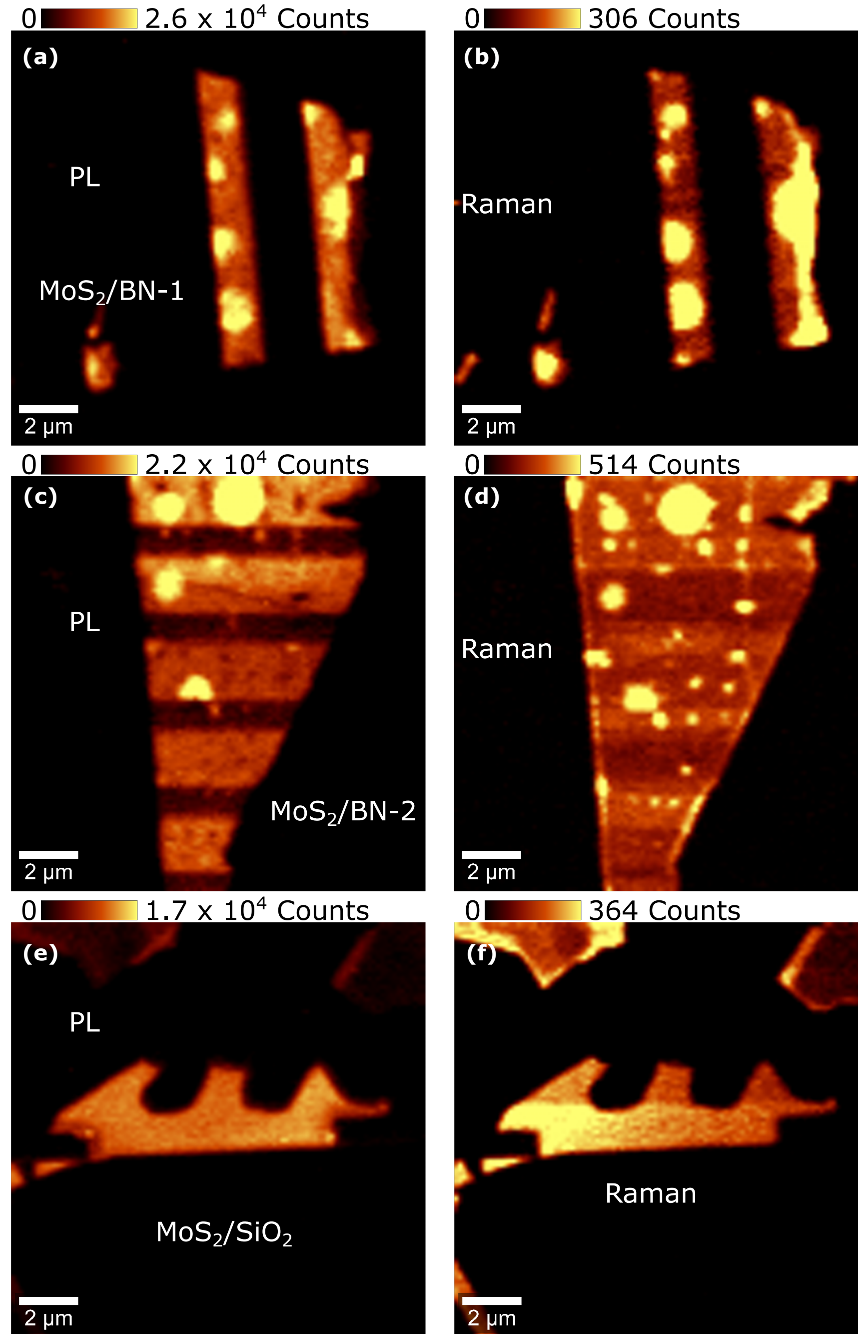

Figure 3.7: **Photoluminescence and Raman images**. Photoluminescence and Raman images of the devices under study. The photoluminescence images show the integrated area of the intensity of the maximum photoluminescence peak, while the Raman images show the integrated area of the intensity of the A' peak. Photoluminescence images of the MoS_2/BN-1, **(a)**, MoS_2/BN-2, **(c)**, and MoS_2/SiO_2, **(e)**, devices. Raman images of the MoS_2/BN-1, **(b)**, MoS_2/BN-2, **(d)**, and MoS_2/SiO_2, **(f)**, devices. The measurements are done with a 457 nm laser, ≈ 1 μm spot size and fluence of 340 $\mu W/\mu m^2$.

3.3 Electrical characterization

The final fabrication step is the insertion of MoS_2 FETs in a chip holder. We wire bond the FETs, contacting them to the chip holder, which we connect to a cryostat. We do all measurements in vacuum ($P \approx 10^{-6}$ mbarr). Before the measurements, we keep the devices in 200 °C for 20 h to improve electrical contact [80]. Before we present the electrical characterization of our devices, we show the electrical measurements setup for clarification, see Fig. 3.8. We use the DC voltage output of a lock-in amplifier to apply a DC voltage in the source (S) of the FET. The generated current in the FET flows toward the drain (D), which is connected to a pre-amplifier. The pre-amplifier is grounded and convert the current signal in an amplified voltage signal, which is measured by a multimeter (Keithley 2000). Finally, we use a DC voltage source (Keithley 2400) to apply a gate voltage.

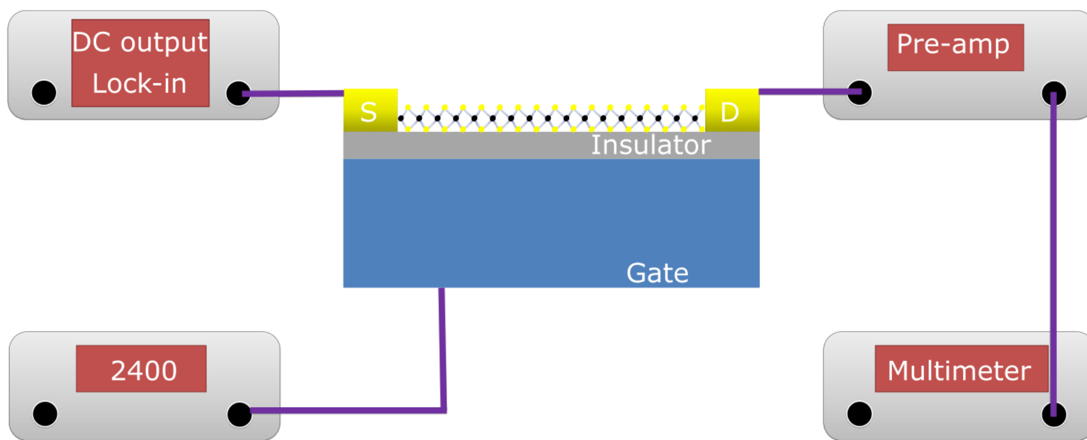

Figure 3.8: **Electrical measurements setup.**

By measuring I_{SD} vs V_{SD} curves, we get information of the quality of the electrical contacts. For example, Schottky contacts present exponential I_{SD} vs V_{SD} curves, while Ohmic contacts show a linear form [81]. Generally, Ohmic contacts are synonyms of high-quality contacts [80, 81]. To check if the contacts of the MoS_2 FETs are working accordingly, we measure I_{SD} vs V_{SD} curves. Fig. 3.9 shows I_{SD} vs V_{SD} measurements for the MoS_2/BN-1, Fig. 3.9(a), MoS_2/BN-2, Fig. 3.9(b), and MoS_2/SiO_2, Fig. 3.9(c), devices. All devices show linear response in the range used, so we have reasonable contacts.

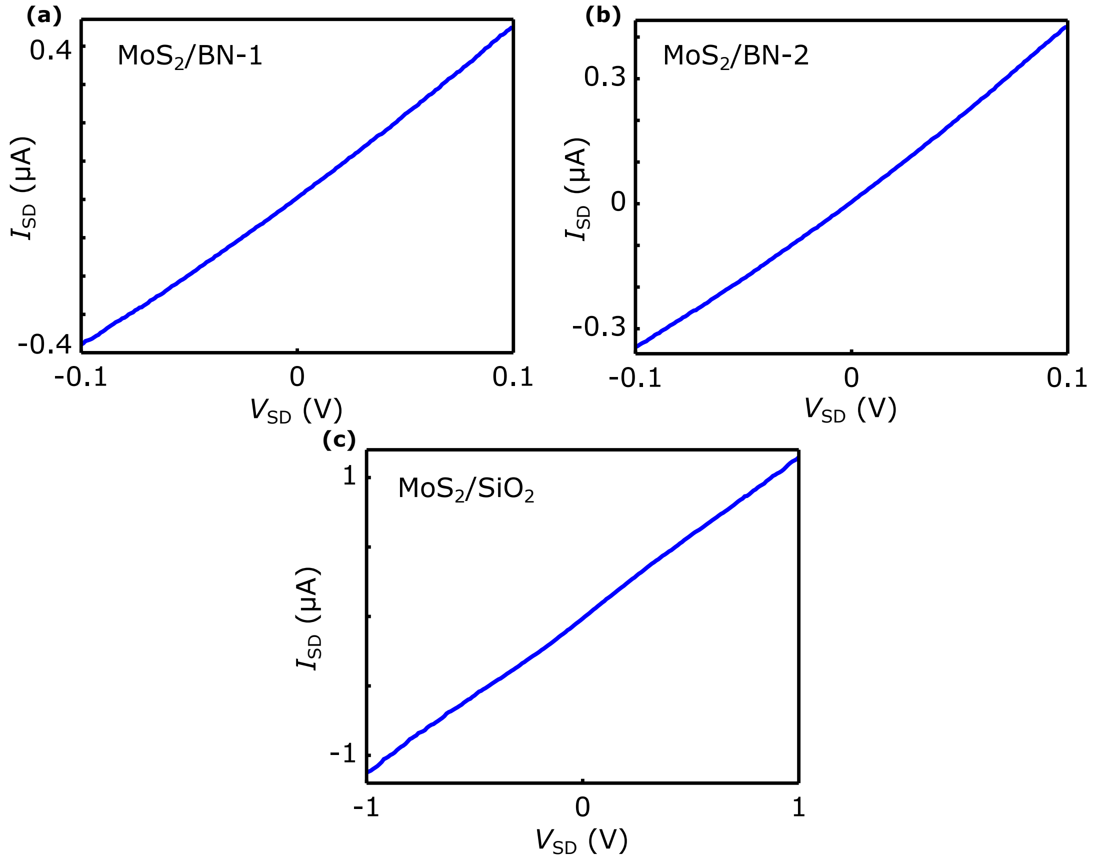

Figure 3.9: $\boldsymbol{I_{\mathrm{SD}}}$ **vs** $\boldsymbol{V_{\mathrm{SD}}}$ **measurements**. I_{SD} vs V_{SD} measurements for the MoS_2/BN-1, **(a)**, MoS_2/BN-2, **(b)**, and MoS_2/SiO_2, **(c)**, devices. In all measurements $V_{\mathrm{BG}} = 0\,\mathrm{V}$

To obtain significant parameters of the MoS_2 FETs, like their mobility, threshold voltages, and the presence of hysteresis, we measure σ vs V_{BG} curves, see section 2.2. Fig. 3.10 shows σ vs V_{BG} curves for the MoS_2/BN-1, Fig. 3.10(a), MoS_2/BN-2, Fig. 3.10(b), and MoS_2/SiO_2, Fig. 3.10(c), devices. The blue circus represents experimental data acquired when V_{BG} is swept from negative to positive values, while red marks represents experimental data acquired when V_{BG} is swept from positive to negative values. In Fig. 3.10, the dashed

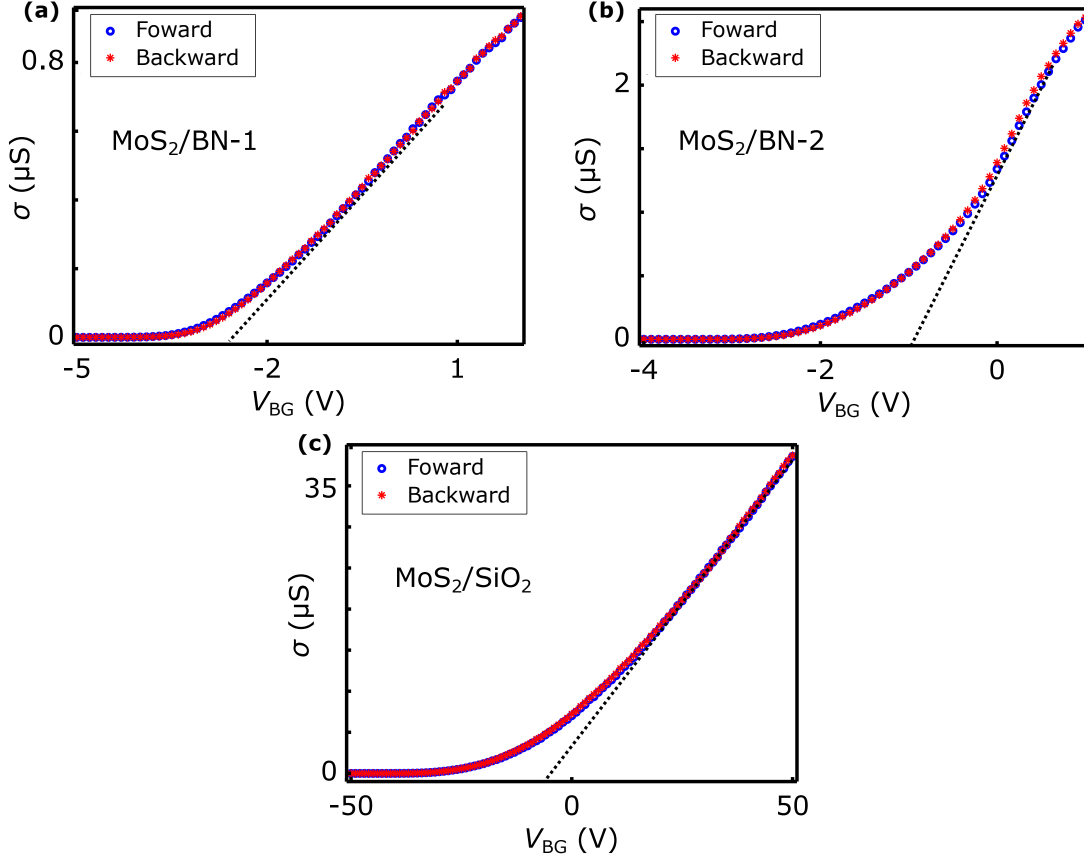

Figure 3.10: **σ vs V_{BG} measurements**. σ vs V_{BG} measurements for the MoS_2/BN-1, **(a)**, MoS_2/BN-2, **(b)**, and MoS_2/SiO_2, **(c)**, devices. The black dashed lines represents the line extrapolation of curves. For the MoS_2/BN-1 and MoS_2/BN-2 devices, $V_{SD} = 0.1\,V$, and for the MoS_2/SiO_2 device, $V_{SD} = 1\,V$.

lines correspond to the line extrapolation of the linear part of the curves. We obtain the threshold voltage (V_{th}) from the interception of the linear extrapolation with the x axis. For the MoS_2/BN-1 device we obtain V_{th} ranging from -2.2 V to -2.9 V, for the MoS_2/BN-2, $V_{th} \approx -0.9$ V and for the MoS_2/SiO_2 V_{th} varies from -3.9 V to -14.4 V. So, all devices are n-type. Furthermore, from Fig. 3.10, it is also possible to evaluate the device mobility using the formula $\mu = \frac{1}{C} \times \frac{d\sigma}{dV_{BG}}$ where $C = \epsilon_0 \epsilon_i / d$, ϵ_0 is the vacuum permittivity, ϵ_i is the insulator dielectric constant (considered 3.9 for both BN and SiO_2) and d is the insulator thickness (28 nm for BN and 285 nm for SiO_2). For the MoS_2/BN-1 device we achieve values of μ ranging from 1 cm^2/V.s to 2 cm^2/V.s, for the MoS_2/BN-2, 12 cm^2/V.s, and for the MoS_2/SiO_2, from 60 cm^2/V.s to 70 cm^2/V.s. It is counter intuitive that the mobility is higher for devices on SiO_2 substrate than on BN. However the Schottky barriers mislead the real value of the mobility, so we believe that the schottky barrier on the MoS_2/SiO_2 device

is much lower than on the MoS_2/BN devices. Another information that we can extract from a σ vs V_{BG} curve is the hysteresis. Hysteresis occurs in a transfer curve, if it follows different paths when we sweep the gate voltage in different directions. Generally, the presence of hysteresis is due to interfacial traps or adsorbed molecules [82–84]. The applied electric field polarizes these contaminants differently according to the direction of the field, generating hysteresis in transfer curves. There is no detectable hysteresis in Fig. 3.10, which is a indicator of the absence of adsorbed molecules on the channel and interfacial traps [82–84] with the substrate.

3.4 Photocurrent setup

In chapter 4 we use two photocurrent setups to perform the measurements. We use the setup of Fig. 3.11 to measure photocurrents with a static laser (the position of the laser is fixed during the measurements). In the setup of the Fig. 3.11, we use a continuum wave (CW) laser with $\lambda = 488\,\text{nm}$ (2.54 eV). The laser beam passes through some mirrors and an objective of 50× magnification focus the beam on the device (spot size of 1 μm). Again, the device is on a cryostat, and we keep the device in vacuum as described in section 3.3.

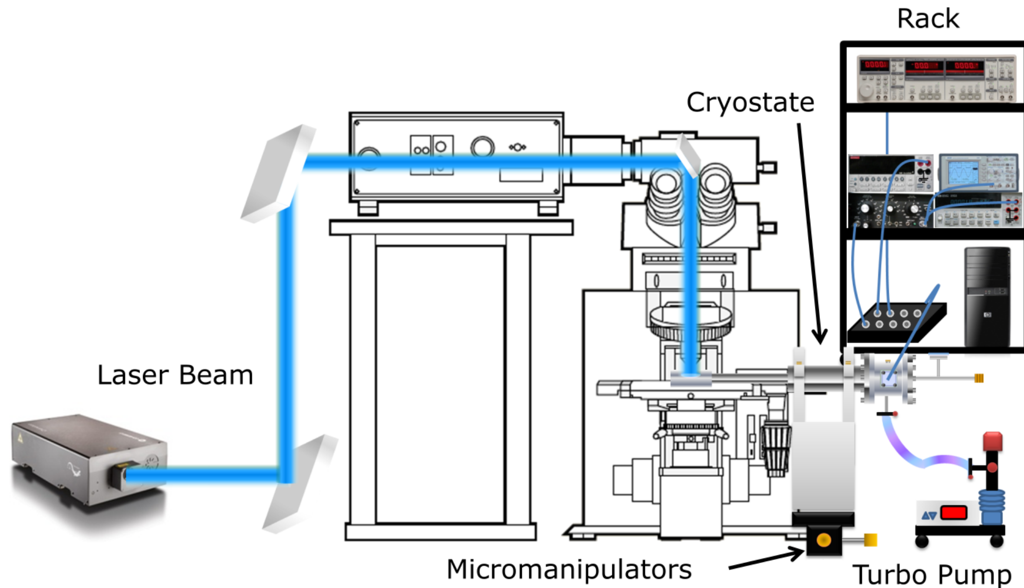

Figure 3.11: **Setup for the photocurrent measurements**.

On the other hand, we use the setup of Fig. 3.12 to scan the device with the laser, forming a photocurrent image. We name this technique of scanning photocurrent microscopy (SPCM). We use a CW laser, with $\lambda = 561\,\text{nm}$ (2.21 eV) laser that generates a beam that passes through a chopper working at 3001 hz. Then, the beam goes through a pair of collimator lens and are reflected by the scanning mirrors. So, the beam splitter partially reflects the beam to a photomultiplier and partially transmits to the device. A 50× objective focus the transmitted light on the device (1 μm spot size). We connect a voltage source to the source of the device, and we connect the drain to the lock-in. The combination of applied

bias and the laser, modulated by the chopper, generates an alternate photocurrent in MoS_2, which is measured by the lock-in. As the scanning mirrors scan the device, a photocurrent image is simultaneously generated with an optical image, forming the SPCM measurement.

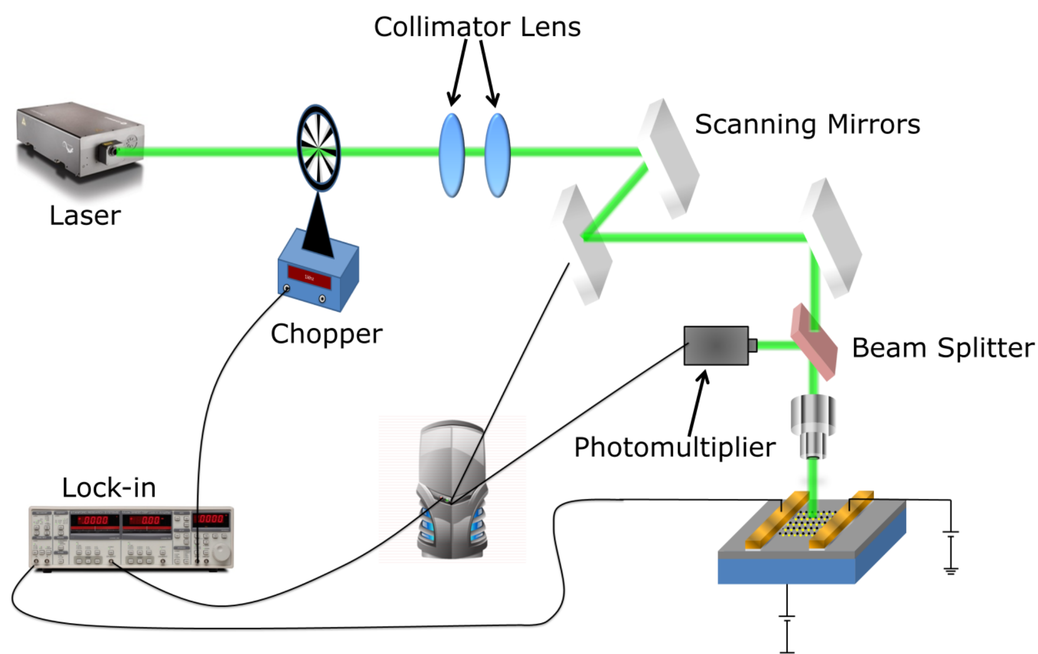

Figure 3.12: **Setup for the SPCM**.

Chapter 4

Results and discussion

In this chapter, we describe and discuss our results. We elaborate that we can increase the density of charges of MoS_2 FETs by simultaneous applications of gate voltage and laser exposure, a photo-induced doping phenomenon that we call the photodoping effect. In the first part of this chapter, we show that we can control the photodoping effect with gate voltage, during laser exposures, in MoS_2/BN devices. From the gate-modulation of the photodoping, we can generate distinct conductive states, which are associated with memory states. Thus, we use the modulation of the photodoping effect to show a new memory phenomenon in FET devices that we denominate of photomemory effect. We then propose a phenomenological model, supported by several experimental evidence, that explain our results. We also point that the photodoping generation and the photomemory states are persistent, retaining up to 50 % of the "recorded" information for more than ten years. Furthermore, we note that the gate voltage can also be used, with the laser off, to amplify and modulate the memory on/off ratio, demonstrating the power of the electric control of the photodoping effect. Next, we show that we can observe a stronger photodoping effect in the MoS_2/SiO_2 device. Finally, we show that we can also control the photocurrent generation in a MoS_2/SiO_2 device spatially.

4.1 The photomemory effect

We begin this chapter by applying the optoelectronic properties of MoS_2 transistors in a photomemory effect. The photomemory effect consists of the modulation of the conductance of a monolayer MoS_2 field effect transistor via a simultaneous application of light and electrostatic gate potential. Along the thesis, we show evidence that the primary mechanisms for the photomemory rely on the manipulation of a charging effect at the gate-insulator interface (the interface between the insulator and the material of the gate terminal). The photomem-

ory is non-volatile, and its architecture is the FET, which is simple and accessible. Also, our photomemory devices have novel operation features, because we use the gate voltage to both "record" and "read" the memory information independently.

We start by describing the photomemory device. To apply MoS_2 in photomemory operations, we use FETs that are Van der Waals heterostructures consisting of a monolayer MoS_2 supported by a high-quality hexagonal Boron Nitride crystal (BN), see Fig. 2.3(a), Fig. 3.3(a) and Fig. 3.3(b). In this case, we use a graphite crystal to provide a flat back gate electrode. Finally, Fig. 4.1(a) shows the photomemory device..

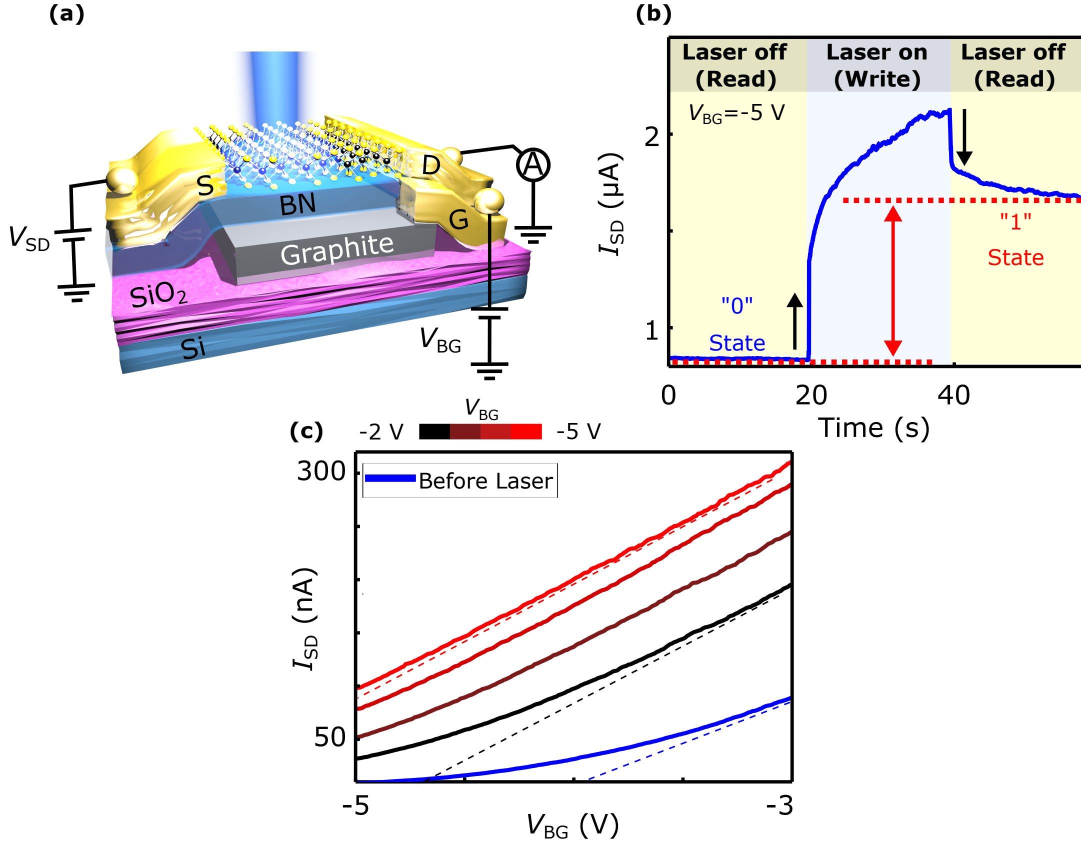

Figure 4.1: **PPC and photodoping**. **(a)**, sketch of the photomemory device. **(b)**, time resolved photocurrent, laser exposure at 488 nm with fluence of 60 $\mu W/\mu m^2$. The parameters are $V_{BG} = -5\,V$ and $V_{SD} = 0.1\,V$. **(c)**, I_{SD} vs V_{BG} curves before laser exposure, blue curve, and after laser exposures with V_{BG} values defined in the color bar. For **(c)** we do laser exposures with a 488 nm laser for 20 s (laser fluence of 60 $\mu W/\mu m^2$).

The photomemory effect is due to the gate-modulation of to the persistent photocurrent (PPC) discussed in section 2.3. So, we now consider the process of photocurrent generation in the MoS_2 FET. Fig. 4.1(b) shows a typical time-resolved photocurrent measurement of the MoS_2/BN device. Initially, we measure the standard current (I_{SD}) in dark conditions, then we illuminate the device using the laser ($\lambda = 488\,nm$) for 20 s, setting $V_{BG} = -5\,V$. A careful analysis of the current as a function of time reveals that two optical processes are generating the photocurrent in the photomemory device. First, there is a rapid increase of I_{SD} due to excitation of electron-hole pairs in the MoS_2 channel (see vertical black arrow), then a second and slow process that starts to dominate the photocurrent. The same trend occurs

when the laser is turned off. There is a rapid collapse of I_{SD}, due to the recombination of the electron-hole pairs, then a prolonged decay process that leads to a persistent photocurrent (PPC). We associate the mechanism of PPC to a photodoping effect, which we will discuss later. For now, note that the device before and after the laser exposure exhibit different conductivity states: after the exposure, I_{SD} is higher than before exposure at the same V_{SD} and V_{BG}. In this way, in Fig. 4.1(b) we can ascribe photomemory states "0" and "1" for the conductivity states before and after laser exposure, respectively. In this chapter we use the laser $\lambda = 488\,\text{nm}$ (2.5 eV) in all optoelectronic measurements, except in a few experiments that we mention the use of different lasers.

Now, we shall associate the PPC to a photodoping effect, and how we can "record" photomemory states by using a simultaneous application of gate voltage application and laser exposure. First, we measure a transfer curve of our device before any laser exposure, see the blue curve in Fig. 4.1(c). We then expose the device to the laser with $V_{\text{BG}} = -2\,\text{V}$ for 20 s. After the exposure, we measure a new transfer curve with the laser off, see the black curve in Fig. 4.1(c). The linear extrapolation of the blue and black curves, see dashed lines, shows that the laser exposure changes the threshold voltage of the device, turning it more n-doped, see Fig. 2.3. So, the laser induces a doping effect in MoS_2, a process we call photodoping. The photodoping defines new I_{SD} values for each V_{BG}. Such permanent modification represents the "recording" of a memory state. We repeat laser exposures in the same fashion described above but with V_{BG} varying from $-3\,\text{V}$ to $-5\,\text{V}$ during the laser exposures. This procedure increases, even more, the doping of MoS_2, see Fig. 4.1(c), demonstrating that the gate voltage application during laser exposures tunes the photodoping effect. Thereby, we denominate of "record" operations the combined actions of laser exposures and gate voltage applications. We denominate the memory state of the device before any laser exposure, the blue curve in Fig. 4.1(c), as "OFF" state. So, the memory device is "blank" while in the "OFF" state. On the other hand, we denominate of "ON" states any memory state measured after a "record" operation.

To completely characterize the gate-dependence of the photomemory effect, we do laser exposures on our device applying gate voltages in a range of $-5\,\text{V} \leq V_{\text{BG}} \leq 5\,\text{V}$, see Fig. 4.2(a). Fig. 4.2(a) illustrates the change of the density of free charges acquired for the MoS_2 after every photomemory "record" operation as compared to the intrinsic density of charge of the photomemory. Here, we use equation 2.4 to evaluate the photodoping. We do the "record" operations in the same fashion as Fig. 4.1(c), but in Fig. 4.2(a) we achieve the initially "recorded" state by applying a $V_{\text{BG}} = 0\,\text{V}$ during the laser exposure. We name this "recorded" "ON" state as "0" state. We "record" the other photomemory states by changing the gate voltages in a range of $-5\,\text{V} \leq V_{\text{BG}} \leq 5\,\text{V}$, following the sequence indicated by the arrows. The negative gate voltages are used to monotonically increase the density of charge to set a "1" state and the positive gate voltages are used to reduce the density of charge and to restore the initial "0" state. We name the process of charge injection in the MoS_2 channel as a "write" operation (red arrow). We perform the "write" operation by exposing the device to the laser with an applied negative gate voltage. We denominate the process of removing the charges as an "erase" operation (blue arrow). The gate-"erase" operation is performed

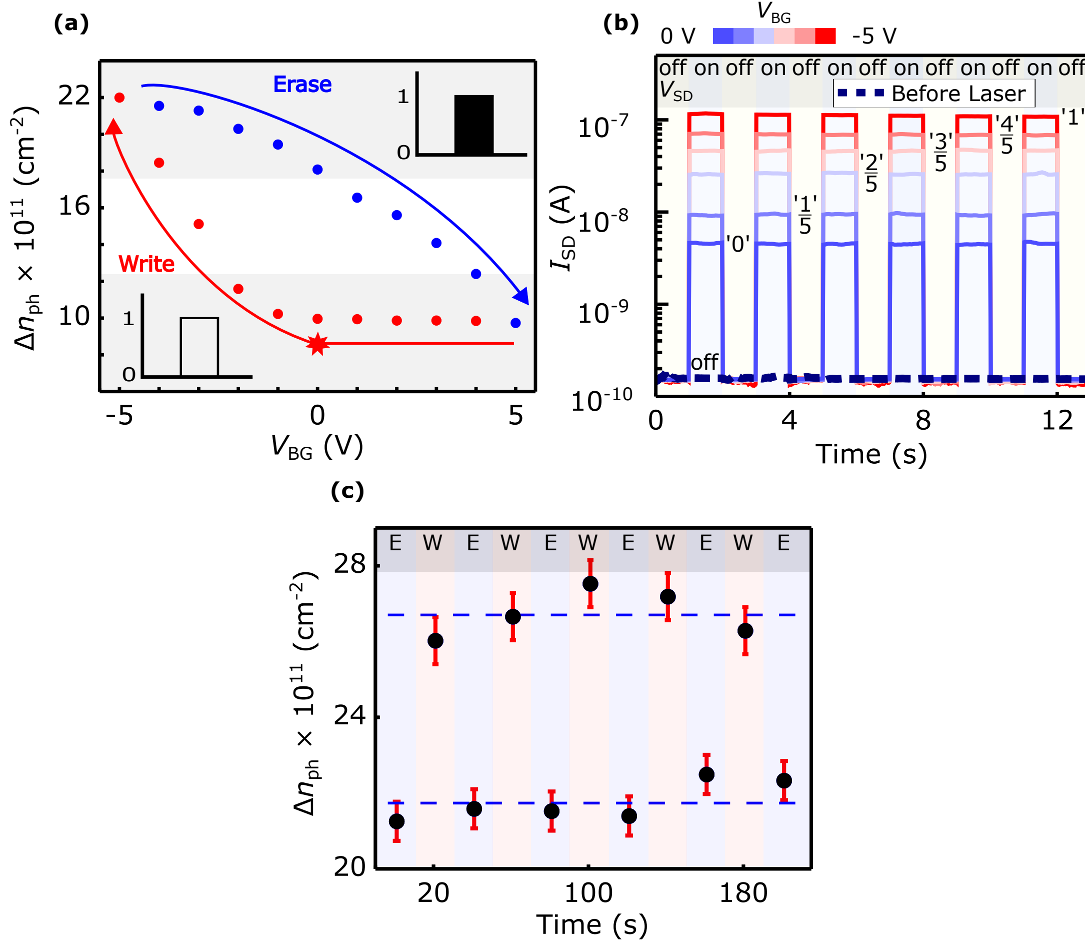

Figure 4.2: **Gate-tunable photomemory**. **(a)**, Δn_{ph} vs V_{BG} curve. First, the point $V_{BG} = 0\,V$ is measured, and then the arrows indicate the followed applied gate voltages. For figure **(a)** there is a 488 nm laser exposure on each point for 20 s (laser fluence of 60 $\mu W/\mu m^2$). **(b)**, multilevel photomemory, gate values from 0 V to -5 V are used for the writings and 20 s of laser exposure, laser fluence of 700 $\mu W/\mu m^2$. For the “readings”, a gate value of -4 V and bias pulses of 0.1 V are applied. **(c)**, “write”-“erase” operations, for $V_{BG} = -5\,V$ and $V_{BG} = 5\,V$, respectively, and 20 s of laser exposure (fluence of 700 $\mu W/\mu m^2$).

right after writing the “1” state, but with gate voltages larger than $V_{BG} = -5\,V$ during the laser exposures. For example, in Fig. 4.2(a) the “erase” operations are executed with several laser exposures applying $V_{BG} = -4\,V, -3\,V$ ... $5\,V$. In Fig. 4.2(a) the gate-“erase” operation does not remove the photodoping completely, but partially (Δn_{ph} does not go to zero, instead $\Delta n_{ph} = 10 \times 10^{10}\,cm^{-2}$ after the “erase” operation). Fig. 4.2(a) also shows that the “record” operations with distinct gate voltages generate particular Δn_{ph} values. The different Δn_{ph} correspond to distinct photomemory states.

The dependence of the photomemory states on the V_{BG} used during the “record” operations enables multilevel memory states operation. Multilevel memory is a memory capable of storing more than a single bit of information in a single memory element. However, we must point out that it is not the aim of this work to explore multilevel memory operation in details. We depict in Fig. 4.2(b) the application of MoS_2 FET on multilevel memory operation by employing current “readings”. In Fig. 4.2(b), the dashed black line represents the I_{SD} from the “OFF” state, which is measured by applying $V_{SD} = 0.1\,V$ and $V_{BG} = -4\,V$ before any laser exposure. We “record” multilevel memory states by applying laser exposures using V_{BG} from 0 V to -5 V, with increments of -1 V. We name these states of “0”, “$\frac{1}{5}$”, “$\frac{2}{5}$” ... “1”. After each “record” operation, we “read” the photomemory state by measuring the current through the device at the same electrostatic condition used when we “read” the “OFF” state. The difference here is that we use pulses of $V_{SD} = 0.1\,V$ for 2 s spaced by 2 s to show that the information is stored in the photomemory even when no V_{SD} is applied.

Although multilevel memory states are interesting, here they are illustrated only to demonstrate the usefulness of the gate-tunability property of the photomemory. However, for practical memory operations, it is straightforward to explore the reliability in the “write”-“erase” operations between the binary memory states. In this case, we generate the binary “1” and “0” states by applying $V_{BG} = -5\,V$ and $V_{BG} = 5\,V$, respectively, during the 20 s laser exposures. We show the reproducibility and reliability of the “write”-“erase” operations of the binary memory states in Fig. 4.2(c), that presents a sequence of successful “write”-“erase” cycles. These results confirm the device robustness. In Fig. 4.2(c), it is also represented the error bars in each “record” operation. The error bars show that the “write”-“erase” operations generate distinguishable photomemory states.

4.2 The mechanism of the photomemory effect

In this section, we discuss the process of photodoping that possibly generates the PPC and photomemory effects in our MoS_2 FETs. PPC is not a consensus topic. The most discussed explanations for the PPC in MoS_2 is either due to the photo-induced charge transfer from adsorbed gases to the MoS_2 channel [56] or due to the Coulomb interaction with defects at the insulator surface [13,48,54,59,61,85–87]. We believe that the interactions with adsorbed gases are not a valid explanation in our devices as there is no hysteresis in the σ vs V_{BG} curves when we sweep the voltage in forward and backward directions [82] (see Fig. 3.10). We believe that the interactions with defects at the insulator surface are not the dominant mechanism, as the devices have a low density of defects when compared with the photodoping

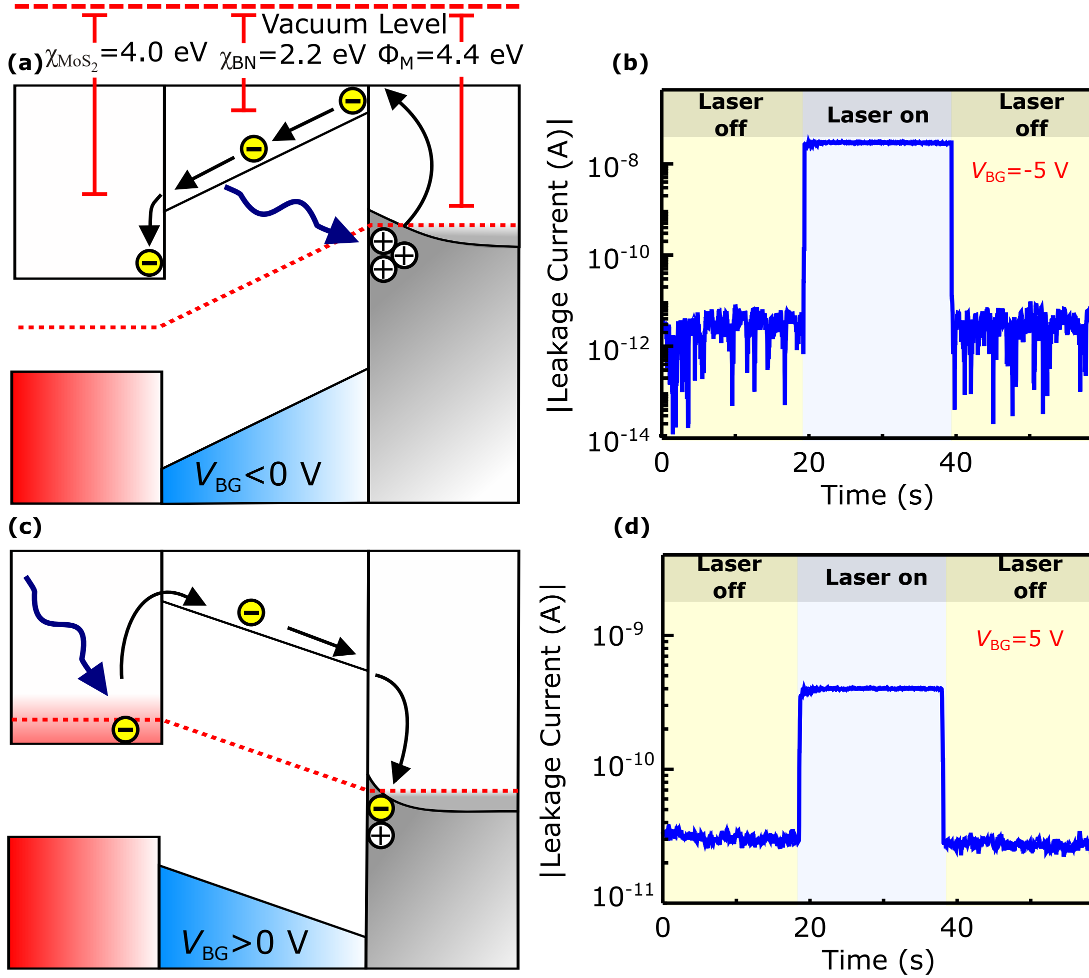

Figure 4.3: **Physical model for the photodoping**. **(a)**, energy band diagram for the MoS_2/BN/graphite junction as a function of position for $V_{BG} < 0\,V$. **(b)**, photogenerated leakage current, $V_{BG} = -5\,V$, $\lambda = 488\,nm$ and fluence of 60 $\mu W/\mu m^2$. **(c)**, energy band diagram for the MoS_2/BN/graphite junction as a function of position for $V_{BG} > 0\,V$. **(d)**, photogenerated leakage current, $V_{BG} = 5\,V$, $\lambda = 488\,nm$ and fluence of 60 $\mu W/\mu m^2$.

observed in our work. Furthermore, the fact that we measure the photodoping in a clean and flat BN/Graphite substrate [9] reinforces this statement. Also importantly, we use a thick BN ($\sim 30\,nm$, see section 3.1), which prevents tunneling as the primary mechanism for charge trapping. On the other hand, tunneling mechanisms are crucial in flash devices and other tunneling-based memory devices, see the reference [42–44] and the discussion in section 2.4.

Thus, after testing several hypotheses, we strongly believe that the photodoping in our MoS_2 FET occurs via a controlled way of trapping holes in the gate-insulator interface. We clarify this mechanism by drawing the energy band diagram of the MoS_2-BN-graphite heterojunction, with the potentials $V_{BG} < 0\,V$, Fig. 4.3(a), and $V_{BG} > 0\,V$, Fig. 4.3(b), applied in the graphite relative to the MoS_2. In Fig. 4.3(a) we depict the MoS_2 (χ_{MoS_2}) and BN (χ_{BN}) electron affinities, which are 4.0 eV [88] and 2.2 eV [67], respectively. We also depict the graphite work function $\Phi_M = 4.4$ eV [89–91]. There are two energy barriers in the heterojunction of Fig. 4.3, between MoS_2 and BN, which energy is $\chi_{MoS_2} - \chi_{BN} = 1.8$ eV, and

between BN and graphite, that is $\Phi_M - \chi_{BN} = 2.2$ eV. We also show in the gate-insulator junction the bending of the graphite band, that generates a built-in electric field. For $V_{BG} < 0\,V$, photons with sufficient energy ($E_{ph} > \Phi_M - \chi_{BN} = 2.2\,eV$) promote the electrons from the gate-insulator interface to the conduction band of BN. The applied negative gate voltage drives these photoexcited electrons through the conduction band of BN to the MoS_2 channel, but some holes generated during the photoabsorption process remain trapped at the gate-insulator interface by the electric field of the gate-insulator junction. The positively charged layer generates photodoping in the MoS_2 channel, see Fig. 4.3(a). According to this energy diagram description, we predict that we should observe a photo-generated leakage current under laser exposure between the drain and gate electrodes. This fact is verified in our experiments, as depicted in Fig. 4.3(b) that exhibits a 10^{-8} A leakage current during the laser exposure.

For $V_{BG} > 0\,V$, the MoS_2 channel is n-doped. When we turn the laser on, photons with enough energy ($E_{ph} > \chi_{MoS_2} - \chi_{BN} = 1.8\,eV$) promote electrons from MoS_2 to the conduction band of BN, see Fig. 4.3(c). In this case, the gate-field drives these electrons through the conduction band of BN to the gate-insulator junction, recombining with some of the trapped holes, reducing the photodoping. We do not achieve the photodoping reduction process totally, in Fig. 4.2(a), because the built-in electric field of the gate-insulator junction prevents some of the electrons to recombine. Fig. 4.3(d) shows that, for $V_{BG} > 0\,V$, we can also observe a photo-generated leakage current during the laser exposure. For $V_{BG} > 0\,V$ the photo-generated leakage current is smaller than for $V_{BG} < 0\,V$. The fact that the density of states of MoS_2 is smaller than the graphite flake's may explain this result. The proposed model in Fig. 4.3 explains the results of Fig. 4.2(b), which shows that the applied negative gate bias increases the photodoping, whether positive gate bias reduces the photodoping. Moreover, the threshold energy for the photodoping generation ($E_{ph}^{th} = \Phi_M - \chi_{BN} = 2.2\,eV$) in Fig. 4.3 matches our experimental results. Indeed, we measure the photodoping with laser energies of 1.6 eV, and 2.5 eV, which are below and above the threshold energy for photodoping, respectively.

Fig. 4.4 shows σ vs V_{BG} curves which express a comparison between generated photodopings with a 1.6 eV, Fig. 4.4(a), and 2.5 eV, Fig. 4.4(b), lasers before (blue curves) and after (red curves) exposure. Such comparison shows that the 1.6 eV laser induces negligible doping ($\Delta n_{ph} \approx 10^{10}\,cm^{-2}$) compared to induced by the 2.5 eV laser ($\Delta n_{ph} \approx 10^{12}\,cm^{-2}$). In all these measurements, the laser is kept on the device for thirty minutes, with fluence of $700\,\mu W/\mu m^2$ and $V_{BG} = -5\,V$, to ensure a saturation of the photocurrent and the photodoping effect. So, the results of Fig. 4.4 agrees with our theoretical prediction. Although the proposed model suits well our results, we do not discard that other minor effects may co-occur. For example, there is a negligible, but not null, photodoping generated with the 1.6 eV laser ($\Delta n_{ph} \approx 10^{10}\,cm^{-2}$). This small photodoping may be due to the excitation of defects from the MoS_2 channel, for example, [35]. However, mostly the gate-insulator interface contains the physics of the photodoping.

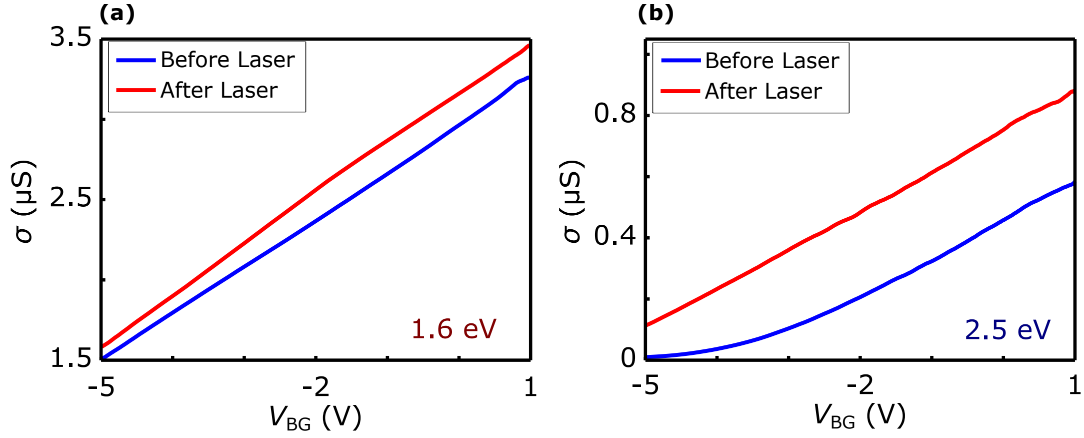

Figure 4.4: **Photodoping comparison using different laser excitation**. **(a)**, σ vs V_{BG} curves, before (blue) and after (red) a 1.6 eV laser. **(b)**, σ vs V_{BG} curves, before (blue) and after (red) a 2.5 eV laser. In these measurements $V_{\mathrm{SD}} = 0.1\,\mathrm{V}$. During the laser exposure, we use $V_{\mathrm{BG}} = -5\,\mathrm{V}$, laser fluence of 700 μW/μm^2 and exposure time of thirty minutes.

4.3 The photomemory performance

We have described how the gate voltage can be used to define binary memory states during "record" operations. Now, we show that we can also use the gate voltage during memory "readings". More importantly, we show that the gate voltage can tune the memory on/off ratio (this parameter was defined in section 2.4). We can read the photomemory states by measuring Δn_{ph} or by measuring I_{SD}. However, by measuring I_{SD} instead of Δn_{ph}, we have the advantage of adjusting the gate voltage, choosing the highest memory on/off ratio. This fact is better observed in Fig. 4.5(a), where we show transfer curves of the photomemory device on a log scale. In the inset, we plot the same curves, but on a linear scale. In blue, we plot a transfer curve before the laser exposure. By extrapolating the I_{SD} curve it is possible to estimate the threshold voltage (V_{th}) as $V_{\mathrm{th}}^{\mathrm{OFF}} = -2.2\,\mathrm{V}$, see the inset in Fig. 4.5(a). We define the blue curve (before laser exposure) as a memory "OFF" state. After this, the MoS_2 device is exposed to the laser beam with $V_{\mathrm{BG}} = -5\,\mathrm{V}$ until the photocurrent saturates. The typical time for photocurrent saturation is thirty minutes. The reason for waiting for the photocurrent saturation is to reach the best response of our device. Then, we turn the laser off and repeat the transfer curve measurement. The data from the transfer curve after the laser exposure (red curve in Fig. 4.5(d)) displays a significant increase of I_{SD} at all applied gate conditions. We estimate by extrapolating the data that the new threshold voltage is $V_{\mathrm{th}}^{\mathrm{ON}} = -9.8\,\mathrm{V}$, see the inset in Fig. 4.5(d). Also, the expected change in the density of charge of MoS_2 due to photodoping in Fig. 4.5(a) is $\Delta n_{\mathrm{ph}} = 6 \times 10^{12}\,\mathrm{cm}^{-2}$, evaluated by the equation 2.4. We define the red curve (after laser exposure) as a memory "ON" state.

Also importantly, for the same memory state in Fig. 4.5(a), rather "ON" or "OFF", we have several I_{SD} values for the different V_{BG} used. So, we can adjust the V_{BG} to optimize the memory "reading". Fig. 4.5(b) depicts a $I_{\mathrm{ON}}/I_{\mathrm{OFF}}$ vs V_{BG} curve. This curve was obtained by dividing the blue and red curves in Fig. 4.5(a) and can be interpreted as a memory on/off ratio curve. The $I_{\mathrm{ON}}/I_{\mathrm{OFF}}$ ratio changes from 10, for positive gate voltages, to values up to 10^6, for negative gate voltages. Observe that the high modulation of the memory on/off

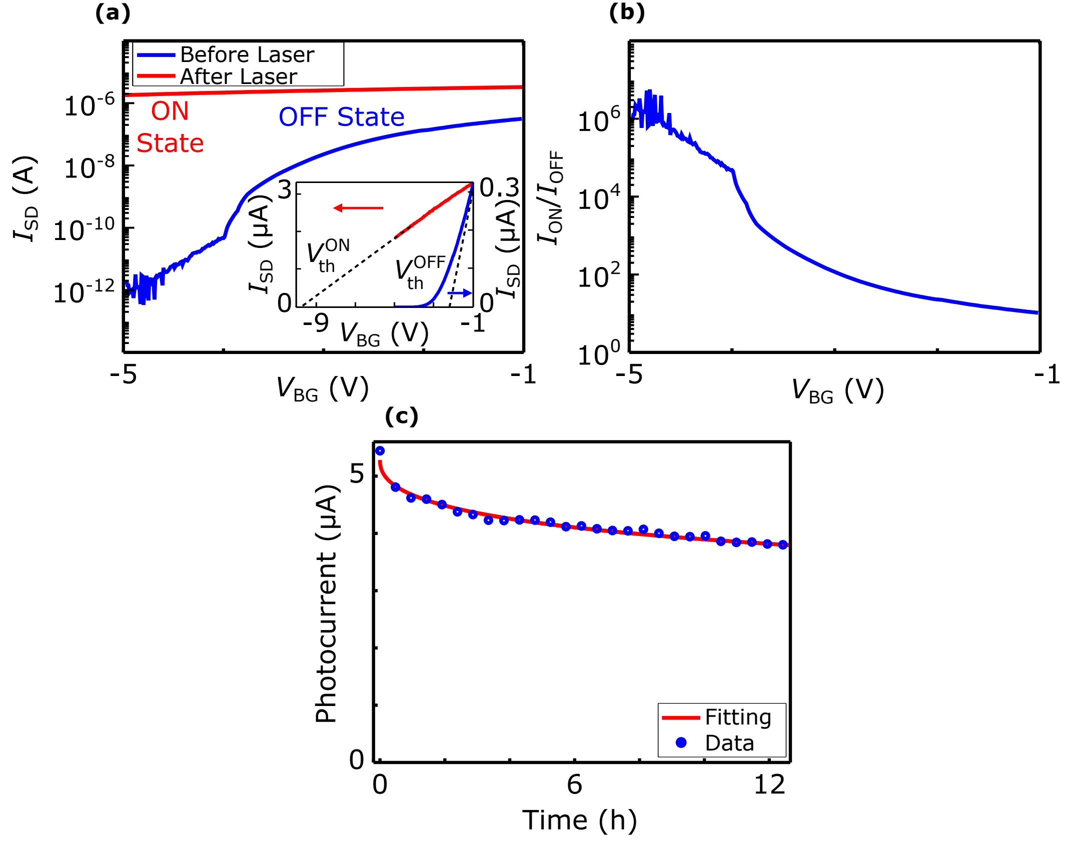

Figure 4.5: **Memory parameters**. **(a)**, The I_{SD} vs V_{BG} measurements on a log scale before (blue) and after (red) the laser exposure, $V_{SD} = 0.1\,V$. In the inset, the same measurements but on a linear scale. The red curve is measured after the 488 nm laser exposure with fluence of 700 $\mu W/\mu m^2$ and $V_{BG} = -5\,V$ until photocurrent saturation. **(b)**, I_{ON}/I_{OFF} ratio as a function of the gate voltage. **(c)**, photocurrent decay after the photodoping induced by the 488 nm laser with fluence of 700 $\mu W/\mu m^2$ until photocurrent saturation. The parameters $V_{BG} = 0\,V$ and $V_{SD} = 0.1\,V$ are used for this measurement.

ratio with gate voltage is an attribute of the photomemory effect. In flash architectures, for example, the gate voltage is used only to define the memory states, and can not be used during the memory "readings".

In Fig. 4.5(a) we obtain a high on/off ratio by selecting two photomemory states, "ON" and "OFF", that are quite different from each other ($\Delta n_{\mathrm{ph}} = 6 \times 10^{12}\,\mathrm{cm}^{-2}$). On the other hand, in Fig. 4.2(a), we sweep between the "ON" states named "0" and "1" photomemory states. The photodoping values of these states differ only by $1 \times 10^{12}\,\mathrm{cm}^{-2}$, which may not give a memory on/off ratio as high as 10^6. However, the photomemory device is gate-tunable. In this way, during the memory "reading" we can set a V_{BG} value slightly lower than the V_{th} of the "0" state, which turns the FET off (low current regime) in this state. After a "write" operation, the FET goes to the high current regime. So, I_{SD} in the "1" state increases by orders of magnitude for the same V_{BG} used to "read" the "0" state. Consequently, this procedure allows for obtaining high values of memory on/off ratio.

Another crucial figure of merit of a memory device is the memory retention time. To estimate that, we measure the MoS_2 photocurrent decay over time with the laser off, after "recording" a memory state, see the blue dots in Fig. 4.5(c). Before measuring the decay of the photocurrent, we perform a "write" operation in our device with $V_{\mathrm{BG}} = -5\,\mathrm{V}$. Next, we turn the laser off and keep measuring I_{SD} with $V_{\mathrm{BG}} = 0\,\mathrm{V}$. After 15 h the photocurrent barely decreases, suggesting that the photomemory state is permanent. So, the photomemory is a non-volatile memory. To estimate the memory loss over ten years, we employ an exponential decay fit, the red line in Fig. 4.5(c), see equation 2.13. From the fitting, we predict that the reminiscent memory current percentage for the photomemory device is approximately 50% of the initial photocurrent, see equation 2.14. Thus, the devices can retain 50% of the memory for ten years. These values are much better than the MoS_2 flash memory architectures', where the retention percentage is in the range of 15-30% [44–46, 67].

To finalize the description of the photomemory effect, we need to present the response time of the photomemory device. Fig. 4.6 shows I_{SD} vs Time curves while the "write" and "erase" operation occurs. The dots represent experimental data acquired, and the lines are exponential fittings, see equation 2.13. Fig. 4.6(a) is a "write" operation with a 488 nm laser, fluence of 700 $\mu\mathrm{W}/\mu\mathrm{m}^2$, and $V_{\mathrm{BG}} = -5\,\mathrm{V}$. The "write" operation is observed by an increase in current. Fig. 4.6(b) corresponds to an "erase" operation under the same conditions of Fig. 4.6(a) but with $V_{\mathrm{BG}} = 5\,\mathrm{V}$, and the "erase" operation is observed by an decrease of the current. From the fittings, the obtained values of τ for "write" and "erase" operations are four and fourteen minutes, respectively. Although these values are high, the gate-tunability property of the photomemory effect allows parallel "record" operations. Fig. 4.2(a) shows that the generation of the photomemory states "0" and "1" are defined by the gate voltage applications. So, in a given multi-cell device, composed of several photomemory cells, we can apply $V_{\mathrm{BG}}= -5\,\mathrm{V}$ in the cells that we desire a "1" state and $V_{\mathrm{BG}}= 5\,\mathrm{V}$ in the cells that we desire a "0" state. So, by using a laser beam we can "record" all the cells at the same time. Moreover, with a short exposure time of 20 s we can still obtain a high photodoping of $\Delta n_{\mathrm{ph}} \approx 10^{12}\,\mathrm{cm}^{-2}$ (see Fig. 4.2(a)).

At this time we can describe in more details the photomemory device, which is composed

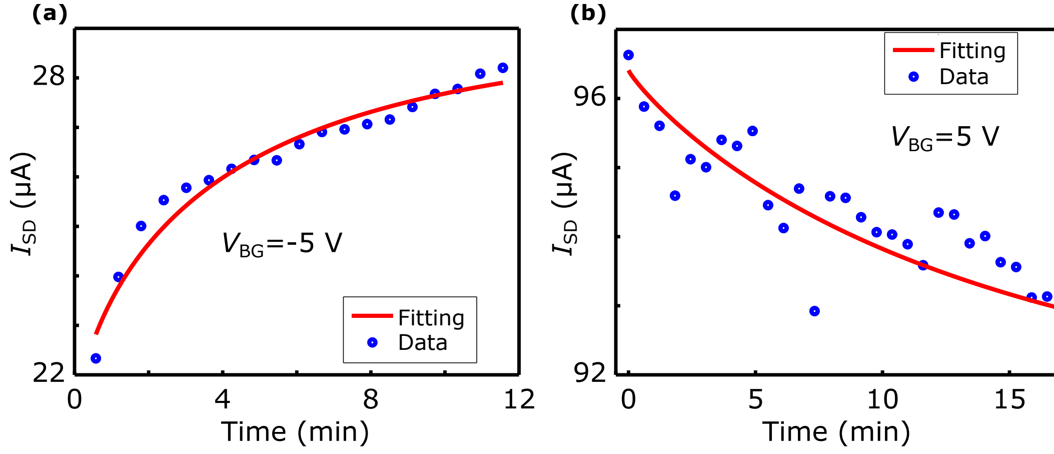

Figure 4.6: **Response time. (a)**, I_{SD} vs Time, in "write" operation. For this measurement, $V_{SD} = 0.1\,\text{V}$ and $V_{BG} = -5\,\text{V}$. **(b)**, I_{SD} vs Time, in "erase" operation. For this measurement, $V_{SD} = 0.1\,\text{V}$ and $V_{BG} = 5\,\text{V}$. In both measurements, we use a 488 nm laser, fluence of 700 $\mu\text{W}/\mu\text{m}^2$.

mainly of two elements in the FET architecture. One element is the gate-insulator interface, where possibly the charges are trapped inducing the photodoping. The other element is the semiconductor channel, from which we "read" the photomemory states. In this way, we can design better photomemory devices by choosing other gate-insulator interfaces that can provide higher values of photodoping and retention time. Furthermore, the choices of semiconductors with better mobility and subthreshold swing would enable us to achieve higher memory on/off ratio values.

4.4 The photodoping in the MoS_2/SiO_2 device

As we have discussed in section 4.2, the photodoping is an effect from the gate-insulator interface. Thus, we can extrapolate the photodoping effect to other transistors, using different components in its structure. Furthermore, we can improve some of the photodoping features by engineering the materials of the gate-insulator interface. Here, we show that we can also observe a photodoping generation in the MoS_2/SiO_2 device, which is composed of MoS_2 on a SiO_2/Si substrate, see Fig. 3.3. We also show that the magnitude of the photodoping and reminiscent memory percentage values of this device are higher than the MoS_2/BN devices'. Fig. 4.7(a) shows transfer curves of the MoS_2/SiO_2 device before (blue) and after (red) the laser exposure. By extrapolating the I_{SD} curve we estimate the threshold voltage as $V_{th}^0 = -10\,\text{V}$ before laser exposure.

After the laser exposure, the device displays a significant increase of I_{SD} at all applied gate conditions. There is a strong shift of the threshold voltage (V_{th}) towards V_{BG} out of the range of the experiment. We estimate by extrapolating the data that the initial $V_{th}^0 = -10\,\text{V}$ shifts to $V_{th}^L = -130\,\text{V}$. Also, the expected change in the density of charge of the MoS_2 due to photodoping is $\Delta n_{ph} = 9 \times 10^{12}\,\text{cm}^{-2}$, see equation 2.4. This value is higher than the photodoping obtained from the MoS_2/BN device ($\Delta n_{ph} = 6 \times 10^{12}\,\text{cm}^{-2}$), and is compared to doping values obtained using high-K dielectrics, see reference [16]. Besides, photodoping

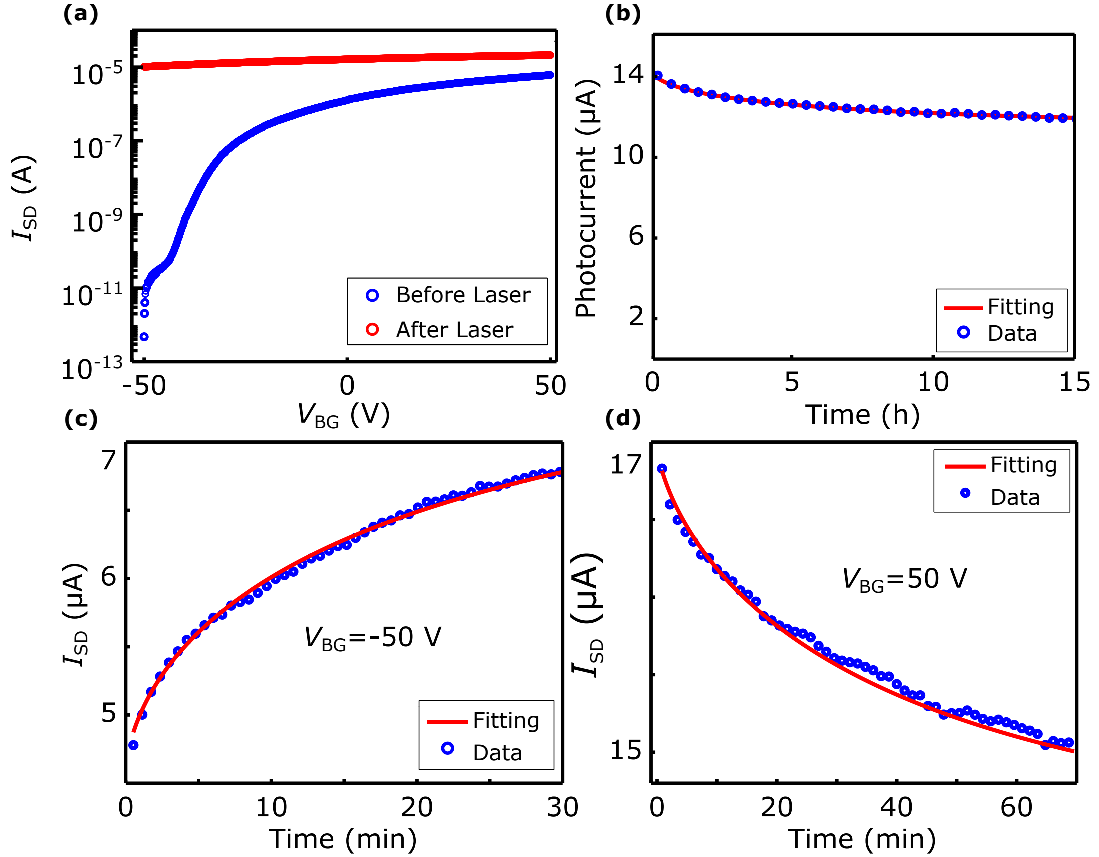

Figure 4.7: **Photodoping from the SiO_2/Si substrate**. **(a)**, I_{SD} vs V_{BG} measurements before (blue) and after (red) the laser exposure for the MoS_2/SiO_2 device, $V_{SD} = 1\,V$. The red curve is measured after the 488 nm laser exposure with fluence of 700 $\mu W/\mu m^2$ and $V_{BG} = -50\,V$ until photocurrent saturation. **(b)**, photocurrent decay for the MoS_2/SiO_2 device after the photodoping induced by the 488 nm laser with fluence of 700 $\mu W/\mu m^2$ and $V_{BG} = -50\,V$ until photocurrent saturation. The parameters $V_{BG} = 0\,V$ and $V_{SD} = 1\,V$ are used for this measurement. **(c)**, I_{SD} vs Time, in "write" operation. For this measurement, $V_{SD} = 1\,V$ and $V_{BG} = -50\,V$. **(d)**, I_{SD} vs Time, in "erase" operation. For this measurement, $V_{SD} = 1\,V$ and $V_{BG} = 50\,V$. In both measurements, we use a 488 nm laser, fluence of 700 $\mu W/\mu m^2$.

enables the acquisition of high doping values by simply exposing the MoS_2 FET to a laser beam, which has a scientific and technology appeals.

Next, we study the time-decay of the photodoping by presenting, in Fig. 4.7(b), the photocurrent decay over time, see the blue dots in Fig. 4.7(b). The measurement is performed after the photocurrent saturation by laser exposure and $V_{BG} = -50\,V$. After 15 h the photocurrent barely decays suggesting that the photodoping in the MoS_2/SiO_2 device is permanent. To estimate the photodoping loss over ten years, we employ an exponential decay fit, the red line in Fig. 4.7(b). From the fitting, we predict that the reminiscent current for the MoS_2/SiO_2 device is approximately 80% of the initial photocurrent. This value is even higher than the obtained for the MoS_2/BN device (50%).

In Fig. 4.7(c) and Fig. 4.7(d) we show the gate-modulation of the photodoping for the MoS_2/SiO_2 device, by means of I_{SD} vs Time curves. The dots represent the acquired experimental data, and the lines are exponential fittings, see equation 2.13. In Fig. 4.7(c) we do a laser exposure with a 488 nm laser, fluence of 700 $\mu W/\mu m^2$, and $V_{BG} = -50\,V$. This procedure is similar to the “write” operation in Fig. 4.6(a). In Fig. 4.7(d) we do a laser exposure under the same conditions of Fig. 4.7(c) but with $V_{BG} = 50\,V$. This procedure is similar to the “erase” operation in Fig. 4.6(b). From the fittings, the obtained values of τ for the “write” and “erase” operations are twenty-three minutes and forty-three minutes, respectively. These values are much higher than for the MoS_2/BN device and are a bottleneck of the MoS_2/SiO_2 device.

According to our model, proposed in Fig. 4.3, the physics of the photodoping effect is contained mostly in the gate-insulator interface. As this interface is crucial for the photodoping generation, we predict that devices which do not have a gate-insulator interface do not generate photodoping. To check this key point experimentally we can compare the photodoping generation of two devices, with and without a gate terminal. However, it is important that both devices have the same insulator substrate. The simpler way to build these devices is by using a standard MoS_2 FET on a SiO_2/Si substrate, and by using a MoS_2 sample on top of glass (SiO_2 device). So, the first device has a gate electrode and the second does not have, while both have the same insulator (SiO_2). Fig. 4.8(a) shows a sketch of the Si/SiO_2 device and Fig. 4.8(b) shows an I_{SD} vs Time curve for this device. In a similar way to 4.1(b), the Si/SiO_2 device shows a prominent PPC due to the photodoping effect. On the other hand, Fig. 4.8(c) shows a sketch of the SiO_2 device, and Fig. 4.8(d) shows a I_{SD} vs Time curve of this device. In contrast to Fig. 4.8(b), Fig. 4.8(d) presents a very sharp and fast response. So, the SiO_2 device presents negligible PPC. This result reinforces our model that the gate-insulator interface is crucial for the photodoping generation.

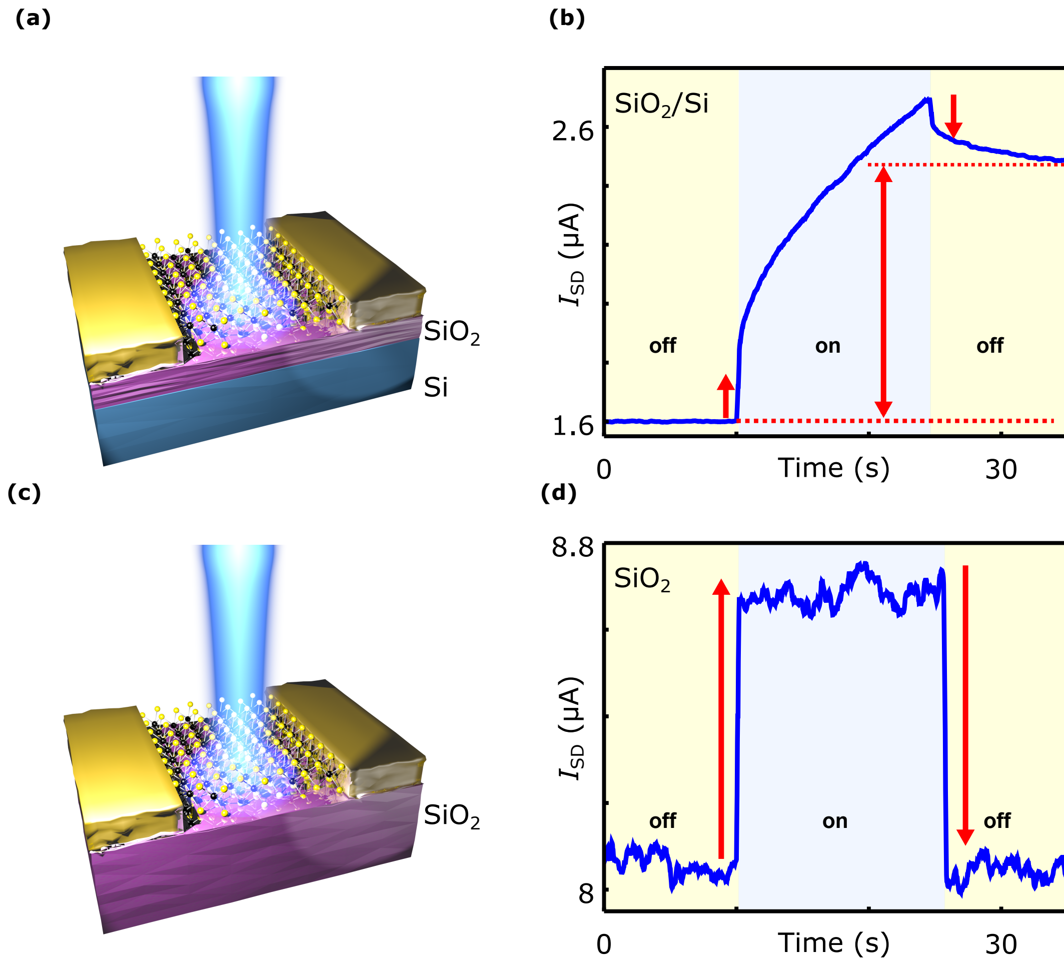

Figure 4.8: **Photodoping and the gate-insulator interface**. **(a)**, sketch of the SiO_2/Si device. **(b)**, time-resolved photocurrent for the SiO_2/Si device, $V_{BG} = -10$ V. **(c)**, sketch of the SiO_2 device. **(d)**, time-resolved photocurrent for the SiO_2 device. In both measurements we use a 488 nm laser with a fluence of 60 μW/μm^2.

4.5 Local photodoping

So far, we have used the photodoping to generate memory states in MoS_2 FETs. However, we did not explore how is the spatial distribution of the photodoping. Here, we show that the photodoping is a local effect and that this local phenomenon can control the photocurrent generation of MoS_2 spatially. To visualize the spatial distribution of the photodoping, we use a scanning photocurrent microscopy (SPCM) setup. We observe the photodoping effect indirectly because in SPCM measurements the laser beam passes through a chopper working at 3 kHz (see section 3.4), which imposes a very short excitation time that prevents the direct observation of the photodoping. Recall that we can only obtain measurable values of photodoping after a 10 s laser exposure in a single point, see Fig. 4.7(c). Therefore, what we observe in a SPCM image is predominantly the photocurrent due to the electron-hole pairs generation in MoS_2. Fig. 4.9(a) shows a SPCM measurement for the MoS_2/SiO_2 device using a 561 nm (2.2 eV) laser with fluence of $100\,\mu W/\mu m^2$. Notice that we use the MoS_2/SiO_2 device instead of the MoS_2/BN device, because the MoS_2/SiO_2 device has a longer channel and its photodoping generation is higher. A gate voltage of $-70\,V$ is applied in the MoS_2 while the measurement is performed to ensure that the sample is almost depleted of charges.

During the SPCM measurement, the laser dwells at each point for small periods of time ($\tau \approx 500\,ms$), which generates a small, but not null, photodoping in the whole sample. To prevent distortions in the SPCM images due to the small photodoping generation during the SPCM measurement, we normalize all the measurements of Fig. 4.9 with the photocurrent from the ordinary region indicated by the arrow. We depict a band diagram of the region delineated by the dashed circle in the inset of Fig. 4.9(a) . When photons strike the sample, electrons can be excited from the valence to the conduction band generating excess carriers. Hence a photocurrent can be measured. Indeed, the photocurrent is generated throughout the sample, but higher values are attained close to the contact interface due to Schottky electric field [92].

After measuring the photocurrent spatially, we expose the delimited area (dashed circle) in Fig. 4.9(a) with the 561 nm laser with a fluence of 1000 $\mu W/\mu m^2$ and $V_{BG} = -50\,V$ for five minutes to ensure that a photodoping is generated. After that, we repeat the SPCM measurement with the same parameters used in Fig. 4.9(a) and a notoriously suppression of the photocurrent occur predominantly at that exposed region. We can explain this local effect qualitatively via a photodoping process. The inset of Fig. 4.9(b) depicts the band diagram of MoS_2 in the dashed circle area that shows why the photocurrent is suppressed. After inducing the photodoping in the dashed area, the states in the conduction band are filled, which limits the photoexcitation of electron-hole pairs. Thus, there is a suppression of the photocurrent in the exposed area (see Fig. 4.9(b)), indicating that the photodoping effect occurs locally in the MoS_2 channel. Similarly to Fig. 4.9(a) and Fig. 4.9(b), Fig. 4.9(c) and Fig. 4.9(d) present SPCM measurements before and after a laser exposure in the area delimited by the dashed circle for five minutes (fluence of 1000 $\mu W/\mu m^2$ and $V_{BG} = -50\,V$), respectively. Again, a suppression of the photocurrent in the exposed area shows that the photodoping is a local effect and that we can control the photocurrent spatially. We adjust the color bar of Fig. 4.9(a) and Fig. 4.9(b), and of Fig. 4.9(c) and Fig. 4.9(d), accordingly

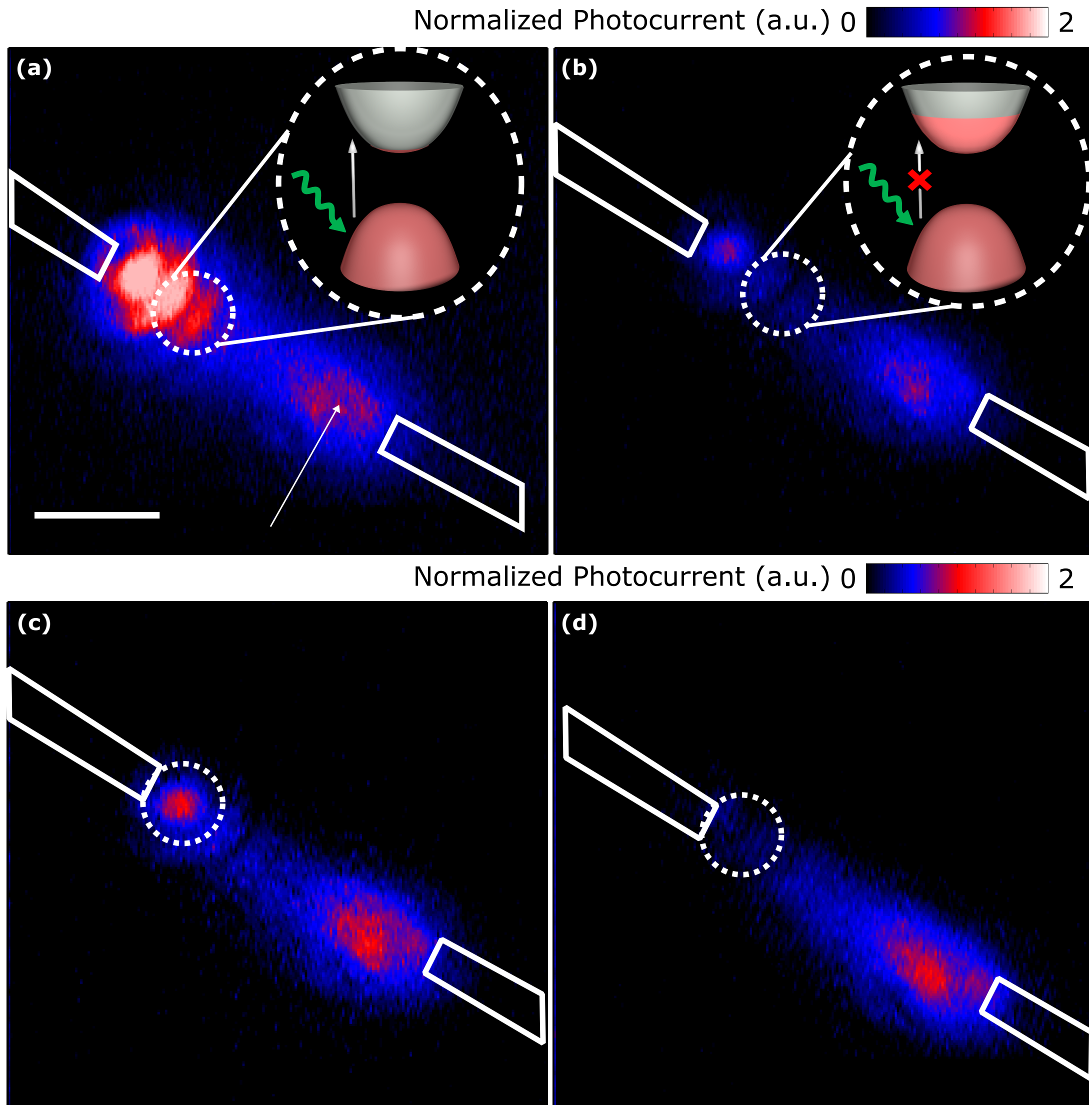

Figure 4.9: **Spatial control of the photocurrent**. **(a)**, scanning photocurrent microscopy measurement for the MoS_2/SiO_2 sample. The excitation laser wavelength is 561 nm with a fluence of 100 $\mu W/\mu m^2$. In this measurement we use $V_{BG} = -70\,V$ and $V_{SD} = 1\,V$. In the inset is the band structure of the region inside the dashed circle. **(b)**, SPCM measurement from the same region and conditions as in **(a)**, but after exposing the region inside the dashed circle with the $\lambda = 561\,nm$ laser, fluence of 1000 $\mu W/\mu m^2$ and $V_{BG} = -50\,V$ for five minutes. Scale bar is 4 μm. **(c)** and **(d)**, SPCM measurements before and after the laser exposure in the dashed circle of **(c)** for five minutes, $\lambda = 561\,nm$, fluence of 1000 $\mu W/\mu m^2$ and $V_{BG} = -50\,V$. Again, the excitation laser wavelength is 561 nm with a fluence of 100 $\mu W/\mu m^2$ during the SPCM measurement.

to highlight the photocurrent suppression after the laser exposure.

Chapter 5

Partial conclusions

In part I of this thesis, we studied the electric-induced modifications of the optical absorption in MoS_2 transistors that unraveled photocurrent and photodoping effects. We revealed that persistent photocurrent, a phenomenon that is still under debate, is due to the photodoping effect. By making simultaneous applications of the gate voltage and laser exposure, we controlled the photodoping generation. This process caused a modulation of MoS_2 conductance, leading to the creation of photomemory states with possible use in multilevel memories. We proposed a model, supported by experimental evidence, that explains the photodoping and photomemory effects. According to this model, these effects are due to a charge trapping at the gate-insulator interface of the FET. We also studied the performance of the photomemory devices. We explained that the gate voltage could be used, with the laser off, during the photomemory "readings", to adjust the memory on/off ratios up to 10^6. We estimated the memory loss, and from our predictions, the photomemory device keeps up to 50% of the memory information for more than ten years. To generalize the photomemory effect to other transistors, we presented photodoping results in a different FET, the MoS_2/SiO_2 device. By using different insulators and materials for the gate, we showed that it is possible to obtain higher photodoping and reminiscent memory retention percentage values. To give another validation of our model, we confirmed that we do not observe persistent photocurrent in a MoS_2 device that does not have a gate-insulator interface. Finally, we used the photodoping effect to control the photocurrent generation at MoS_2 spatially. Our work unravels the optoelectronic effects in MoS_2 transistors and shows their applications in non-volatile memories that expand the possibilities of memory application beyond conventional memory architectures.

Part II

Unraveling Stark and quenching effects of atomic-like emissions in layered talc devices

Chapter 6

Theory

Now we start the second part of this thesis, entitled unraveling Stark and quenching effects of atomic-like emissions in layered talc devices. Here, we show photoluminescence (PL) emissions in talc that are similar to atomic emissions. We also deliberate that we can control them by application of a transverse electric field. This control occurs in two ways, Stark splitting of the energies and a quench of the intensities of the emissions. Therefore, to understand these results we need to expose some essential topics, which we do in this chapter. We start by introducing talc, describing its crystal and electronic structures. Next, we explain the photoluminescence effect, which is vital to comprehend our measurements. Subsequently, we consider the linear Stark effect, which is the mechanism that shifts the emissions in talc. Finally, we take into account the physical phenomena that cause PL quenching.

6.1 Introduction to talc

Talc is a crystalline hydrated magnesium silicate, belonging to the silicate crystals family. We can extract talc from the soapstone rock, and a common pure form of talc has the unit cell chemical formula $Mg_3Si_4O_{10}(OH)_2$. It has several properties, like softness, hydrophobicity, organophilicity, inertness, diverse mineralogical composition and the ability to form plates. All these properties make talc appropriate for many industrial applications such as cosmetics, pharmaceuticals, coatings, paper, ceramics, polymers, and wastewater treatment. Also important, talc is a layered material, so the layers that form talc interact by Van der Waals forces [93]. Thus, it is possible to extract a single layer (monolayer) of talc experimentally [15].

In this thesis, we study talc samples obtained from a typical mine in Ouro Preto (Brazil). Previous works, using similar samples, showed that talc has a triclinic structure [15, 94].

Fig. 6.1 presents the crystal structure of triclinic monolayer talc. This image is taken with permission from [95]. Each talc layer consists of an atomic layer of Mg atoms placed between two quartzlike Si-O layers, with additional hydroxyl units. More precisely, the monolayer talc is an octahedral layer composed of Mg and OH^- between two tetrahedra layers of Si and O.

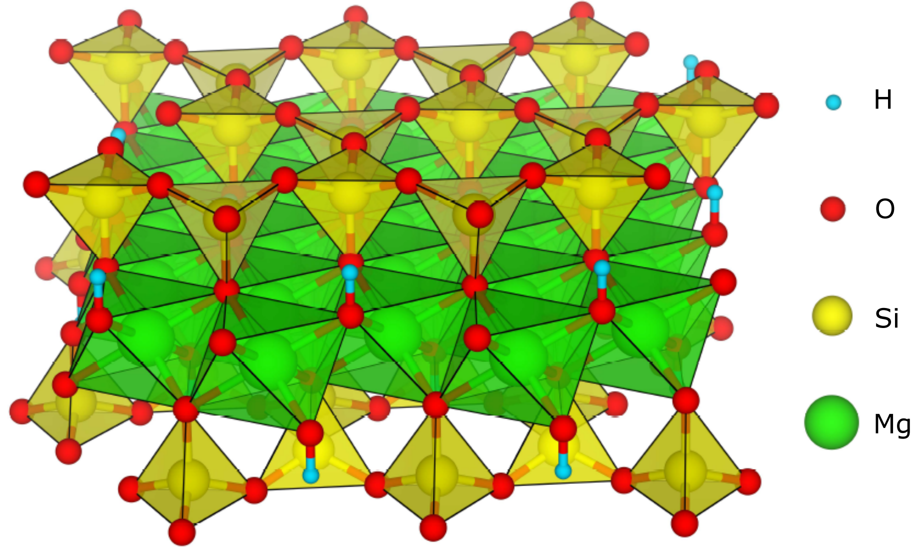

Figure 6.1: **The crystal structure a monolayer talc**. Taken from [95].

In Fig. 6.2(a) we show the bulk structure of talc, taken with permission from [95]. In Fig. 6.2(b), we show the top-view of the triclinic structure of talc. The red arrows correspond to the triclinic $C\bar{1}$ unit cell, while the blue arrows correspond to the triclinic $P\bar{1}$ unit cell. Also, in Fig. 6.2(b) we depict in black lines the zig-zag and armchair directions. The triclinic structure is the Bravais lattice which $a \neq b \neq c$, and $\alpha \neq \beta \neq \gamma$. X-ray measurements in talc give $a = 5.291(1)$ Å, $b = 9.172(1)$ Å, $c = 9.455(1)$ Å, $\alpha = 90.58(1)^\circ$, $\beta = 98.77(1)^\circ$ and $\gamma = 89.99(1)^\circ$ [94].

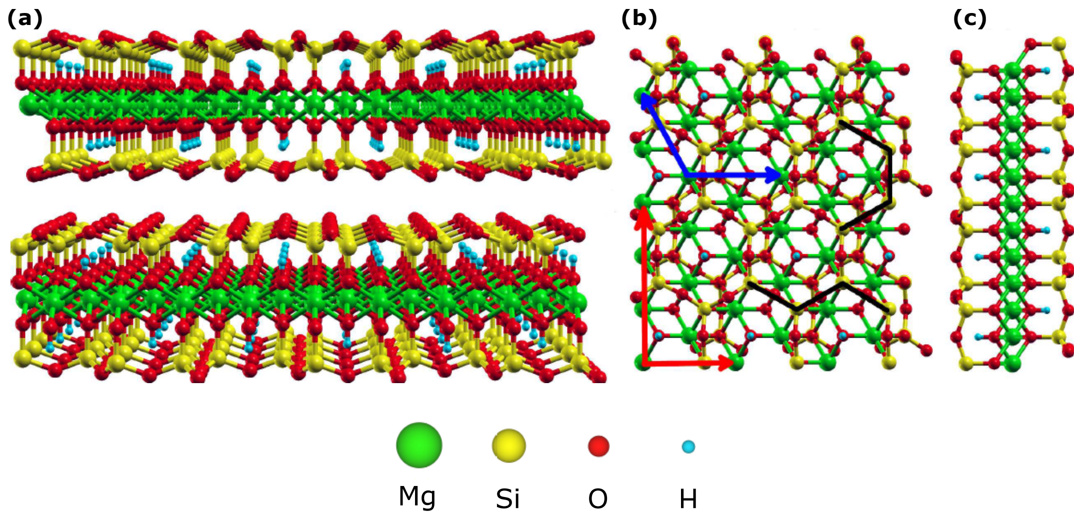

Figure 6.2: **The crystal structure of talc**. Taken from [95]. **(a)**, the structure of bulk talc. **(b)** and **(c)**, top and side-view of the triclinic structure of talc, respectively. In **(b)**, we represent with red and blue arrows the the unit cell of the triclinic C$\bar{1}$ and P$\bar{1}$ structures, respectively. The black lines in **(b)** show the zig-zag and armchair directions.

To understand the electronic properties of talc, we plot in Fig. 6.3 the electronic structures of the bulk, **(a)**, and monolayer, **(b)**, talc, calculated by density functional theory (DFT) [95]. Fig. 6.3 exhibit that the bulk and monolayer crystals have a similar electronic structure. Both are insulators with band gap energy (E_{g}) of approximately 5 eV, and the minimum of the conduction band and maximum of the valence band are located at the Γ point.

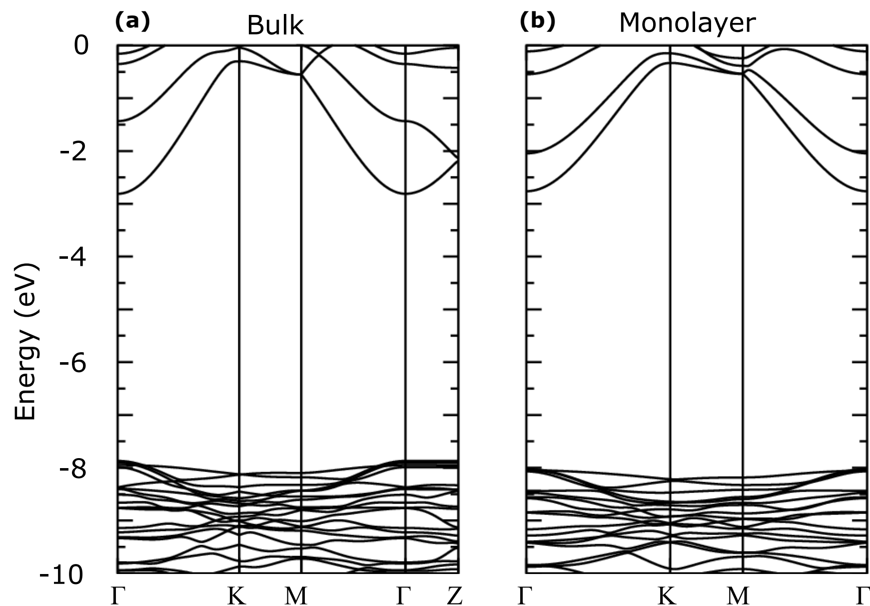

Figure 6.3: **Electronic structure of talc**. Electronic structure of the bulk, **(a)**, and monolayer, **(b)**, talc. Taken from [95].

Talc has natural impurities on its composition, which varies from the mine where we extract talc crystals. The literature reports lots of impurities, mainly Fe and Al, but also traces

of Ni, F, Na, K, Cu, Mn, and others [96–100]. The presence of these impurities changes the properties of talc, as its hydrophobicity, polymer adsorption [98], and its magnetic properties [100]. They may also modify the optical properties of talc, see Fig. 6.4, which shows optical pictures of talc samples with different colors from different mines. For example, Fig. 6.4(a) shows a white talc from North Carolina (USA) [101], Fig. 6.4(b) shows a green talc typically from Ouro Preto (Brazil) [94,102], Fig. 6.4(c) shows a pink talc from Texas (USA) and 6.4(d) shows a black talc from Guangfeng County (China) [103]. Most notably, we do measurements in talc crystals from Ouro Preto (Brazil), that are typically green, see Fig. 6.4(b).

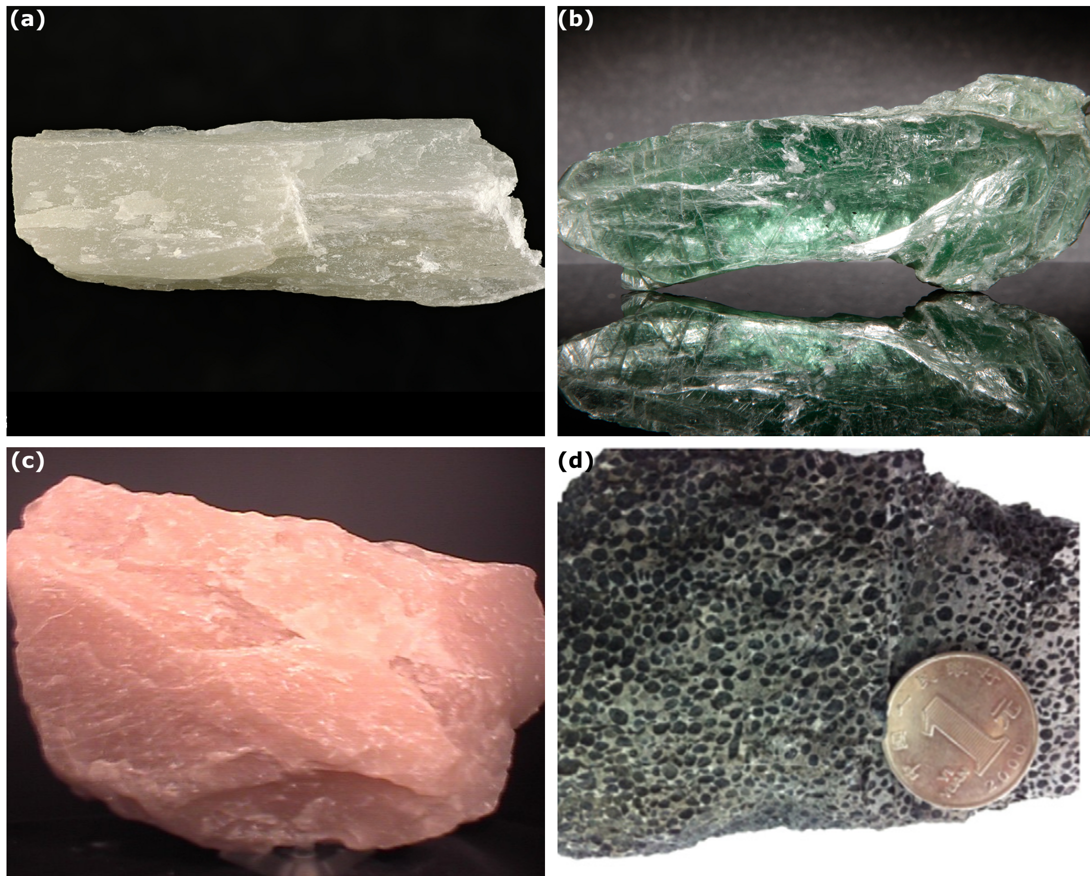

Figure 6.4: **Talc crystals**. Optical images of the white, **(a)** [101], green, **(b)** [102], pink , **(c)** [104], and black, **(d)** [103], talc crystals.

Since 1970, it is known that the layers in talc electrostatically attract by Van der Waals forces [93]. However, only very recently, experimental and theoretical groups from the Federal University of Minas Gerais (UFMG) have isolated a monolayer talc [15]. They have also demonstrated that talc has interesting elastic and mechanical properties. Ever since, research groups specialized in 2D materials started to study talc even further. The reference [105] demonstrates that talc generates spontaneous doping in graphene while keeping the intrinsic quantum properties of this material. Furthermore, the reference [94] explores the hyperbolic properties of talc to uncover surface plasmon-phonon polaritons in a heterostructure of talc and graphene. Here, we make advances in the study of the 2D talc, but on a previously not studied topic in this material: the photoluminescence. We show that electronic transitions in

intrinsic defects in talc generate atomic-like photoluminescence emissions, with a potential application on quantum information. Moreover, we describe an external control of talc PL in two different manners. We tune the energy of the PL by the linear Stark effect. On the other hand, we modulate the intensity of the PL and quench some of the emissions with applications of transverse electric fields.

Next, we briefly describe the photoluminescence effect, which is the essential optical effect that we study in part II.

6.2 Photoluminescence

Atoms emit light by spontaneous emission when electrons in excited states drop down to a lower level by radiative transitions [3]. In crystals, the spontaneous radiative emission process is called luminescence. Several mechanisms generate luminescence, however here we are going to describe only the photoluminescence. The photoluminescence is the luminescence stimulated by photons. So, in this case, photons promote electrons to excited states, which decay by spontaneous emission. The spontaneous emission rate for radiative transitions between two levels is determined by the Einstein A coefficient [3], which gives the radiative emission rate:

$$\left(\frac{dN}{dt}\right)_{\text{Radiative}} = -AN, \tag{6.1}$$

where N is the population of the excited state. The solution of the equation 6.1 is an exponential decay, where the radiative lifetime can be given by $\tau_R = 1/A$. The spontaneous emission occurs through radiative channels (RC), which are the transitions that emit photons during the decay process. However, some transitions go through a non-radiative channel (NC), which do not emit photons. The NC can be phonon-assisted transitions or defect-assisted transitions, for example. In a system that both RC and NC coexist, there is a competition between these processes, decreasing the probability that radiative emissions occur. For this particular case, we can write the luminescence efficiency η_R as:

$$\eta_R = \frac{1}{1 + \tau_R/\tau_{NR}}, \tag{6.2}$$

where τ_{NR} is the non-radiative lifetime. Doing an asymptotic analyses of equation 6.2, we get $\eta_R = 1$, for $\tau_{NR} \to +\infty$, and $\eta_R = 0$, for $\tau_{NR} \to 0$. Therefore, the longer the non-radiative lifetime, the higher the luminescence efficiency.

To better describe the photoluminescence process, in Fig. 6.5 we illustrate this effect for an atomic, Fig. 6.5(a), and crystal, Fig. 6.5(b), systems. In section 8.1, we present PL spectra from talc (which is a crystal) that are similar to atomic emissions, so the differences between the atomic and crystal photoluminescences are crucial for the understanding of our results. Hence, we start describing these emissions, pointing out some differences between them. The photoluminescence process starts by exciting the system with photons with energy (E_{L}) larger than the difference between two atomic states, Fig. 6.5(a), or the bandgap of the solid, Fig. 6.5(b). For the atomic system, the electrons are excited to virtual states

and subsequently decay to an excited atomic level, see Fig. 6.5(a). For the crystal system, photons excite the electrons from the valence band (VB) to the conduction band (CB), then they relax to the bottom of the CB, see Fig. 6.5(b), while the photoexcited holes relax to the top of the VB. Generally, the relaxation process is due to carrier-carrier and carrier-photon scatterings, which imposes a very fast response of the order of femtoseconds [58]. So, after relaxation, the electron-hole pairs can recombine through radiative and non-radiative channels. The electron-hole pairs that recombine by radiative channels emit photons with energy equal to the difference between the two atomic levels, Fig. 6.5(a), or to the bandgap, Fig. 6.5(b). The decay time of the radiative process is of the order of nanoseconds [58], which is longer than the time for relaxation (femtoseconds). So, the carriers relax first, in a fast process, to subsequently recombine. The energy of the emitted photons is independent of the laser excitation energy because the energy difference between the atomic levels and the bandgap of the material are fixed parameter for a given temperature. Consequently, if we want to figure out that an unknown spectrum is due to a PL effect, we need to measure it after several energy excitations. If the energies of the peaks from the spectrum are independent of laser energy, it is probably due to a PL effect.

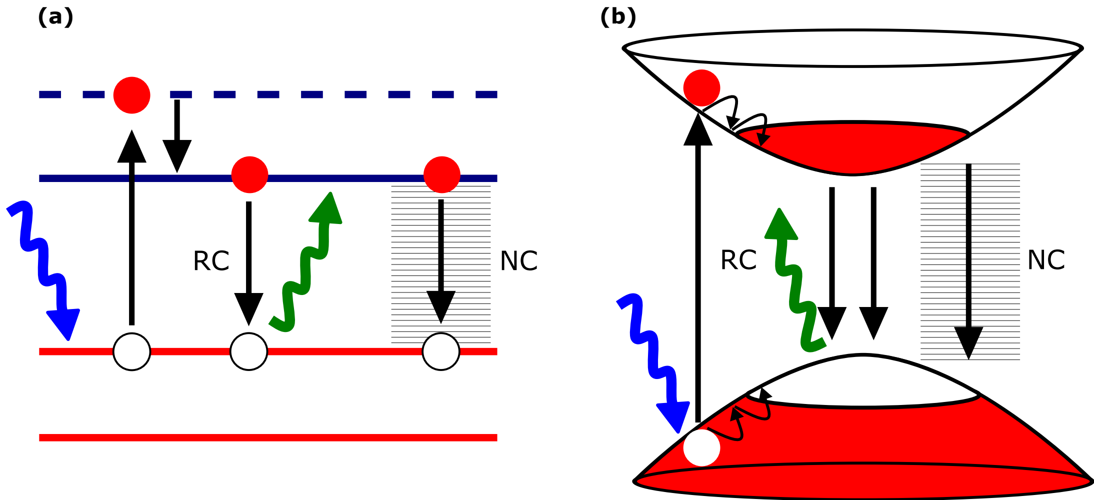

Figure 6.5: **Photoluminescence process**. Photoluminescence in an atomic system, **(a)** and in a crystal system, **(b)**.

To obtain the intensity of the PL, we need to evaluate the equation:

$$I \approx |M|^2 g(\hbar\omega) \times \text{level occupancy factors}, \tag{6.3}$$

where M is the matrix element, that describes the effect of the external perturbation caused by light on the electron, $g(\hbar\omega)$ is the joint density of states, that comes from the Fermi golden rule, and the level occupancy factors refer to the probability that the excited and ground states are filled and empty of electrons, respectively. From the equation 6.3 we can obtain the intensity of the PL of a 3D crystal, which is given by $I \approx (\hbar\omega - E_g)^{1/2} \times exp\left(-\frac{\hbar\omega - E_g}{k_b T}\right)$, where E_g is the bandgap energy [3]. From this last equation, the PL intensity increases abruptly, due to the term $(\hbar\omega - E_g)^{1/2}$, but decays at an exponential rate, due to the expression $exp\left(-\frac{\hbar\omega - E_g}{k_b T}\right)$. Furthermore, the typical full width at half maximum in this

equation is k_bT. On the other hand, the PL from atomic systems is quite narrow, obeying the uncertainty principle ($\Delta E \Delta t \geq \frac{\hbar}{2}$). These differences occur because in atomic systems the states are discrete, whether in solids they form a continuum named the band structure.

Although atomic emissions emerge in ensembles of atoms that do not interact so strongly as in solids, there are interesting solid systems that can behave as atomic. We can cite two of them, the defect centres in crystals [106–108] and quantum dots [109, 110]. In the first case, point defects in solids generate flat, discrete states inside the gap of the solid, which resemble atomic levels. On the other hand, the quantum confinement generates the atomic-like states in quantum dots. The defect centres in solids can better describe our results in chapter 8, so now we are going to focus on this system. There are some distinctions between the atomic-like and crystal emissions. One of them is the narrow FWHM of atomic-like emissions discussed previously. In addition, the defect centres generate mid-gap states in the solid, so we can probe them by measuring PL with subgap excitation ($E_{\mathrm{L}} < E_{\mathrm{g}}$). Recall that in solids, we observe PL with $E_{\mathrm{L}} > E_{\mathrm{g}}$, see Fig. 6.5(b). Another measurement that can distinguish between the atomic-like and solid emissions is the dependence of the excitation laser intensity of the PL. Conventionally, atomic-like levels have a limited density of states, so in this case, the PL intensity follows a sublinear curve with the excitation intensity, tending to saturate [106, 107, 109]. On the other hand, the band structure of solids have a high density of states, so the intensity dependence of the photoluminescence is linear [111]. Conclusively, the discussion of this section is fundamental to interpret the atomic-like emission measurements in talc, see section 8.1.

6.3 Photoluminescence under non-trivial electrostatic conditions

Interesting phenomena show up when we apply an electric field in materials and atoms. Here, we study some effects that raise upon transverse electric field applications. More specifically, we consider some of the mechanisms related to the splitting and quenching of the photoluminescence, which are observed in our experiments. We start by describing the Stark effect, that can elucidate the energy shift of atomic-like states.

6.3.1 Stark effect

When we subject atoms or atomic-like systems to an electric field, we can sometimes observe splitting of the energies of the atomic levels. So, we call this phenomenon of Stark effect. Under the electric field influence, the Hamiltonian of the system is given by:

$$H = H_0 - \overrightarrow{E} \cdot \overrightarrow{P}, \tag{6.4}$$

where H_0 is the Hamiltonian of the system in the absence of the electric field, $\overrightarrow{E}$ is the external electric field operator and $\overrightarrow{P}$ is the dipole moment operator. In our experiments, we apply a transverse electric field electric field (parallel to the z direction), then the term $\overrightarrow{E} \cdot \overrightarrow{P}$ becomes simply EP_z. For weak electric fields, we can use the perturbation theory of

the quantum mechanics [112] to expand the energies of the levels as a function of electric field:

$$\varepsilon = \varepsilon_0 - p \cdot E - \frac{1}{2}\alpha \cdot E^2 + \dots, \tag{6.5}$$

where ε_0 is the unperturbed energy, and p and α are coefficients of the linear and quadratic terms of the electric field, respectively. The displacement of the PL from our samples with the electric field are linear, so here we explore only the linear part of the Stark effect. Thus, the quadratic and higher order terms are beyond the scope of this work. Considering only the linear Stark effect, we have:

$$\varepsilon = \varepsilon_0 - p \cdot E. \tag{6.6}$$

For the linear term, if the states are non-degenerate, we have:

$$p = q\langle\phi_0|Z|\phi_0\rangle, \tag{6.7}$$

where we use the formula $P_z = qZ$ (Z is the projection of the position operator in the z direction) and ϕ_0 is an eigenstate of the unperturbed Hamiltonian. The coefficient p is the expected mean value of the operator electric dipole moment. Using the SI system, the unit of the electric dipole is C.m, but the most used unit is the Debye (D), where $1\,\mathrm{D} = 3.33564 \times 10^{-30}\,\mathrm{C \cdot m}$. From equation 6.6, the operator Z has odd parity, so if the eigenstate $|\phi_0\rangle$ has a well-defined parity, which occurs for some atomic states, the equation 6.6 is zero. Thus, a non-degenerate state displays linear stark shift if it does not possess parity, which sometimes characterizes non-centrosymmetric states. Besides, the expected mean value of the dipole moment, evaluated in non-degenerate eigenstates that display linear Stark effect, are necessarily non-zero, see equation 6.7. Nevertheless, degenerate states with well-defined parity may also present linear stark shift. In this case, the electric field lifts the degeneracy of these states.

Note that according to equation 6.6, for $E > 0$ the stark effect shifts the energies of the system toward lower values (redshift) if $p > 0$. On the other hand, we can observe shifts of the energies toward higher values (blueshift) for $p < 0$. For the case of $E < 0$, we observe a redshift if $p < 0$ and a blueshift if $p > 0$. In a linear Stark effect experiment, we can fit the energy vs electric field curve with equation 6.6 to extract the dipole moment of the system.

Recall that talc is a dielectric material. So, the applied electric field inside talc (internal field) is different than the external electric field. The internal field is given by $E_{\text{int}} = E_{\text{ext}} + \frac{1}{3\epsilon_0}P$ [113], where E_{int} and E_{ext} are the internal and external electric fields, respectively. Assuming that talc is a linear dielectric, we have $P = \epsilon_0 \chi_e E_{\text{ext}}$. So, we can obtain:

$$E_{\text{int}} = \left(\frac{2 + \epsilon_r}{3}\right) E_{\text{ext}}, \tag{6.8}$$

where $\epsilon_r = 1 + \chi_e$ is the dielectric constant. This expression is frequently called the Lorentz local field approximation [114, 115].

6.3.2 Photoluminescence quenching

Now, we briefly describe some of the mechanisms that can quench the photoluminescence upon electric field applications. We observe a PL quenching in talc, see subsection 8.2.2, so the following discussion is essential to illuminate the interpretation of our results. Some of the mechanisms that explain a PL quenching via electric field applications are (I) thermal dissociation, (II) ionization via electric field, (III) field-induced enhancement of the non-radiative portion of exciton recombination, (IV) change in radiative lifetime, and (V) impact ionization by field accelerated electrons [116]. Below, we provide a brief discussion of each of these effects.

For the (I) thermal dissociation process, the thermal energy is not enough to break the excitons of a semiconductor or to ionize atomic levels in an atom. However, the electric field application lowers the energy barriers that prevent the separation of the charges. In this process, the field lowering may be enough to yield the thermal dissociation. The electric field does not quench the PL by itself. It only helps the thermal energy to separate the carriers. The thermal dissociation of the carriers prevents their recombination, quenching the photoluminescence.

The (II) ionization via electric field occurs when we use ultra-high electric fields ($E \sim 1 - 100\,\mathrm{MV/m}$, see the reference [117–119]). In this scenario, the electric field can ionize a defect center in a semiconductor/insulator to its valence or conduction bands [117], or can also break excitons in quantum dots [116, 118]. The quenching effect of the mechanism II is reversible [117, 118]. Note that the electric field by itself separates the carriers in the mechanism II, quenching the PL during the process.

The (III) field-induced enhancement of the non-radiative portion of exciton recombination can decrease the photoluminescence because the non-radiative channels compete with the radiative, reducing the PL efficiency as pointed in equation 6.2.

The (IV) change in radiative lifetime induced by electric field may also quench the PL, because an increase of the radiative lifetime reduces the spontaneous emission rate, see equation 6.1.

Finally, the (V) impact ionization by field accelerated electrons occurs when the electric field accelerates free carriers (they can also be photoexcited excess carriers), which collides with the excitons, breaking them. The exciton breaking prevents their recombination, leading to a PL quenching. This effect typically occurs in semiconductors, where the excitonic states are close to the conducting states. Generally, we need a low electric field to quench the photoluminescence by this mechanism ($E \sim 1 - 10\,\mathrm{mV/m}$), see the reference [116, 120].

The Stark splitting and PL quenching are fascinating and rich physical phenomena. Furthermore, they have large applications, including electro-optic modulators and integrating optoelectronics. Few works are exploiting the linear stark effect in solids, especially the 2D materials. There are even fewer papers on the PL quenching topic. In this thesis, we explore these two interesting effects simultaneously in a new 2D material (2D talc). In this direction, we believe that our work illuminates the aspects of the atomic-like emission in solids and uncovers interesting phenomena in 2D materials. Now that we have discussed the critical theoretical points of our work, we describe in the next chapter the methods used in this

project, and very soon, in chapter 8, we expose and elaborate our experimental results.

Chapter 7

Methods and characterizations

In this chapter, we describe the methods and characterizations used in part II of the thesis. We start with the preparation of our talc device. Next, we consider the experimental techniques that we use to characterize the talc crystal, which are the X-ray diffraction, the Raman spectroscopy and the wavelength-dispersive X-ray spectroscopy (WDS). Finally, we present the photoluminescence setup that we use for the measurements of chapter 8.

7.1 Sample preparation

For the part I of this thesis, we study a single device, which is a Van der Waals heterostructure consisting of few-layer graphene on top of a 116 nm thick talc flake. In this case, we use a graphite crystal to provide a flat back gate electrode. We require few-layer graphene as an electrode because it is a quasi-transparent material. On the other hand, a flat back gate electrode is needed to apply an electric field uniformly. To make this structure, we use the pick-up method [121]. Now, instead of transferring flakes from the membrane to the substrate, we initially do the opposite: we pick-up the flakes from the substrate with the membrane. To pick-up the flakes, we approach a polycarbonate (PC) membrane to the substrate at $T = 70\,^{\circ}\mathrm{C}$ but without touching the flakes. Then, we warm-up the system up to $T = 83\,^{\circ}\mathrm{C}$ for two minutes. After we increase the temperature of the system, the PC expands, touching the flake in this process, because PC is a thermoplastic material. So, we turn the heater off and wait for the system to cool down, picking-up the flake. To transfer the flakes to a substrate, we keep the membrane in the desired substrate and warm-up the system to $T = 160\,^{\circ}\mathrm{C}$. To remove the PC residue, we put the substrate on a chloroform bath for ten minutes at $T = 40\,^{\circ}\mathrm{C}$ and rinse in IPA followed by blow-dry in Argon. The membrane that we use for the pick-up method is composed of PC on top of PDMS. The PC is from

Sigma Aldrich and is 6% dissolved in chloroform. Fig. 7.1 presents how we prepare the talc devices by the pick-up method. First, we exfoliate graphite crystals on a Si/SiO_2 substrate by standard micromechanical cleavage. Then, we select few-layer graphene flakes and also thin graphite crystals (20 nm thick). Next, we exfoliate talc on a different Si/SiO_2 substrate. Afterward, we pick-up the few-layer graphene flake, Fig. 7.1(a). Then, we pick-up the talc, but ensuring that the graphene flake is on top of the talc flake. Finally, we transfer these flakes to a graphite flake, again ensuring that the flakes are aligned and that the graphene does not touch the graphite, avoiding electrical contact between them.

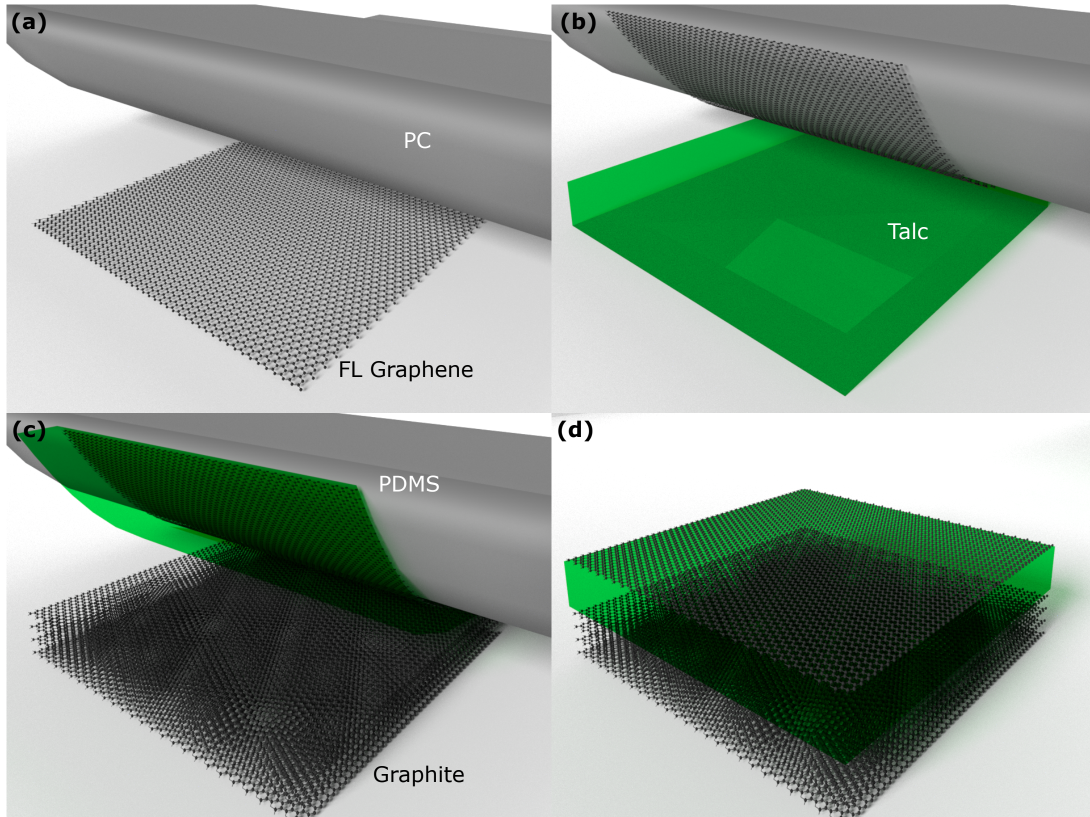

Figure 7.1: **Preparing the talc device**.

After we prepare the Van der Waals heterostructure of talc, we contact the graphite and the few-layer graphene electrically by e-beam lithography and thermal evaporation of a stitching layer of Cr (1 nm) followed by Au (90 nm). Fig. 7.2 shows an optical image of the talc device, where we can see the graphite, talc, and few-layer graphene flakes. We have two graphene flakes that are electrically contacted independently. So, we can apply different potentials in these flakes.

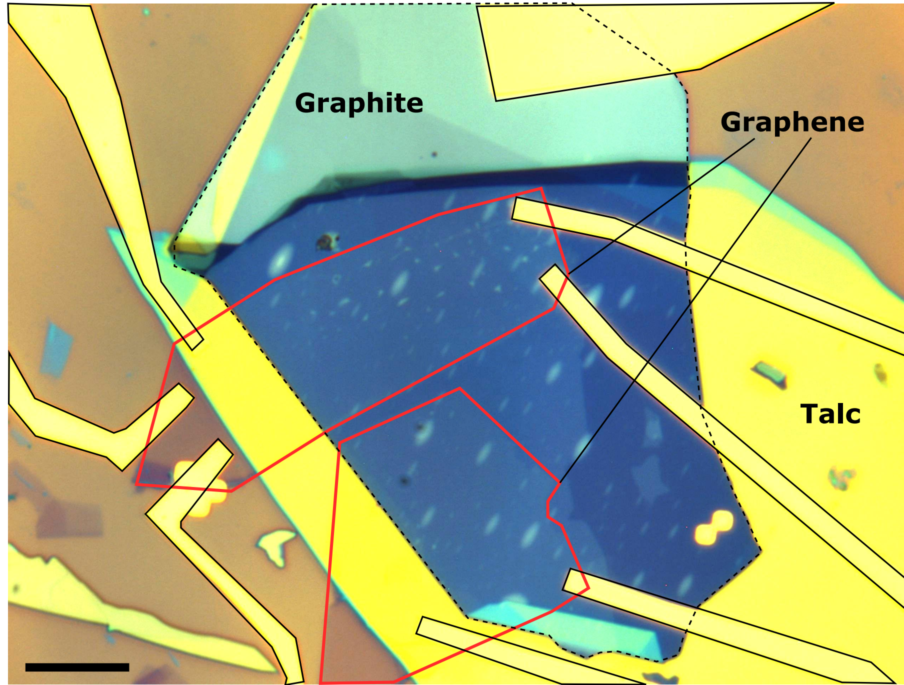

Figure 7.2: **Optical image of the talc device**. Scale bar is 10 μm.

7.2 X-ray diffraction

In this work, we obtain the talc samples from a talc (soapstone) mineral crystal from Ouro Preto (Brazil), see Fig. 7.3(a). X-ray diffraction (XRD) measurements were carried out at the XRD1 beamline of the Brazilian Synchrotron Light Laboratory (LNLS) to corroborate $Mg_3Si_4O_{10}(OH)_2$ as the major phase of the mineral crystal, see Fig. 7.3(b). We can access these measurements in the reference [94], and we repeat them here with proper permission of the authors. Here, we use the same mineral crystal of this group. The main phase observed is the triclinic P1 system (Rietveld refinement using ICSD 100682), with lattice structure given by a = 5.291(1) Å, b = 9.172(1) Å, c = 9.455(1) Å, $\alpha = 90.58(1)^\circ$, $\beta = 98.77(1)^\circ$, $\gamma = 89.99(1)^\circ$. This crystallographic structure that we show in Fig. 7.3(c) was used to produce the fit of Fig. 7.3(b) (Rietveld refinement using the MAUD software), which is the best possible fit using a single talc phase. It is possible to simulate the other structures from crystallographic databases but leads to poor or incomplete fits of the experimental data.

7.3 Raman spectroscopy

We discussed in section 3.2 that the Raman spectroscopy provides information of the vibrational properties of materials. In this way, the peaks in the Raman spectrum are assigned to vibrational modes. So, it is possible to use Raman spectroscopy to characterize materials. However, few reports are describing and interpreting the Raman spectrum of talc [122, 123]. We present in Fig. 7.4 the Raman spectrum of our talc crystal. The spectrum is very similar to data from the literature [122, 123]. Talc has a rich Raman spectrum, because of the large

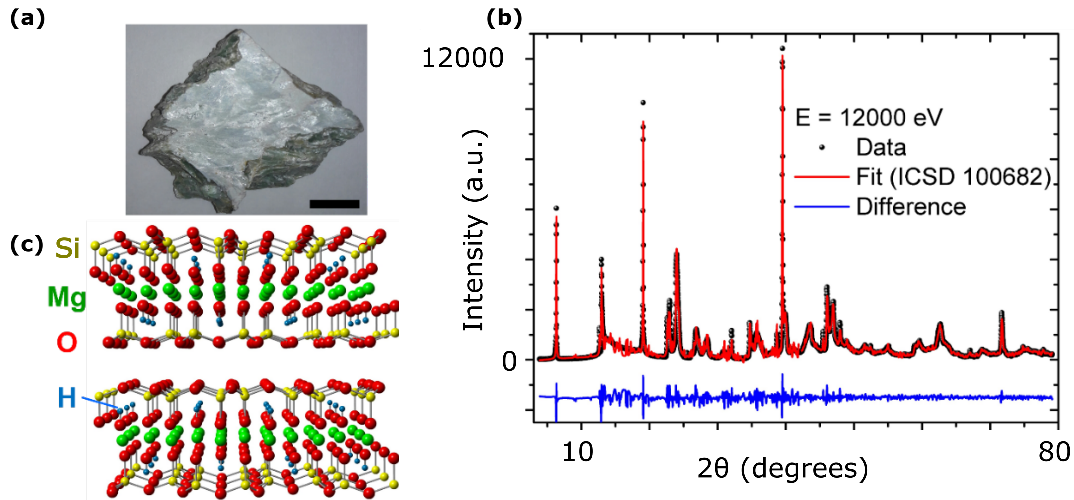

Figure 7.3: **X-ray characterization of talc**. **(a)**, optical image of a talc/soapstone crystal, scale bar is 2.5 cm. **(b)**, X-ray measurement of the talc crystal. **(c)**, representation of the triclinic crystalline structure of talc (ICSD 100682), used to fit the diffraction data of **(b)**. Data taken with permission from [94].

number of atoms and of its complex structure. The Raman spectrum shows three prominent peaks at 369 cm^{-1}, 684 cm^{-1} and 3684 cm^{-1} among others with smaller intensities.

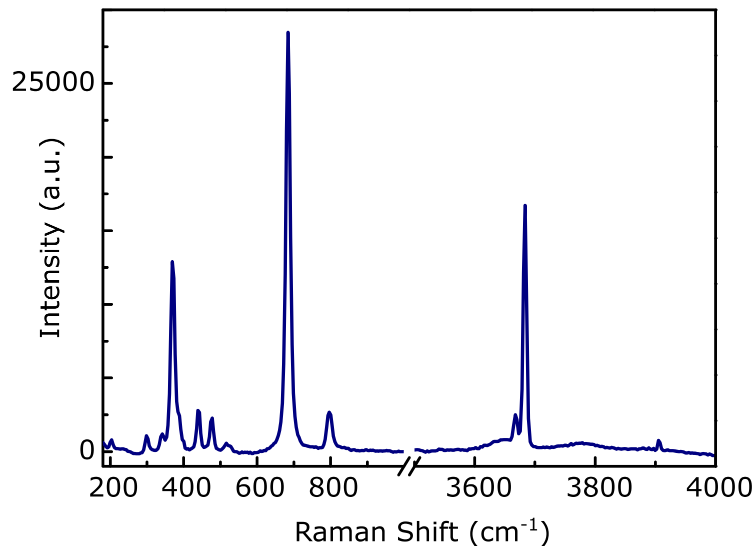

Figure 7.4: **Raman spectrum of talc**. We use a $\lambda = 457\,\text{nm}$, fluence of 12 $mW/\mu m^2$ and 600 g/mm grating.

Table 7.1 shows the position of the Raman peaks of Fig. 7.4. The most intense peaks are highlighted in bold. Table 7.1 also shows the intensity of the peaks on a scale of weak (w), medium (m), strong (s) and very strong (vs). The strong peak with a frequency of 3684 cm^{-1} is attributed to the stretch of the hydroxyl group (OH^-). The medium peak of 440 cm^{-1}, in turn, corresponds to the in-plane asymmetric stretch of the bridging oxygen

(Si-O-Si), while the 475 cm^{-1} may be due to the out-of-plane stretch of the "brucite" layer (Mg_3OH_2) [123, 124]. For more detailed group analyses of talc vibrational modes, see the reference [123, 124].

Table 7.1: **Raman peaks of talc**. Position of the Raman peaks of talc and their intensity. The abbreviations w, m, s and vs of the intensity correspond to weak, medium, strong and very strong, respectively. The most intense peaks are highlighted in bold.

Raman shift (cm^{-1})	Raman intensity (a.u.)
204	w
298	w
342	w
369	s
388	w
440	m
475	m
516	w
528	w
684	vs
797	m
3667	m
3684	s

7.4 Wavelength-dispersive X-ray spectroscopy

The soapstone is a rock with several components, been talc one of them. We show in Fig. 7.3 that the main phase of our soapstone crystal is talc. However, the literature reports lots of impurities in talc crystals, mainly Fe and Al, but also traces of Ni, Cu, Mn, and others [96–99], that cannot be measured by standard X-ray spectroscopy. As we study PL from defect states in talc, it is so important to identify the impurities on its structure. For this purpose, we did wavelength-dispersive X-ray spectroscopy (WDS) measurements at the Center of Microscopy at the Federal University of Minas Gerais (Brazil). WDS is a technique that can provide information regarding the chemical species of the materials and their concentrations. WDS uses an electron beam with high energies (typically 20 KV) that interacts with the sample. From this interaction, the sample emits X-rays with specific energies for each element. Thus, from the X-ray spectra that the sample emits, we can identify the elements of the material. Furthermore, the setup of the WDS contains a crystal and detector that are mobile. The X-ray from the sample goes through Bragg diffractions in the crystal. By employing precise spatial configurations of the crystal and detector, the Bragg diffractions select specific X-rays with proper energy. In this way, we can measure a particular signal from the sample at each time, which increases the precision and the detectability of the chemical species. From the WDS measurements, we can identify the impurities of Fe and Ni in our talc crystal. Yet, WDS can detect only elements with concentrations in weight percentage larger than 0.1%. Hence, our talc crystal can possess more impurities rather than Fe and Ni, but with a lower concentration. Table 7.2 shows the concentration in weight percentage of the SiO_2, MgO, FeO, and NiO elements. We did thirteen measurements in different locations in the talc crystal, and surprisingly the concentrations do not vary significantly. From the values of the table, we can estimate the concentrations of Fe and Ni, which are 1.32 ± 0.04 % and 0.32 ± 0.02 %, respectively.

Table 7.2: **Weight concentrations of talc chemical species**. Weight concentrations of the SiO_2, MgO, FeO and NiO elements.

N.	SiO_2 (%)	MgO (%)	FeO (%)	NiO (%)
1	61.85	29.18	1.30	0.29
2	64.22	30.75	1.42	0.30
3	61.33	30.56	1.34	0.31
4	64.70	28.91	1.28	0.33
5	57.87	26.74	1.30	0.36
6	59.23	28.65	1.28	0.35
7	64.76	30.93	1.29	0.31
8	62.63	29.59	1.36	0.32
9	61.20	31.51	1.27	0.31
10	62.58	28.85	1.32	0.31
11	60.34	29.20	1.34	0.34
12	62.66	32.04	1.31	0.35
13	61.10	35.03	1.30	0.29

7.5 Photoluminescence setup

Now, we describe the photoluminescence setup that we use for the measurements of chapter 8. Fig. 7.5 shows the photoluminescence setup. To do the PL measurements, we use both Witec and T64000 systems. We mainly use two lasers, a He/Cd laser with $\lambda = 441\,\text{nm}$ and a solid state laser with $\lambda = 457\,\text{nm}$. After the laser, there is a Senrock laserline filter for the T64000 setup. Next, the laser crosses a beam splitter, which reflects and transmits 50 % of the light. The reflected light enters the microscope and is focused on the device by a 50× magnification lens (spot size of ≈1 μm). The generated PL signal goes back to the microscope and is transmitted by the beam splitter. For the Witec setup, the transmitted PL passes through an edge filter. In this way, we can filter the laser signal from the PL signal. In both Witec and T64000 setups, the PL beam enters a spectrometer and a CCD. For the T64000, we use the spectrometer in a triple subtractive mode, with a 1800 g/mm grating. For the Witec, we use the single mode, with a 600 g/mm grating.

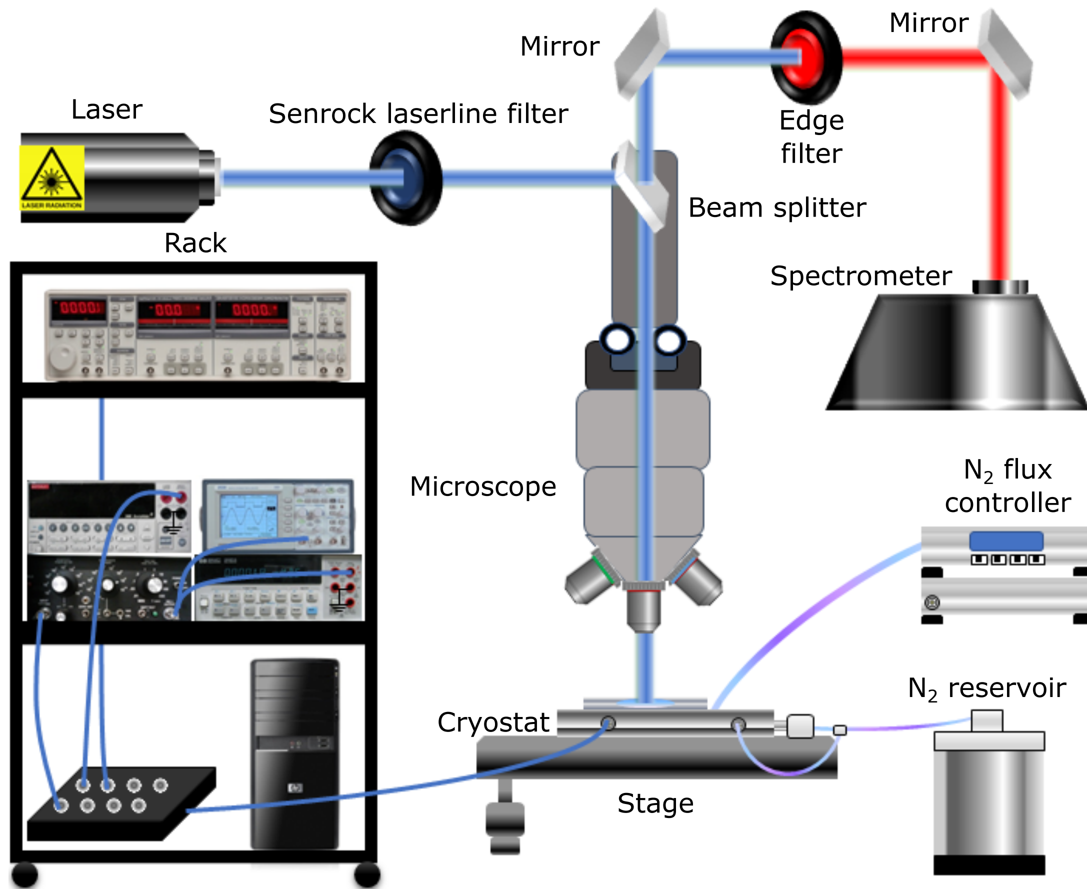

Figure 7.5: **Photoluminescence setup**. The credit for the microscope cartoon is to Natalia Rezende.

Our device is inside a Linkam cryostat during the measurements. Thus, during our measurements, the temperature of the device is $T = 80\,\text{K}$. The Linkam cryostat is coupled with the microscope stage, and there is a N_2 reservoir that provides liquid N_2 to the cryostat. N_2 flux and temperature controllers are also connected to the cryostat, which ensures thermal

stabilization. The cryostat also has electronic terminals, which are connected to the device and Rack. The Rack, in turn, has the electrical components that we need for doing the measurements. Finally, to apply an electric field in talc, we connect a DC voltage source (Keithley 2400) on graphite, and we ground the few-layer graphene.

Chapter 8

Results and discussion

In this chapter, we describe and discuss our results from the second part of this thesis. We study the electric-control of the atomic-like emissions from 2D talc. So, we characterize these emissions at the beginning of this chapter. Then, we apply an electric field in talc and show how the photoluminescence peaks modify under the field influence. The electric field affects the photoluminescence in two different ways: by Stark splitting and photoluminescence quenching. Thus, we analyze the Stark splitting first, followed by the PL quenching. After presenting our measurements, we deliberate on the possible mechanisms and effects that describe better our results.

8.1 Atomic-like emission in talc

To study the atomic-like emission in talc, we perform photoluminescence spectroscopy measurements with subgap excitation. In other words, we excite talc with laser energy smaller than the band gap energy of talc. Fig. 8.1(a) shows a PL spectrum of talc at low temperature (T= 80 K) using a $E_{\mathrm{L}} = 2.8\,\mathrm{eV}$ laser. Note that $E_{\mathrm{L}} < E_{\mathrm{g}}$, since the band gap energy of talc is 5 eV (see Fig. 6.3), so we are exciting subgap defect states in this material. In a moment we show measurements demonstrating that the optical spectrum in Fig. 8.1(a) is a PL, but from now let us discuss the features of this spectrum. In Fig. 8.1(a), we observe four main peaks with approximate energy of 1.8 eV, denoted by P1', P1", P2' and P2", among others. These peaks are narrow, so we need to use a high-resolution spectrometer to visualize them (in this case, we use a spectrometer with a triple subtractive mode, 1800 g/mm grating, with a 40 μeV resolution). We use this spectrometer mode for all the measurements presented in this section. Since we measure a PL in talc by exciting it with subgap energy, defect states may originate this PL. To better illustrate this hypothesis, Fig. 8.1(b) shows an energy band diagram of an insulator, but with mid-gap defect states. When we excite this system with

subgap energy photons, we excite electrons from the filled states (E_1) to the state E_v, which can be real or virtual. Next, the electrons decay to the empty states E_2 and decay back to the states E_1 emitting photons with subgap energy.

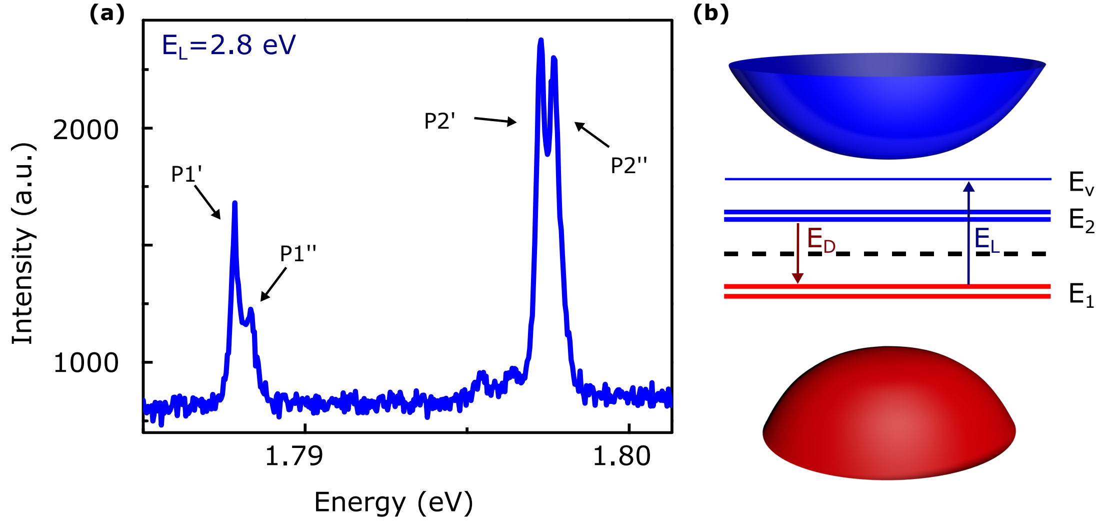

Figure 8.1: **PL emission from defect states**. **(a)**, PL emission from defect states in talc, $E_L = 2.8\,\mathrm{eV}$, fluence of 12 mW/μm^2, and $T = 80\,\mathrm{K}$. In this measurement, we use a spectrometer with a triple subtractive mode and 1800 g/mm grating. **(b)**, band-diagram of an insulator with mid-gap states.

We need to perform a fitting analysis of the spectrum from Fig. 8.1(a) to obtain relevant parameters, as the energy and full width at half maximum (FWHM) of the peaks. Fig. 8.2 presents a fitting analysis of the PL peaks from Fig. 8.1(a). Here, we use Lorentzians functions to fit the data. Fig. 8.2(a) presents fittings from the P1' and P1" peaks, while Fig. 8.2(b) presents fittings from the P2' and P2" peaks. In Fig. 8.2(b), we fit other peaks rather than P2' and P2", but we do not study them in this thesis. From the fittings, we obtain values of energy and FWHM of the peaks, that are presented in Fig. 8.2(c). The energies of the peaks are in the range 1.78783 eV-1.79768 eV. Also, the values of the FWHM are in the range 27-48 $\times\, 10\,\mu$eV. These small values of FWHM show that the measured PL peaks are narrow, similar to the atomic emissions, where the FWHM is of the order of 40 μeV [125].

To show that the peaks from Fig. 8.1(a) are due to a PL process, we should study the behavior of the PL for different E_L - the energies of PL peaks do not vary when we change the excitation energy. For this purpose, we measure spectra with the excitation wavelengths of 442 nm, 447 nm, 488 nm, and 514 nm, see Fig. 8.3. Fig. 8.3 shows that the peaks have the same energies for all the excitation lasers, see the dashed red line. Accordingly, the results of Fig. 8.3 corroborates that the peaks from Fig. 8.1(a) are due to a PL effect.

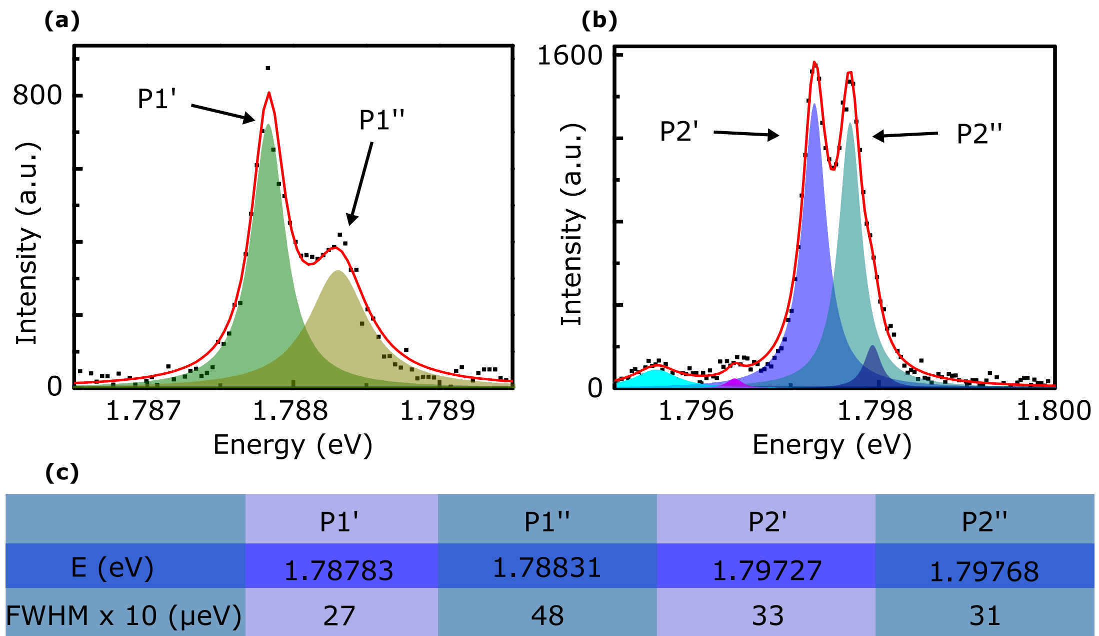

	P1'	P1''	P2'	P2''
E (eV)	1.78783	1.78831	1.79727	1.79768
FWHM x 10 (μeV)	27	48	33	31

Figure 8.2: **Fittings of the PL spectrum**. **(a)**, Lorentzian fittings of the P1' and P1" peaks. **(b)**, Lorentzian fittings of the P2' and P2" peaks. **(c)**, values of energy and FWHM obtained from the fittings.

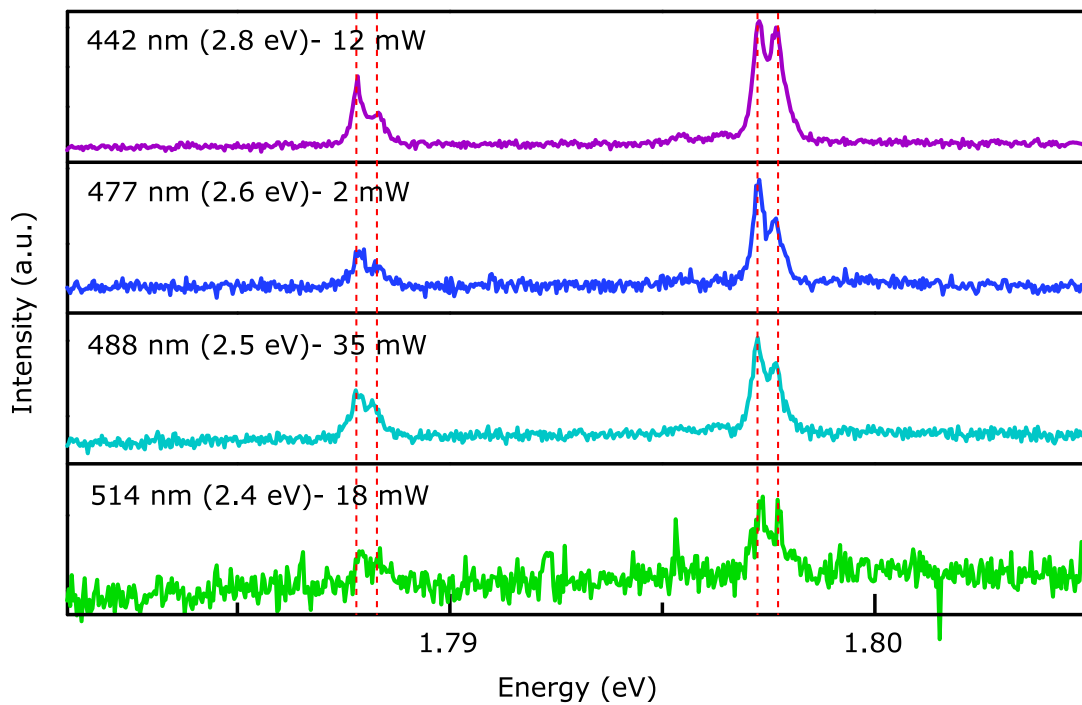

Figure 8.3: **PL spectra with different excitation lasers**. In these measurements $T = 80\,\mathrm{K}$, and we use a triple subtractive mode with 1800 g/mm grating.

It is relevant to provide more evidence that the PL peaks of Fig. 8.1 (a) are from defects. It is known that the PL of defect centres in insulators has a sublinear behavior with the laser power and tends to saturate [106, 107]. This property is due to the limited density of states from the defect states relative to the conducting states of a crystal. With these facts in mind, we measure a power dependence of the PL spectra, see Fig. 8.4. The symbols represent the intensity of the PL peaks for each laser power. To confirm that the power dependence of the PL is sublinear, we fit the data of Fig. 8.4 with the equation $y = ax^{\alpha}$. In this equation, a is the multiplier coefficient, and α is the exponent coefficient. The PL data has a sublinear response if we obtain $\alpha < 1$ after fitting it. The lines in Fig. 8.4 are fittings from the equation $y = ax^{\alpha}$. From the fittings, we obtain the values of α for each peak. For the peaks P1', P1", P2' and P2" we have $\alpha = 0.76$, 0.72, 0.84 and 0.81, respectively. For all peaks $\alpha < 1$, which characterize a sublinear response. A sublinear response is another evidence for the excitation of defects, as we desired.

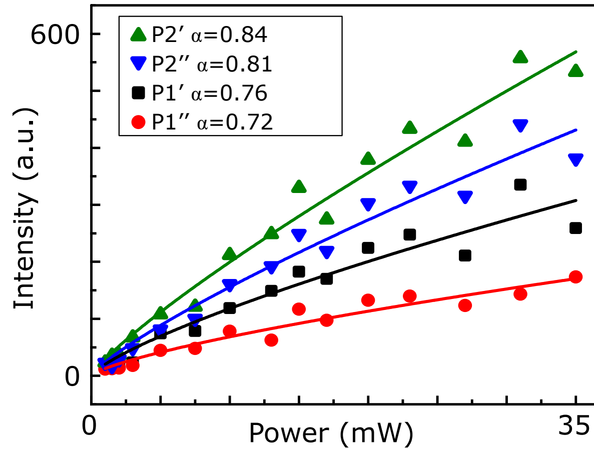

Figure 8.4: **Power dependence of the PL spectra**. For these measurements we use the 2.8 eV (442 nm) laser, T= 80 K, and a triple subtractive mode with 1800 g/mm grating.

So far, we presented the basic characterization of the narrow PL peaks, which shows up when we excite talc with subgap excitation. We argued that these peaks are actually from a photoluminescence effect and that they follow a sublinear behavior with the laser power. This last result, combined with the fact that we observe the PL peaks with subgap excitation, points to the existence of mid-gap defect states. Moreover, the emissions are atomic-like. According to our WDS measurements, see table 7.2, the predominant impurity in our talc crystal is Fe. Toward this direction, Alencar, A. did some DFT calculus to predict the modification of the talc electronic structure due to the replacement of Fe impurities in the atoms of talc, see the reference [95]. There are three different possible configurations of Fe replacing atoms in talc, see Fig. 8.5: Fe replacing Mg in the site 1, see Fig. 8.5(a), Fe replacing Mg in the site 2, see Fig. 8.5(b), and Fe replacing Si, see Fig. 8.5(c). In Fig. 8.5, the region highlighted in blue and delimited by the dashed blue line correspond to mid-gap states generated by the Fe impurity, the dashed black line is the Fermi level, and the red and black lines correspond to states with opposite spins. Observe the images on top of Fig.

8.5, that represent the possible configurations of Fe replacing Mg and Si.

Note that the Fe impurities generate flat states that are similar to atomic levels. The small dispersion observed for the defect states in Fig 8.5 originates from the periodic unit cells of the DFT calculation. Additionally, the Fe atom has electronic configuration of [Ar]$3d^6 4s^2$, so it has eight electrons in the valence orbitals. Interestingly, the Fe impurities in talc give rise to exact eight states with well-defined spins, see Fig. 8.5. Perceive that, in Fig. 8.5(a), the red curve right above the Fermi level has two states. It is possible to occur, in the diagram of Fig. 8.5, radiative transitions between defect states that are above and below the Fermi level. Our PL peaks have energies close to 2 eV, so in Fig. 8.5 we also point with arrows the transitions that have similar energy difference. Thus, the transitions of the levels marked with arrows may explain the results of Fig. 8.1(a) qualitatively. Otherwise stated, the DFT calculus reinforces that the Fe impurities in talc can give rise to atomic-like emission as we observe in Fig. 8.1. Each of the configurations in Fig. 8.5 can explain our results, so we are working on XPS measurements to confirm which of these configurations is more likely to occur in our talc crystal. Nonetheless, in subsection 8.2.1 we show strong evidence that points toward Fe replacing Si atoms as the configuration that better describes the emissions of talc.

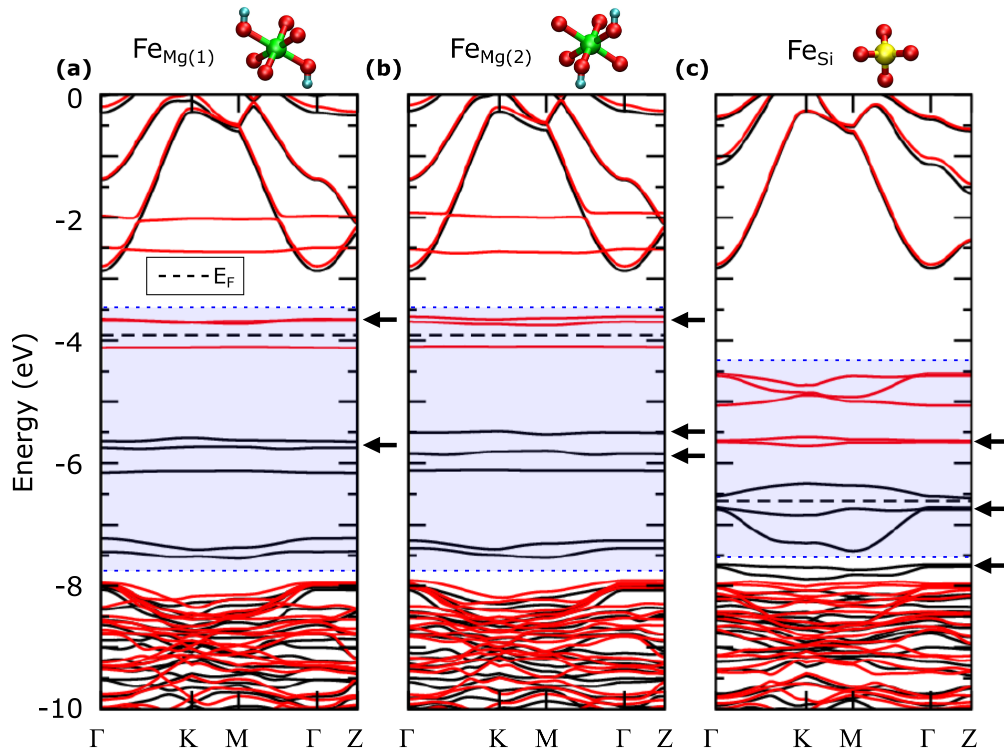

Figure 8.5: **Electronic structure of talc with Fe impurities.** In **(a)**, Fe replacing Mg in the site 1. **(b)**, Fe replacing Mg in the site 2. **(c)**, Fe replacing Si. Taken from [95].

8.2 Effects of electric field applications in the photoluminescence of talc

We have studied optical properties of talc, the atomic-like emissions. Now, we apply a perpendicular electric field in this material to unravel optoelectronic effects, using the device depicted in Fig. 7.2. Here, we tune the energy and the intensity of the PL peaks. These measurements are time-consuming, so to speed up the process, we use a 600 g/mm grating, which provides a better signal. This grating has a low resolution (260 μeV) compared to the 1800 g/mm grating (40 μeV), so we observe the P1' and P1" peaks as a single peak when we do not apply a gate-potential. The same is observed for the P2' and P2" peaks, see the red spectrum in Fig. 8.6. To clarify the modifications of the PL spectra under electric field applications, we measure PL spectra for several gate voltages and plot these results in a 2D waterfall graph. Fig. 8.6 shows a 2D waterfall graph from PL spectra with $V_{\mathrm{BG}} = 0\,\mathrm{V}$, $-35\,\mathrm{V}$, $-56\,\mathrm{V}$, and $-98\,\mathrm{V}$. For $V_{\mathrm{BG}} = 0\,\mathrm{V}$ we observe mainly two peaks, P1 and P2, because we use a low-resolution grating, so we do not distinguish the fine structure of Fig. 8.1(a). When we apply $V_{\mathrm{BG}} = -35\,\mathrm{V}$, we detect the fine structure of the peaks because P1' and P1" split further away from each other. Observe that the same occurs for the P2' and P2" peaks.

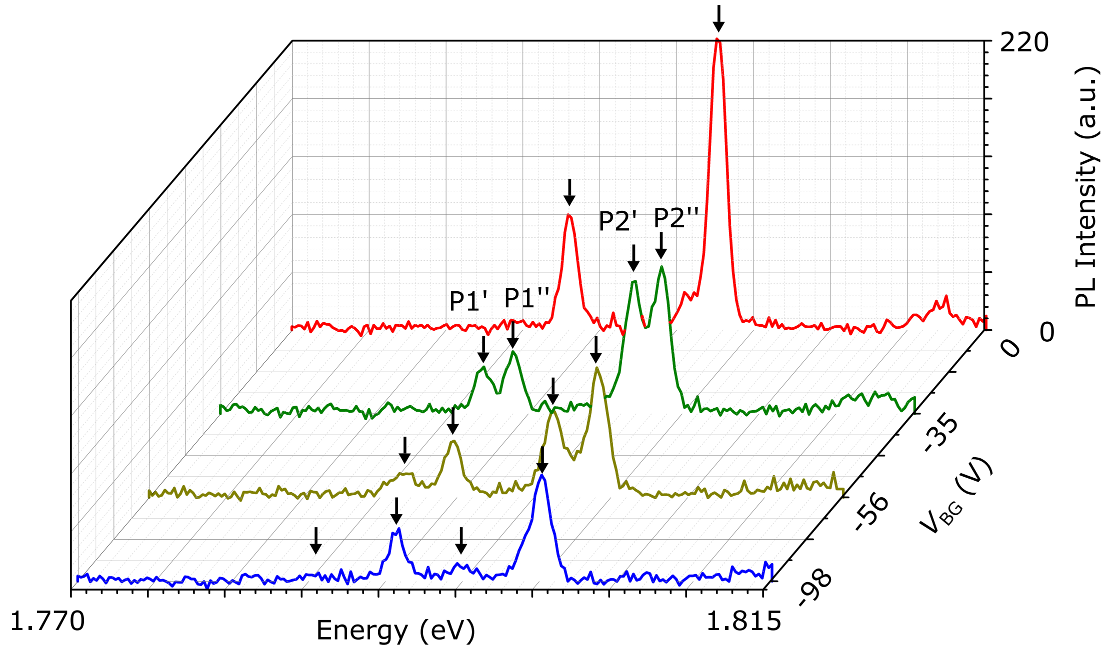

Figure 8.6: **PL spectra for different V_{BG}.** For these measurements we use the 2.7 eV (457 nm) laser, $T = 80\,\mathrm{K}$ and fluence of 12 mW/μm^2. We use a spectrometer in the single mode with 600 g/mm grating.

Besides, we observe a partial quenching of the peaks. This quenching is more evident when we apply $V_{\mathrm{BG}} = -56\,\mathrm{V}$, because there is a strong reduction of the PL intensity in this configuration. Furthermore, the peaks displace even further by applying larger electric

fields. Finally, we quench the P1' and P2' peaks almost completely by applying $V_{\mathrm{BG}} = -98$.

To better describe the gate-tunability of the PL peaks, Fig. 8.7 presents a colormap of the normalized PL intensity as a function of V_{BG} and energy. In Fig. 8.7, we also plot the PL for $V_{\mathrm{BG}} > 0\,\mathrm{V}$. We observe a linear shift of the energies of the PL peaks by increasing the electric field. For $V_{\mathrm{BG}} < 0\,\mathrm{V}$, the P1' and P2' peaks suffer a redshift, while the P1" and P2" peaks suffer a blueshift. On the other hand, for $V_{\mathrm{BG}} > 0\,\mathrm{V}$ the P1' and P2' peaks suffer a blueshift, while the P1" and P2" peaks suffer a redshift.

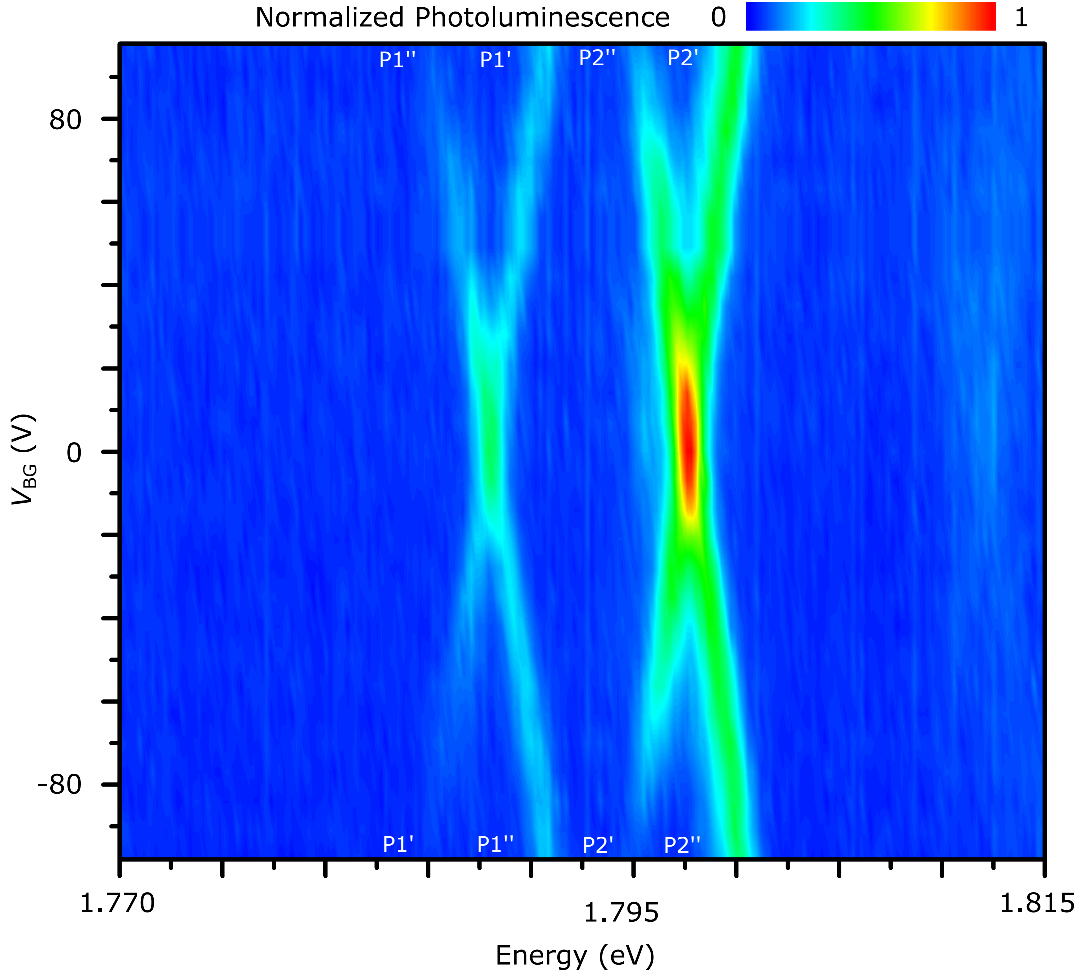

Figure 8.7: **Colormap of the normalized PL intensity as a function of V_{BG} and energy**. For these measurements we use the 2.7 eV (457 nm) laser, T= 80 K and fluence of 12 mW/μm^2. We use a spectrometer in the single mode with 600 g/mm grating.

Furthermore, the electric field starts to quench the PL intensity from $V_{\mathrm{BG}} \approx |40|\,\mathrm{V}$. For example, for the P1' peak, the color goes from green, for $V_{\mathrm{BG}} = 0\,\mathrm{V}$, to blue, for $V_{\mathrm{BG}} = -98\,\mathrm{V}$. The blue color corresponds to the intensity 0, and the red color corresponds to the intensity 1. Similarly, the color of the P2' peak goes from red to blue. In the $V_{\mathrm{BG}} < 0\,\mathrm{V}$ regime, the PL of the P1' and P2' peaks quenches almost completely for large electric fields, as the color that corresponds to the peaks in this condition is similar to the color of the substrate. However, we do not quench the P1" and P2" peaks completely in the $V_{\mathrm{BG}} < 0\,\mathrm{V}$ regime, because for $V_{\mathrm{BG}} < 40\,\mathrm{V}$ these peaks have approximately a constant intensity. On

the other hand, the application of large electric fields in the $V_{BG} > 0\,V$ regime quench the P1" and P2" peaks instead of the P1' and P2' peaks.

The application of a perpendicular electric field in talc modifies the PL peaks in two manners. So, we are going to study these modifications separately, starting with the shifting of the peaks, which are due to a linear Stark effect.

8.2.1 Linear Stark splitting of the photoluminescence peaks

Now, we draw our attention to the splitting of the photoluminescence peaks. Although the colormap in Fig. 8.7 provides a beautiful picture of our results, it is not the better representation to describe the PL shift. For this purpose, we should plot the energy of the peaks as a function of the internal electric field. We evaluate the internal electric field by the equation 6.8. Here, we assume that the dielectric constant of talc is 2.5 [105], and its thickness is 116 nm, measured by atomic force microscopy. Fig. 8.8(a) presents a PL energy as a function of the internal electric field curve for the P1', P1", P2' and P2" peaks. To obtain the plot of Fig. 8.8(a), we fit the data from Fig. 8.7 with Lorentzians, considering only the $V_{\mathrm{BG}} < 0\,\mathrm{V}$ region. From the fittings, we extract the energies of the peaks, and plot them as a function of the internal electric field, see Fig. 8.8(a). The PL energies are linear functions of the electric field, which points for a linear stark effect, see section 6.3. In this way, we use the equation 6.6 to fit the data from Fig. 8.8(a) and extract the dipole moment of the emissions. The lines in Fig. 8.8(a) are the fittings, and in Fig. 8.8(b) we show the dipole moments extracted from the fittings. The dipole moments are represented in units of D ($1\,\mathrm{D} = 3.33564 \times 10^{-30}\,\mathrm{C} \cdot \mathrm{m}$). For the P2", P2', P1" and P1' peaks, we obtain dipole moments of 0.093±0.003 D, −0.090±0.003 D, 0.105±0.003 D and −0.098±0.004 D, respectively.

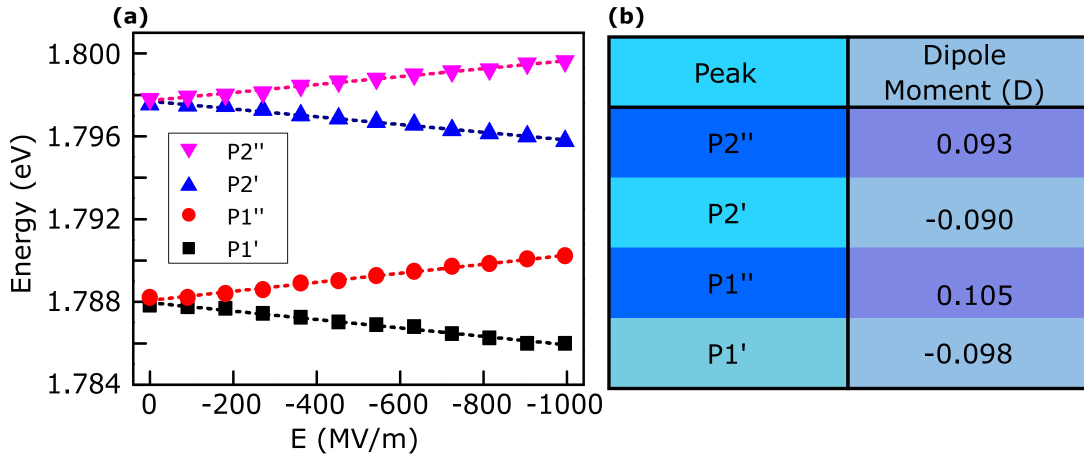

Peak	Dipole Moment (D)
P2''	0.093
P2'	-0.090
P1''	0.105
P1'	-0.098

Figure 8.8: **PL energy as a function of the electric field**. For the measurements of **(a)** we use the 2.7 eV (457 nm) laser, $T = 80\,\mathrm{K}$ and fluence of 12 mW/μm^2. We use a spectrometer in the single mode with 600 g/mm grating. **(b)**, dipole moments obtained by fitting the data of **(a)**.

To get insight into the results of Fig. 8.8, we should note that first, the PL energy behaves linearly with the electric field, and second, it seems that there is already a small split of the peaks with $V_{\mathrm{BG}} = 0\,\mathrm{V}$, see Fig. 8.1. These results may allude for the existence of an intrinsic electric dipole moment in the surroundings of the defect centres, which could lift the degeneracy of the defect states in the $V_{\mathrm{BG}} = 0\,\mathrm{V}$ condition. We cannot observe this issue in Fig. 8.6 (red curve), because in these measurements we use a low-resolution grating. On the other hand, in Fig. 8.1 we use a high-resolution grading, which allows the observation of the splitting with $V_{\mathrm{BG}} = 0\,\mathrm{V}$.

In section 6.3, we argued that a linear Stark effect occurs if the expected mean value of the dipole moment evaluated in the non-perturbed eigenstate is non-zero. However, if the expected mean value of the dipole moment is zero, there is still a possibility to observe the linear Stark effect. In this case, the states have to be degenerate. As the PL states are non-degenerate, see Fig. 8.1 and Fig. 8.2, it is natural to think that the expected mean value of the dipole moment is non-zero. From these hypotheses, we deduce which configuration in Fig. 8.5 should be appropriate to describe our results. It is not possible to obtain a dipole moment if the Fe atom is replacing the Mg atom in talc. The reason is that in this configuration the Fe atoms are symmetrically positioned in the monolayer talc, because the Mg atoms are located in the middle of the monolayer, see Fig. 6.2(d). In contrast, the Si atoms are positioned in the edges of the monolayer, see Fig. 6.2(d). So, the replacement of Fe atoms in Si sites generates an intrinsic dipole moment. There are two layers of Si atoms in talc, which are symmetrically located on opposite sides of the monolayer talc. Consequently, we expect that they generate dipole moments with opposite orientations along the z-axis. These assumptions match our measurements, that exhibit dipole moments with opposite signals, see Fig. 8.8(b). Thus, from our linear Stark effect results, we strongly believe that Fe impurities are substituting Si atoms in talc, and they generate the atomic-like emissions.

8.2.2 Quenching of the photoluminescence peaks

Now, we describe the quenching of the PL intensity as a function of the transverse electric field. Fig. 8.9(a) displays the absolute PL intensity of the P1', P1", P2' and P2" peaks as a function of the gate voltage. To plot the data of Fig. 8.9(a), we extract the maximum intensities of the Lorentzians fittings of the peaks from Fig. 8.7. Here, we only consider the $V_{\mathrm{BG}} < 0\,\mathrm{V}$ regime. For the P2" peak, the PL intensity varies from 125 to 75. This value remains almost stable at 75 for large electric fields. Similarly, for the P1" peak, the intensity slightly varies from 50 to 40. Differently, the intensity of the P1' and P2' peaks drops to approximately zero for large voltages. In Fig. 8.9(b), we normalize the data of Fig. 8.9(a) by the intensities of the P2" peak. Note that the normalized intensity of the P1" peak is constant, while the intensities of the P1' and P2' peaks drops to zero for large voltages.

We should remark some essential issues of our results from Fig. 8.9. First, we use ultra-large electric fields to quench the PL. An obvious quenching occurs with $V_{\mathrm{BG}} > |40|\,\mathrm{V}$ or $E > |500|\,\mathrm{MV/m}$, which is a strong field. Second, the PL that we measure comes from the radiative recombination of deep mid-gap states. Third, the PL quenching is reversible. We show this last feature in Fig. 8.9(c), where we present two PL spectra with $V_{\mathrm{BG}} = 0\,\mathrm{V}$, before (blue) and after (red) the PL quenching. More precisely, we measure a spectrum with $V_{\mathrm{BG}} = 0\,\mathrm{V}$ (blue), apply $V_{\mathrm{BG}} = -98\,\mathrm{V}$ to quench the PL (see Fig. 8.6). Then, we apply $V_{\mathrm{BG}} = 0\,\mathrm{V}$ again and measure a new spectrum (red). The blue and red curves, in Fig. 8.9(c), differ only by 14 %, which suggests that the PL quenching is reversible.

The three points raised above are important to understand the main mechanism of the PL quenching. In section 6.3, we approached five mechanisms that may generate this effect. Now, we try to argue which one better describes our results. The (I) thermal dissociation process may be irrelevant in our case, as we do all measurements in cryogenic temperature.

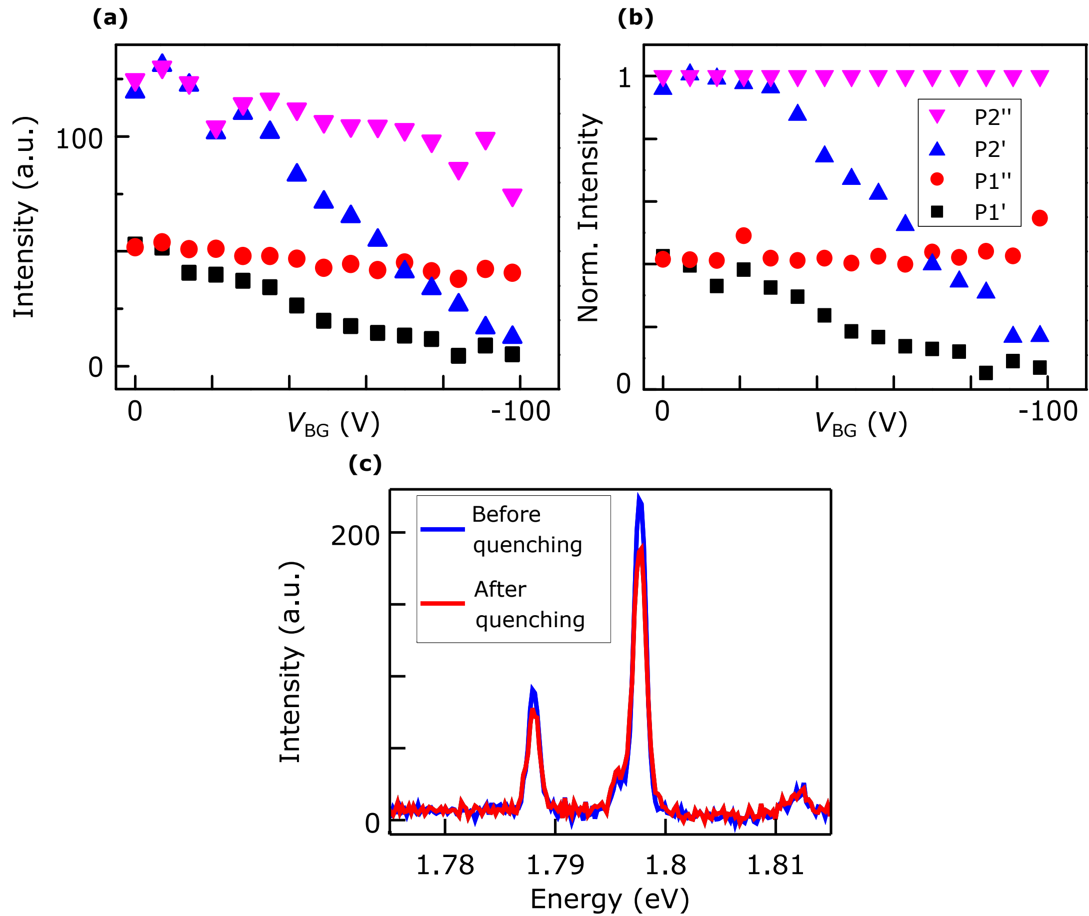

Figure 8.9: **PL intensity as a function of the gate voltage**. **(a)**, intensity in absolute units. **(b)**, normalized intensity relative to the P2" peak. **(c)**, PL spectra with $V_{\mathrm{BG}} = 0\,\mathrm{V}$ before (blue) and after (red) the PL quenching. To obtain the PL quenching we apply $V_{\mathrm{BG}} = -98\,\mathrm{V}$. For these measurements we use the 2.7 eV (457 nm) laser, $T = 80\,\mathrm{K}$, and fluence of 12 mW/μm^2. We use a spectrometer in the single mode with 600 g/mm grating.

In a moment we elaborate about the (II) ionization via electric field. Unfortunately, we do not have enough experiments to investigate the (III) field-induced enhancement of the non-radiative portion of exciton recombination and the (IV) change in radiative lifetime induced by electric field mechanisms. For the (IV) mechanism, we would have to measure the lifetime while applying an electric field, which is quite hard to do in our setup. The (V) impact ionization by field accelerated electrons is unlikely to occur, as our system is an insulator which there are no free charges to flow and ionize the defects. Furthermore, generally the reference [116, 120] use low electric fields to observe this effect ($E \sim 1 - 10\,\mathrm{mV/m}$).

By elimination, we believe that the (II) ionization via electric field is the most probable mechanism that describes the results. Some issues also corroborates with the mechanism II. Recall that we use ultra-large electric fields ($E \sim \mathrm{GV/m}$), which is predicted to allow field ionization [119]. Also important, our quenching effect is reversible similarly to the reference [117, 118], which quenching mechanism is the ionization via electric field. At last, our PL is probably due to deep defect mid-gap states, which means that the charges are trapped in these states, see Fig. 8.5. In this way, one of the few possible ways to ionize them is by using a strong electric field or either by a simultaneous application of electric field and photon absorption. However, we do not discard the mechanisms III and IV completely, as we do not have enough measurements for this purpose.

We can not quench the P2" and P1" peaks completely using large electric fields in the $V_{\mathrm{BG}} < 0\,\mathrm{V}$ regime, see Fig. 8.7. On the other hand, in the same situation, we quench the P2' and P1' peaks. Consider that the P2" and P1" peaks have electric dipole moments contrary to the field for $V_{\mathrm{BG}} < 0\,\mathrm{V}$, see Fig. 8.8. On the other hand, the P2' and P1' peaks have electric dipoles that are in the same direction of the electric field for $V_{\mathrm{BG}} < 0\,\mathrm{V}$. By looking at Fig. 8.7, we observe that these results reverts in the $V_{\mathrm{BG}} > 0\,\mathrm{V}$ regime. In this case, large electric fields quench the P2" and P1" peaks instead of the P2' and P1' peaks. We interpret these issues by looking at the potential energy of the electric dipole, which is $U = -\vec{p} \cdot \vec{E}$. From this expression, the potential energy is maximum when the dipole is anti-parallel to the field and is minimum when they are aligned with each other. Based on these simple assumptions and in our results, we conclude that the electric dipole offers maximum resistance to the field ionization if it is anti-parallel to the field. These resistance avoids the quenching of the P2" and P1" peaks in Fig. 8.9(a). On the other hand, if the electric dipole is aligned to the field, it offers minimum resistance to the field ionization. In this case, large electric fields quench the P2' and P1' peaks almost completely, see Fig. 8.9(a).

The quenching of the PL peaks is interesting for photon switching applications. Also, obtaining an electrically controlled photon switch is relevant for designing on-chip optoelectronic structures. Now, we show that it is possible to use a talc device for photon switching applications. For this purpose, we do a confocal PL imaging of our device with an applied electric field, see Fig. 8.10. Fig. 8.10(a) shows the optical image of our device and the red square outlines the region that we do the confocal imaging. To clarify that our device can work as a photon switch, we plot in Fig. 8.10(b) two PL spectra with $V_{BG} = 0\,V$ (black) and $V_{BG} = -98\,V$ (red). If we manage to filter the blue region in Fig. 8.10(b), we can measure a high and low PL signals with $V_{BG} = 0\,V$ and $V_{BG} = -98\,V$, respectively. As a matter of fact, this process is the base mechanism of a photon switch.

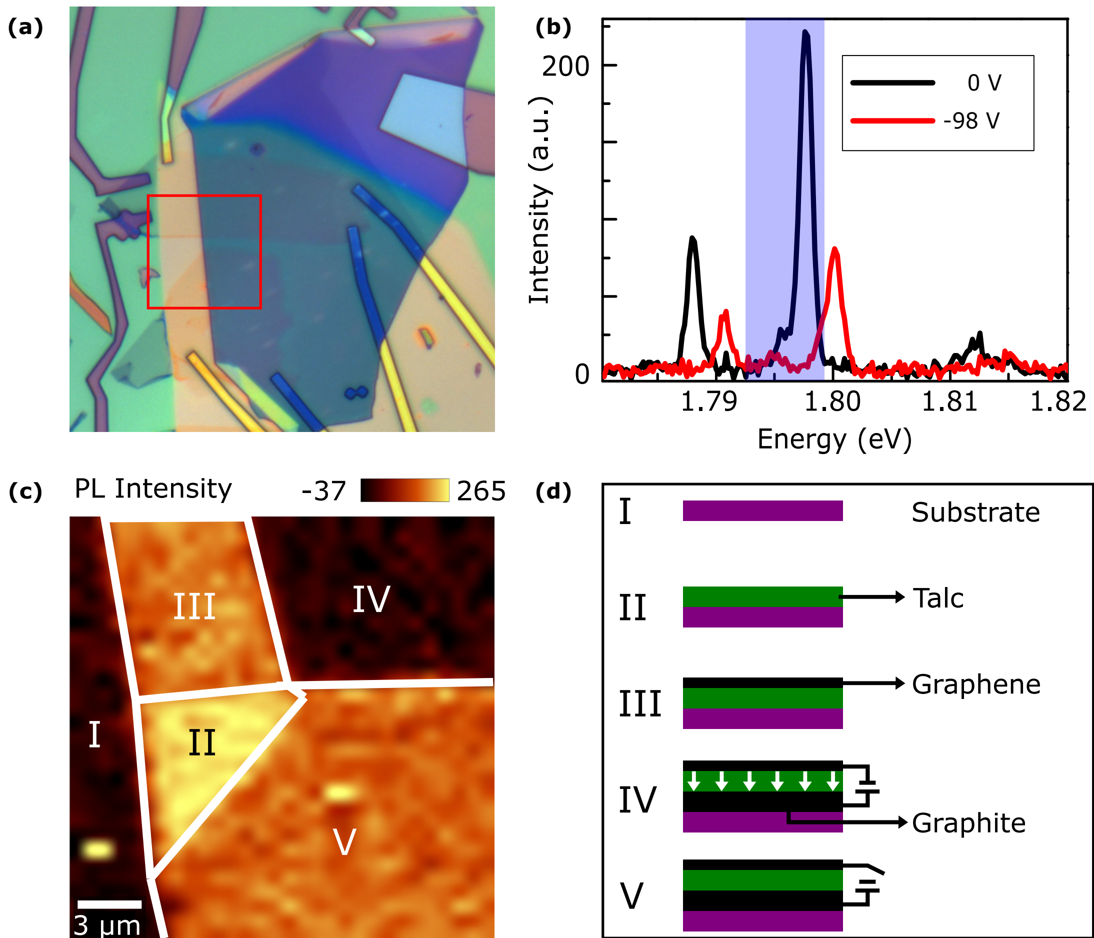

Figure 8.10: **Prospects of an electrical photon switch application**. **(a)**, optical image of our device. The red square delimits the region that we do the confocal PL image measurements. **(b)**, comparing the PL spectra of talc for $V_{BG}= 0\,V$ and $V_{BG}= -98\,V$. The blue region delimits the region of the spectrum that we filter in the confocal PL image measurements. **(c)**, confocal PL image with $V_{BG} = -70\,V$. For these measurements we use the 2.7 eV (457 nm) laser, $T= 80\,K$ and fluence of 12 mW/μm^2. We use a spectrometer in the single mode with 600 g/mm grating. **(d)**, description of the regions of figure **(c)**.

Fig. 8.10(c) shows the confocal PL image with $V_{BG} = -70\,V$ applied in graphite and by filtering the blue region of the spectra in Fig. 8.10(b). We need to describe each of the highlighted regions in Fig. 8.10(c) to understand what information this figure shows. The

region I is the substrate, that does not emit any PL. In Fig. 8.10(d), a purple rectangle represents the substrate. The region II is talc that emits PL with high intensity. In Fig. 8.10(d), a green rectangle represents talc. The region III corresponds to the stacking of few-layer graphene on top of talc, see Fig. 8.10(d). The region III emits a PL, but not so strong as in region II. The reason for the weaker intensity in region III is that the few-layer graphene absorbs some photons. In Fig. 8.10(d), a thin black rectangle represents the graphene. To elucidate the difference between the regions IV and V, first, we shall point out that in Fig. 8.10(a) there are two few-layer graphene flakes on top of talc, which in turn is partially on the graphite flake. The top graphene flake is grounded, while the bottom graphene flake is floating. So, we expect that there is an applied electric field in the talc region that is beneath the top graphene and above the graphite flake. In contrast, there is no electric field in the region beneath the bottom graphene.

The region IV in Fig. 8.7(c), where there is a robust suppression of the PL, corresponds to the specific area of the top graphene which is on top of the talc/graphite heterostructure (see also Fig. 8.7(d), where a thick black rectangle represents the graphite). The color of the IV region is similar to the region I (substrate), which means that their PL intensities are identical (close to zero). On the other hand, region V corresponds to the particular area of the bottom graphene which is on top of the talc/graphite heterostructure. The region V emits a PL, with an intensity represented by a color that is identical to the region III. However, the region III does not have graphite beneath talc. In short, the PL quenching is observed only in the region IV, where there is an applied electric field. There is an electric field applied in the region IV, because it has a grounded graphene on top of talc, and an applied $V_{\mathrm{BG}} = -70\,\mathrm{V}$ on the graphite beneath it. Instead, the other regions do not show any significant quenching, including the region V that has a similar structure to the region IV. Comparing these similar regions, where IV and V have low and high PL signals, respectively, the only difference between them is that region IV has a grounded graphene (which allows an electric field application), while region V has a floating graphene (which prevents the electric field application). In conclusion, these results suggest that the electric field application can lead to a photon switching application in our devices. Moreover, by comparing the PL intensities of different regions of the talc device in Fig. 8.10, we discard artifacts that would decrease the PL intensity.

Chapter 9

Partial conclusions

In part II of this thesis, we studied the electric-induced modifications of the optical emission in layered talc devices, that unraveled Stark splitting and photoluminescence quenching effects. We measured an optical spectrum with narrow peaks by exciting talc with photon energies smaller than its bandgap energy, a subgap excitation. By presenting a laser energy dependence of the measured spectrum, we confirmed that it is due to a photoluminescence mechanism. Furthermore, the intensity of the photoluminescence followed a sublinear behavior with laser power. We argued that the features of the measured photoluminescence spectrum are similar to atomic emissions. We also pointed out that the observed atomic-like emissions are probably due to the photoexcitation of defect states in talc. By applying transverse electric fields in this material, we could modify the energies and intensities of the emissions. We attributed the splitting of the energies to a linear Stark effect. By inspecting this phenomenon, we could evaluate the dipole moments of the defects. Combining these issues with density functional theory calculations, we argued that Fe impurities substituting Si sites in talc would explain the experimental results. We had also investigated the physical mechanisms that can quench photoluminescence, and we concluded that the ionization via electric field might be the mechanism responsible for the photoluminescence quenching in the results. We also connected the Stark splitting and photoluminescence quenching effects, by showing that we did (did not) quench photoluminescence peaks which dipole moments were aligned parallel (antiparallel) to the field. Finally, we pointed a direction toward the implementation of the photoluminescence quenching effect in photon switching devices. Our work unravels impressive optoelectronic effects in the recent discovered 2D talc, and show interesting possibilities for implementing talc in optical devices.

Chapter 10

General conclusions

In this thesis, we studied optoelectronic properties of 2D materials. By applying electric fields in MoS_2 and talc devices, we modified their absorption and emission properties, respectively, unraveling interesting possibilities. The influence of electric field applications in MoS_2 transistors generated two optoelectronic effects: the electric-induced separation of photoexcited carriers in MoS_2, a photocurrent effect, and a photoinduced charge-trapping at the gate-insulator interface of the MoS_2 transistor, a photodoping effect. In talc devices, for the first time, we investigated atomic-like emissions under the influence of electric fields. In these systems, the field application controlled the energies, by a linear Stark effect, and the intensities, through a photoluminescence quenching effect, of the emissions. We made efforts to understand and model the observed optoelectronic phenomena. In MoS_2, we developed a physical model based on the combined actions of photon absorptions and electric field applications that trap holes in the gate-insulator interface of the transistor. We supported this model with experiments and extrapolated our results to other transistors. In talc devices, the inspection of the Stark effect combined with density functional calculations helped us to understand the atomic-like emissions. We argued that the defect states that generate these emissions are due to the replacement of Fe impurities in the Si sites of the monolayer talc. We have also investigated the physical mechanisms that generate photoluminescence quenching. We concluded that the ionization via field is the most reasonable mechanism that can explain our results. We also showed interesting applications of the optoelectronic effects. In MoS_2, we used the electric-control of the photodoping effect to apply MoS_2 in photomemory devices, with gate-tunability properties, high memory on/off ratio up to 10^6, and ultra-high memory retention percentage up to 50% after ten years. We had also exposed that the photodoping effect controls the photocurrent generation in MoS_2 spatially. For talc devices, we deliberated that the strong manipulation of the emission properties of talc with

electric fields can lead to applications in electro-optic modulators. In conclusion, our work makes advances in fields of science and technology, unraveling novel and exciting possibilities to study and control the optoelectronics of 2D materials.

List of publications

Refereed journal publications

1. **Andreij C. Gadelha**; Alisson R. Cadore; Kenji Watanabe; Takashi Taniguchi; Ana M. de Paula; Leandro Malard; Rodrigo G. Lacerda; Leonardo C. Campos. “Gate-tunable non-volatile photo-memory effect in MoS_2 transistors.” *2D Materials* 6, 025036, 2019.

2. G. S. N. Eliel; M. V. O. Moutinho; **A. C. Gadelha**; A. Righi; L. C. Campos; H. B. Ribeiro; Po-Wen Chiu; K. Watanabe; T. Taniguchi; P. Puech, M. Paillet; T. Michel; P. Venezuela; M. A. Pimenta. “Intralayer and interlayer electron-phonon interactions in twisted graphene heterostructures.” *Nature Communications* 9 (1221), 2018.

3. Thales F. D. Fernandes; **Andreij C. Gadelha**; Ana P. M. Barboza; Roberto M. Paniago; Leonardo C. Campos; Paulo S. Soares Guimarães; Pierre-Louis de Assis; Bernardo R. A. Neves. “Robust nanofabrication of monolayer MoS_2 islands with strong photoluminescence enhancement via local anodic oxidation.” *2D Materials* 5 (2), 025018, 2018.

4. Natália P. Rezende; Alisson R. Cadore; **Andreij C. Gadelha**; Cíntia L. Pereira; Vinícius Ornelas; Kenji Watanabe; Takashi Taniguchi; André S. Ferlauto; Angelo Malachias; Leonardo C. Campos; Rodrigo G. Lacerda. “Probing the Electronic Properties of Monolayer MoS_2 via Interaction with Molecular Hydrogen.” *Adv. Electron. Mater.* 5, 1800591, 2019.

5. C. L. Pereira; A. R. Cadore; N. P. Rezende; **A. Gadelha**; E. A. Soares; H. Chacham; L. C. Campos; R. G. Lacerda. “Reversible doping of graphene field effect transistors by molecular hydrogen: the role of the metal/graphene interface.” *2D Materials* 6, 025037, 2019.

6. Rafael N. Gontijo; **Andreij Gadelha**; Orlando J. Silveira; Bruno R. Carvalho; Ricardo W. Nunes; Leonardo C. Campos; Marcos A. Pimenta; Ariete Righi; Cristiano Fantini. “Temperature dependence of the double-resonance Raman bands in monolayer MoS_2.” Submitted, *Journal of Raman Spectroscopy*, 2019.

Unpublished papers

1. **Andreij C. Gadelha**; *et al.* “Controlling MoS_2 photocurrent via a local photodoping effect.” In preparation, 2019.

2. **Andreij C. Gadelha**; *et al.* “Electric-induced stark splitting and quenching of defect emissions in layered talc.” In preparation, 2019.

3. **Andreij C. Gadelha**; *et al.* “Atomic-like emission from magnetic defects in 2D talc.” In preparation, 2019.

4. Rodrigo Almeida; **Andreij C. Gadelha**; *et al.* “Electronic transport through MoS_2 devices: from ohmic contact to Schottky-like Behavior.” In preparation, 2019.

5. S. Souza; Eliel Gomes; **Andreij C. Gadelha**; *et al.* “Laser exposure dependent raman and photoluminescence response in MoS_2.” In preparation, 2019.

International conference

Oral presentation

1. APS, March meeting 2018. Gate-tunable photo-memory effect in MoS_2 transistors. Los Angeles, USA, 2018.

2. XXXVIII Encontro Nacional de Fisica da Materia Condensada. Single-Layer MoS_2 Photodetectors. Brazil, 2015.

Poster presentation

1. NT17. Photo-Doping and Photo-Memory Effect in MoS_2 Transistors. Brazil, 2017.

2. Graphene Brazil 2013. Few-Layer Molybdenum Disulfide Field Effect Based Transistors. Buzios, Brazil, 2013.

Highlights

1. Featured paper: Writing data into ultrathin materials. *Brazilian Materials Research Society bulletin*, 80th edition, 2019. https://www.sbpmat.org.br/en/artigo-em-destaque-gravando-dados-em-materiais-ultrafinos/. Accessed: 2019-05-09.

Bibliography

[1] Freddy Adams and Carlo Barbante. Chapter 4 - nanotechnology and analytical chemistry. In Freddy Adams and Carlo Barbante, editors, *Chemical Imaging Analysis*, volume 69 of *Comprehensive Analytical Chemistry*, pages 125 – 157. Elsevier, 2015.

[2] Optoelectronics. https://www.rp-photonics.com/optoelectronics.html. Accessed: 2019-03-18.

[3] Mark Fox. *Optical Properties of Solids.* Oxford University Press, 2010.

[4] Sajedeh Manzeli, Dmitry Ovchinnikov, Diego Pasquier, Oleg V. Yazyev, and Andras Kis. 2D transition metal dichalcogenides. *Nature Reviews Materials*, 2:17033–, June 2017.

[5] Rudren Ganatra and Qing Zhang. Few-layer MoS_2: A promising layered semiconductor. *ACS Nano*, 8(5):4074–4099, 2014. PMID: 24660756.

[6] Qing Hua Wang, Kourosh Kalantar-Zadeh, Andras Kis, Jonathan N. Coleman, and Michael S. Strano. Electronics and optoelectronics of two-dimensional transition metal dichalcogenides. *Nature Nanotechnology*, 7:699–, November 2012.

[7] Matthew J. Allen, Vincent C. Tung, and Richard B. Kaner. Honeycomb carbon: A review of graphene. *Chem. Rev.*, 110(1):132–145, January 2010.

[8] T. Dvir, F. Massee, L. Attias, M. Khodas, M. Aprili, C. H. L. Quay, and H. Steinberg. Spectroscopy of bulk and few-layer superconducting $NbSe_2$ with van der waals tunnel junctions. *Nature Communications*, 9(1):598–, 2018.

[9] Dean C. R., Young A. F., MericI., Lee C., Wang L., Sorgenfrei S., Watanabe K., Taniguchi T., Kim P., Shepard K. L., and Hone J. Boron nitride substrates for high-quality graphene electronics. *Nat Nano*, 5(10):722–726, October 2010.

[10] Bevin Huang, Genevieve Clark, Dahlia R. Klein, David MacNeill, Efrén Navarro-Moratalla, Kyle L. Seyler, Nathan Wilson, Michael A. McGuire, David H. Cobden, Di Xiao, Wang Yao, Pablo Jarillo-Herrero, and Xiaodong Xu. Electrical control of 2D magnetism in bilayer CrI_3. *Nature Nanotechnology*, 13(7):544–548, 2018.

[11] F. Withers, O. Del Pozo-Zamudio, A. Mishchenko, A. P. Rooney, A. Gholinia, K. Watanabe, T. Taniguchi, S. J. Haigh, A. K. Geim, A. I. Tartakovskii, and K. S.

Novoselov. Light-emitting diodes by band-structure engineering in van der waals heterostructures. *Nature Materials*, 14:301–, February 2015.

[12] Feifan Yu, Mingxiang Hu, Feiyu Kang, and Ruitao Lv. Flexible photodetector based on large-area few-layer MoS_2. *Progress in Natural Science: Materials International*, 28(5):563 – 568, 2018.

[13] Oriol Lopez-Sanchez, Dominik Lembke, Metin Kayci, Aleksandra Radenovic, and Andras Kis. Ultrasensitive photodetectors based on monolayer MoS_2. *Nat Nano*, 8(7):497–501, July 2013.

[14] K. F. Mak, K. L. McGill, J. Park, and P. L. McEuen. The valley hall effect in MoS_2 transistors. *Science*, 344(6191):1489–1492, 2014.

[15] Ananias B Alencar, Ana Paula M Barboza, Bráulio S Archanjo, Helio Chacham, and Bernardo R A Neves. Experimental and theoretical investigations of monolayer and few-layer talc. *2D Materials*, 2(1):015004, feb 2015.

[16] B. Radisavljevic, A. Radenovic, J. Brivio, V. Giacometti, and A. Kism. Single-layer MoS_2 transistors. *Nat Nano*, 6(3):147–150, March 2011.

[17] Manish Chhowalla, Hyeon Suk Shin, Goki Eda, Lain-Jong Li, Kian Ping Loh, and Hua Zhang. The chemistry of two-dimensional layered transition metal dichalcogenide nanosheets. *Nat Chem*, 5(4):263–275, April 2013.

[18] A. Kuc, N. Zibouche, and T. Heine. Influence of quantum confinement on the electronic structure of the transition metal sulfide TS_2. *Phys. Rev. B*, 83:245213, Jun 2011.

[19] Andrea Splendiani, Liang Sun, Yuanbo Zhang, Tianshu Li, Jonghwan Kim, Chi-Yung Chim, Giulia Galli, and Feng Wang. Emerging photoluminescence in monolayer MoS_2. *Nano Letters*, 10(4):1271–1275, 2010. PMID: 20229981.

[20] Jason K. Ellis, Melissa J. Lucero, and Gustavo E. Scuseria. The indirect to direct band gap transition in multilayered MoS_2 as predicted by screened hybrid density functional theory. *Applied Physics Letters*, 99(26):–, 2011.

[21] Eugene S. Kadantsev and Pawel Hawrylak. Electronic structure of a single MoS_2 monolayer. *Solid State Communications*, 152(10):909 – 913, 2012.

[22] Tawinan Cheiwchanchamnangij and Walter R. L. Lambrecht. Quasiparticle band structure calculation of monolayer, bilayer, and bulk MoS_2. *Phys. Rev. B*, 85:205302, May 2012.

[23] Ashwin Ramasubramaniam. Large excitonic effects in monolayers of molybdenum and tungsten dichalcogenides. *Phys. Rev. B*, 86:115409, Sep 2012.

[24] Kin Fai Mak, Changgu Lee, James Hone, Jie Shan, and Tony F. Heinz. Atomically thin MoS_2: A new direct-gap semiconductor. *Phys. Rev. Lett.*, 105:136805, Sep 2010.

[25] Jason S. Ross, Sanfeng Wu, Hongyi Yu, Nirmal J. Ghimire, Aaron M. Jones, Grant Aivazian, Jiaqiang Yan, David G. Mandrus, Di Xiao, Wang Yao, and Xiaodong Xu. Electrical control of neutral and charged excitons in a monolayer semiconductor. *Nat Commun*, 4:1474–, February 2013.

[26] Hyun Seok Lee, Min Su Kim, Hyun Kim, and Young Hee Lee. Identifying multiexcitons in MoS_2 monolayers at room temperature. *Phys. Rev. B*, 93:140409, Apr 2016.

[27] Jason W. Christopher, Bennett B. Goldberg, and Anna K. Swan. Long tailed trions in monolayer MoS_2: Temperature dependent asymmetry and resulting red-shift of trion photoluminescence spectra. *Scientific Reports*, 7(1):14062–, 2017.

[28] Kin Fai Mak, Keliang He, Changgu Lee, Gwan Hyoung Lee, James Hone, Tony F. Heinz, and Jie Shan. Tightly bound trions in monolayer MoS_2. *Nature Materials*, 12:207–, December 2012.

[29] Dominik Lembke, Simone Bertolazzi, and Andras Kis. Single-layer MoS_2 electronics. *Accounts of Chemical Research*, 48(1):100–110, 2015. PMID: 25555202.

[30] Riccardo Frisenda, Aday J. Molina-Mendoza, Thomas Mueller, Andres Castellanos-Gomez, and Herre S. J. van der Zant. Atomically thin p-n junctions based on two-dimensional materials. *Chem. Soc. Rev.*, 47(9):3339–3358, 2018.

[31] Jae Yoon Lee, Jun-Hwan Shin, Gwan-Hyoung Lee, and Chul-Ho Lee. Two-dimensional semiconductor optoelectronics based on van der waals heterostructures. *Nanomaterials (Basel, Switzerland)*, 6(11):193–, October 2016.

[32] He Tian, Matthew L. Chin, Sina Najmaei, Qiushi Guo, Fengnian Xia, Han Wang, and Madan Dubey. Optoelectronic devices based on two-dimensional transition metal dichalcogenides. *Nano Research*, 9(6):1543–1560, Jun 2016.

[33] Xu Cui, Gwan-Hyoung Lee, Young Duck Kim, Ghidewon Arefe, Pinshane Y. Huang, Chul-Ho Lee, Daniel A. Chenet, Xian Zhang, Lei Wang, Fan Ye, Filippo Pizzocchero, Bjarke S. Jessen, Kenji Watanabe, Takashi Taniguchi, David A. Muller, Tony Low, Philip Kim, and James Hone. Multi-terminal transport measurements of MoS_2 using a van der waals heterostructure device platform. *Nat Nano*, 10(6):534–540, June 2015.

[34] D. Liu, Y. Guo, L. Fang, and J. Robertson. Sulfur vacancies in monolayer MoS_2 and its electrical contacts. *Applied Physics Letters*, 103(18):–, 2013.

[35] Péter Vancsó, Gábor Zsolt Magda, János Pető, Ji-Young Noh, Yong-Sung Kim, Chanyong Hwang, László P. Biró, and Levente Tapasztó. The intrinsic defect structure of exfoliated MoS_2 single layers revealed by scanning tunneling microscopy. *Scientific Reports*, 6:29726–, July 2016.

[36] Yijin Zhang, Jianting Ye, Yusuke Matsuhashi, and Yoshihiro Iwasa. Ambipolar MoS_2 thin flake transistors. *Nano Letters*, 12(3):1136–1140, 2012. PMID: 22276648.

[37] Masihhur R. Laskar, Digbijoy N. Nath, Lu Ma, Edwin W. Lee, Choong Hee Lee, Thomas Kent, Zihao Yang, Rohan Mishra, Manuel A. Roldan, Juan-Carlos Idrobo, Sokrates T. Pantelides, Stephen J. Pennycook, Roberto C. Myers, Yiying Wu, and Siddharth Rajan. p-type doping of MoS_2 thin films using Nb. *Applied Physics Letters*, 104(9):–, 2014.

[38] Steven Chuang, Corsin Battaglia, Angelica Azcatl, Stephen McDonnell, Jeong Seuk Kang, Xingtian Yin, Mahmut Tosun, Rehan Kapadia, Hui Fang, Robert M. Wallace, and Ali Javey. MoS_2 p-type transistors and diodes enabled by high work function MoOx contacts. *Nano Letters*, 14(3):1337–1342, 2014. PMID: 24568656.

[39] Marcio Fontana, Tristan Deppe, Anthony K. Boyd, Mohamed Rinzan, Amy Y. Liu, Makarand Paranjape, and Paola Barbara. Electron-hole transport and photovoltaic effect in gated MoS_2 schottky junctions. *Sci. Rep.*, 3:–, April 2013.

[40] Jingli Wang, Qian Yao, Chun-Wei Huang, Xuming Zou, Lei Liao, Shanshan Chen, Zhiyong Fan, Kai Zhang, Wei Wu, Xiangheng Xiao, Changzhong Jiang, and Wen-Wei Wu. High mobility MoS_2 transistor with low schottky barrier contact by using atomic thick $h-BN$ as a tunneling layer. *Adv. Mater.*, 28(37):8302–8308, October 2016.

[41] Xu Cui, En-Min Shih, Luis A. Jauregui, Sang Hoon Chae, Young Duck Kim, Baichang Li, Dongjea Seo, Kateryna Pistunova, Jun Yin, Ji-Hoon Park, Heon-Jin Choi, Young Hee Lee, Kenji Watanabe, Takashi Taniguchi, Philip Kim, Cory R. Dean, and James C. Hone. Low-temperature ohmic contact to monolayer MoS_2 by van der waals bonded $Co/h-BN$ electrodes. *Nano Lett.*, 17(8):4781–4786, August 2017.

[42] Quoc An Vu, Yong Seon Shin, Young Rae Kim, Van Luan Nguyen, Won Tae Kang, Hyun Kim, Dinh Hoa Luong, Il Min Lee, Kiyoung Lee, Dong-Su Ko, Jinseong Heo, Seongjun Park, Young Hee Lee, and Woo Jong Yu. Two-terminal floating-gate memory with van der waals heterostructures for ultrahigh on/off ratio. *Nature Communications*, 7:12725–, September 2016.

[43] Ruiqing Cheng, Feng Wang, Lei Yin, Kai Xu, Tofik Ahmed Shifa, Yao Wen, Xueying Zhan, Jie Li, Chao Jiang, Zhenxing Wang, and Jun He. Multifunctional tunneling devices based on $graphene/h-BN/MoSe_2$ van der waals heterostructures. *Applied Physics Letters*, 110(17):173507, 2017.

[44] Enze Zhang, Weiyi Wang, Cheng Zhang, Yibo Jin, Guodong Zhu, Qingqing Sun, David Wei Zhang, Peng Zhou, and Faxian Xiu. Tunable charge-trap memory based on few-layer MoS_2. *ACS Nano*, 9(1):612–619, 2015. PMID: 25496773.

[45] Simone Bertolazzi, Daria Krasnozhon, and Andras Kis. Nonvolatile memory cells based on MoS_2/graphene heterostructures. *ACS Nano*, 7(4):3246–3252, 2013. PMID: 23510133.

[46] Myung Hun Woo, Byung Chul Jang, Junhwan Choi, Khang June Lee, Gwang Hyuk Shin, Hyejeong Seong, Sung Gap Im, and Sung-Yool Choi. Low-power nonvolatile

charge storage memory based on MoS_2 and an ultrathin polymer tunneling dielectric. *Advanced Functional Materials*, pages 1703545–n/a. 1703545.

[47] Dong Li, Mingyuan Chen, Zhengzong Sun, Peng Yu, Zheng Liu, Pulickel M. Ajayan, and Zengxing Zhang. Two-dimensional non-volatile programmable p-n junctions. *Nature Nanotechnology*, 12:901–, June 2017.

[48] Marco M. Furchi, Dmitry K. Polyushkin, Andreas Pospischil, and Thomas Mueller. Mechanisms of photoconductivity in atomically thin MoS_2. *Nano Letters*, 14(11):6165–6170, 2014. PMID: 25299515.

[49] Michele Buscema, Maria Barkelid, Val Zwiller, Herre S. J. van der Zant, Gary A. Steele, and Andres Castellanos-Gomez. Large and tunable photothermoelectric effect in single-layer MoS_2. *Nano Letters*, 13(2):358–363, 2013. PMID: 23301811.

[50] Joeson Wong, Deep Jariwala, Giulia Tagliabue, Kevin Tat, Artur R. Davoyan, Michelle C. Sherrott, and Harry A. Atwater. High photovoltaic quantum efficiency in ultrathin van der waals heterostructures. *ACS Nano*, 11(7):7230–7240, July 2017.

[51] Evgeniy Ponomarev, Ignacio Gutiérrez-Lezama, Nicolas Ubrig, and Alberto F. Morpurgo. Ambipolar light-emitting transistors on chemical vapor deposited monolayer MoS_2. *Nano Lett.*, 15(12):8289–8294, December 2015.

[52] Rui Cheng, Dehui Li, Hailong Zhou, Chen Wang, Anxiang Yin, Shan Jiang, Yuan Liu, Yu Chen, Yu Huang, and Xiangfeng Duan. Electroluminescence and photocurrent generation from atomically sharp $WoSe_2/MoS_2$ heterojunction p–n diodes. *Nano Lett.*, 14(10):5590–5597, October 2014.

[53] Juwon Lee, Sangyeon Pak, Young-Woo Lee, Yuljae Cho, John Hong, Paul Giraud, Hyeon Suk Shin, Stephen M. Morris, Jung Inn Sohn, SeungNam Cha, and Jong Min Kim. Monolayer optical memory cells based on artificial trap-mediated charge storage and release. *Nature Communications*, 8:14734–, March 2017.

[54] Yueh-Chun Wu, Cheng-Hua Liu, Shao-Yu Chen, Fu-Yu Shih, Po-Hsun Ho, Chun-Wei Chen, Chi-Te Liang, and Wei-Hua Wang. Extrinsic origin of persistent photoconductivity in monolayer MoS_2 field effect transistors. *Scientific Reports*, 5:11472–, June 2015.

[55] Zongyou Yin, Hai Li, Hong Li, Lin Jiang, Yumeng Shi, Yinghui Sun, Gang Lu, Qing Zhang, Xiaodong Chen, and Hua Zhang. Single-layer MoS_2 phototransistors. *ACS Nano*, 6(1):74–80, 2012. PMID: 22165908.

[56] Bastian Miller, Eric Parzinger, Anna Vernickel, Alexander W. Holleitner, and Ursula Wurstbauer. Photogating of mono- and few-layer MoS_2. *Applied Physics Letters*, 106(12):122103, 2015.

[57] Andreij de Carvalho Gadelha. Single-layer MoS_2 photodetectors. Master's thesis, Federal University of Minas Gerais, 2015.

[58] Hongyan Shi, Rusen Yan, Simone Bertolazzi, Jacopo Brivio, Bo Gao, Andras Kis, Debdeep Jena, Huili Grace Xing, and Libai Huang. Exciton dynamics in suspended monolayer and few-layer MoS_2 2D crystals. *ACS Nano*, 7(2):1072–1080, February 2013.

[59] M. F. Khan, M. W. Iqbal, M. Z. Iqbal, M. A. Shehzad, Y. Seo, and Jonghwa Eom. Photocurrent response of MoS_2 field-effect transistor by deep ultraviolet light in atmospheric and N_2 gas environments. *ACS Applied Materials & Interfaces*, 6(23):21645–21651, 2014. PMID: 25409490.

[60] Sujoy Ghosh, Andrew Winchester, Baleeswaraiah Muchharla, Milinda Wasala, Simin Feng, Ana Laura Elias, M. Bala Murali Krishna, Takaaki Harada, Catherine Chin, Keshav Dani, Swastik Kar, Mauricio Terrones, and Saikat Talapatra. Ultrafast intrinsic photoresponse and direct evidence of sub-gap states in liquid phase exfoliated MoS_2 thin films. *Scientific Reports*, 5:11272–, July 2015.

[61] Antonio Di Bartolomeo, Luca Genovese, Tobias Foller, Filippo Giubileo, Giuseppe Luongo, Luca Croin, Shi-Jun Liang, L K Ang, and Marika Schleberger. Electrical transport and persistent photoconductivity in monolayer MoS_2 phototransistors. *Nanotechnology*, 28(21):214002, 2017.

[62] https://hblok.net/blog/posts/2013/02/13/historical-cost-of-computer-memory-and-storage. Accessed: 2017-04-15.

[63] Historical cost of computer memory and storage. https://hblok.net/blog/posts/2017/12/17/historical-cost-of-computer-memory-and-storage-4/. Accessed: 2019-03-12.

[64] The first hard drive was announced in 1956. http://factmyth.com/factoids/the-first-hard-drive-was-announced-in-1956/. Accessed: 2019-03-12.

[65] Samsung força a amizade e enfia 16 tb em um ssd. https://meiobit.com/324079/samsung-pm1633a-ssd-com-16-terabytes/. Accessed: 2019-03-12.

[66] Cd-r (compact disc, recordable). https://searchstorage.techtarget.com/definition/CD-R. Accessed: 2019-03-12.

[67] Min Sup Choi, Gwan-Hyoung Lee, Young-Jun Yu, Dae-Yeong Lee, Seung Hwan Lee, Philip Kim, James Hone, and Won Jong Yoo. Controlled charge trapping by molybdenum disulphide and graphene in ultrathin heterostructured memory devices. *Nature Communications*, 4:1624–, March 2013.

[68] Yu Wang, Erfu Liu, Anyuan Gao, Tianjun Cao, Mingsheng Long, Chen Pan, Lili Zhang, Junwen Zeng, Chenyu Wang, Weida Hu, Shi-Jun Liang, and Feng Miao. Negative photoconductance in van der waals heterostructure-based floating gate phototransistor. *ACS Nano*, 12(9):9513–9520, September 2018.

[69] G. He, H. Ramamoorthy, C.-P. Kwan, Y.-H. Lee, J. Nathawat, R. Somphonsane, M. Matsunaga, A. Higuchi, T. Yamanaka, N. Aoki, Y. Gong, X. Zhang, R. Vajtai, P. M. Ajayan, and J. P. Bird. Thermally assisted nonvolatile memory in monolayer MoS_2 transistors. *Nano Letters*, 16(10):6445–6451, 2016. PMID: 27680095.

[70] Gwang Hyuk Shin, Choong-Ki Kim, Gyeong Sook Bang, Jong Yun Kim, Byung Chul Jang, Beom Jun Koo, Myung Hun Woo, Yang-Kyu Choi, and Sung-Yool Choi. Multilevel resistive switching nonvolatile memory based on MoS_2 nanosheet-embedded graphene oxide. *2D Materials*, 3(3):034002, 2016.

[71] Augustin J. Hong, Emil B. Song, Hyung Suk Yu, Matthew J. Allen, Jiyoung Kim, Jesse D. Fowler, Jonathan K. Wassei, Youngju Park, Yong Wang, Jin Zou, Richard B. Kaner, Bruce H. Weiller, and Kang L. Wang. Graphene flash memory. *ACS Nano*, 5(10):7812–7817, 2011. PMID: 21854056.

[72] Yi Zheng, Guang-Xin Ni, Chee-Tat Toh, Ming-Gang Zeng, Shu-Ting Chen, Kui Yao, and Barbaros Özyilmaz. Gate-controlled nonvolatile graphene-ferroelectric memory. *Applied Physics Letters*, 94(16):163505, 2009.

[73] Brian Standley, Wenzhong Bao, Hang Zhang, Jehoshua Bruck, Chun Ning Lau, and Marc Bockrath. Graphene-based atomic-scale switches. *Nano Letters*, 8(10):3345–3349, 2008. PMID: 18729415.

[74] Xiaomu Wang, Weiguang Xie, Jun Du, Chengliang Wang, Ni Zhao, and Jian-Bin Xu. Graphene/metal contacts: Bistable states and novel memory devices. *Advanced Materials*, 24(19):2614–2619, 2012.

[75] Congli He, Zhiwen Shi, Lianchang Zhang, Wei Yang, Rong Yang, Dongxia Shi, and Guangyu Zhang. Multilevel resistive switching in planar graphene/SiO_2 nanogap structures. *ACS Nano*, 6(5):4214–4221, 2012. PMID: 22519726.

[76] Xiao-Dong Zhuang, Yu Chen, Gang Liu, Pei-Pei Li, Chun-Xiang Zhu, En-Tang Kang, Koon-Gee Noeh, Bin Zhang, Jin-Hui Zhu, and Yong-Xi Li. Conjugated-polymer-functionalized graphene oxide: Synthesis and nonvolatile rewritable memory effect. *Advanced Materials*, 22(15):gropo, 2010.

[77] Andres Castellanos-Gomez, Michele Buscema, Rianda Molenaar, Vibhor Singh, Laurens Janssen, Herre S J van der Zant, and Gary A Steele. Deterministic transfer of two-dimensional materials by all-dry viscoelastic stamping. *2D Materials*, 1(1):011002, 2014.

[78] Changgu Lee, Hugen Yan, Louis E. Brus, Tony F. Heinz, James Hone, and Sunmin Ryu. Anomalous lattice vibrations of single- and few-layer MoS_2. *ACS Nano*, 4(5):2695–2700, 2010. PMID: 20392077.

[79] Hong Li, Qing Zhang, Chin Chong Ray Yap, Beng Kang Tay, Teo Hang Tong Edwin, Aurelien Olivier, and Dominique Baillargeat. From bulk to monolayer MoS_2: Evolution of raman scattering. *Advanced Functional Materials*, 22(7):1385–1390, 2012.

[80] Britton W. H. Baugher, Hugh O. H. Churchill, Yafang Yang, and Pablo Jarillo-Herrero. Intrinsic electronic transport properties of high-quality monolayer and bilayer MoS_2. *Nano Letters*, 13(9):4212–4216, 2013. PMID: 23930826.

[81] S. M. Sze and Kwok K. Ng. *Physics of Semiconductor Devices*. John Wiley & Sons, Inc, 2007.

[82] Dattatray J. Late, Bin Liu, H. S. S. Ramakrishna Matte, Vinayak P. Dravid, and C. N. R. Rao. Hysteresis in single-layer MoS_2 field effect transistors. *ACS Nano*, 6(6):5635–5641, 2012. PMID: 22577885.

[83] Yury Yu Illarionov, Gerhard Rzepa, Michael Waltl, Theresia Knobloch, Alexander Grill, Marco M Furchi, Thomas Mueller, and Tibor Grasser. The role of charge trapping in MoS_2 /SiO_2 and MoS_2/hBN field-effect transistors. *2D Materials*, 3(3):035004, 2016.

[84] A. R. Cadore, E. Mania, K. Watanabe, T. Taniguchi, R. G. Lacerda, and L. C. Campos. Thermally activated hysteresis in high quality graphene/$\mathrm{h-BN}$ devices. *Applied Physics Letters*, 108(23):233101, 2016.

[85] Wenjing Zhang, Jing-Kai Huang, Chang-Hsiao Chen, Yung-Huang Chang, Yuh-Jen Cheng, and Lain-Jong Li. High-gain phototransistors based on a cvd MoS_2 monolayer. *Advanced Materials*, 25(25):3456–3461, 2013.

[86] Ju L., J. Velasco Jr, Huang E., Kahn S., Nosiglia C., Hsin-Zon Tsai, Yang W., Taniguchi T., Watanabe K., Zhang Y., Zhang G., Crommie M., Zettl A., and Wang F. Photoinduced doping in heterostructures of graphene and boron nitride. *Nat Nano*, 9(5):348–352, May 2014.

[87] Young Duck Kim, Myung-Ho Bae, Jung-Tak Seo, Yong Seung Kim, Hakseong Kim, Jae Hong Lee, Joung Real Ahn, Sang Wook Lee, Seung-Hyun Chun, and Yun Daniel Park. Focused-laser-enabled p-n junctions in graphene field-effect transistors. *ACS Nano*, 7(7):5850–5857, 2013. PMID: 23782162.

[88] R. Schlaf, O. Lang, C. Pettenkofer, and W. Jaegermann. Band lineup of layered semiconductor heterointerfaces prepared by van der waals epitaxy: Charge transfer correction term for the electron affinity rule. *Journal of Applied Physics*, 85(5):2732–2753, 1999.

[89] K. S. KRISHNAN and S. C. JAIN. Thermionic constants of graphite. *Nature*, 169(4304):702–703, April 1952.

[90] Yingke Zhou, Timothy Holme, Joe Berry, Timothy R. Ohno, David Ginley, and Ryan O'Hayre. Dopant-induced electronic structure modification of hopg surfaces: Implications for high activity fuel cell catalysts. *The Journal of Physical Chemistry C*, 114(1):506–515, 2010.

[91] Keishi Akada, Tomo o Terasawa, Gaku Imamura, Seiji Obata, and Koichiro Saiki. Control of work function of graphene by plasma assisted nitrogen doping. *Applied Physics Letters*, 104(13):131602, 2014.

[92] Chung-Chiang Wu, Deep Jariwala, Vinod K. Sangwan, Tobin J. Marks, Mark C. Hersam, and Lincoln J. Lauhon. Elucidating the photoresponse of ultrathin MoS_2 field-effect transistors by scanning photocurrent microscopy. *The Journal of Physical Chemistry Letters*, 4(15):2508–2513, 2013.

[93] William Ward and James M. Phillips. Calculated lamellar binding: I. van der waals bonding in talc and pyrophyllite. *Surface Science*, 25(2):379–385, 1971.

[94] Ingrid D. Barcelos, Alisson R. Cadore, Ananias B. Alencar, Francisco C. B. Maia, Edrian Mania, Rafael F. Oliveira, Carlos C. B. Bufon, Ângelo Malachias, Raul O. Freitas, Roberto L. Moreira, and Hélio Chacham. Infrared fingerprints of natural 2d talc and plasmons-phonon coupling in graphene-talc heterostructures. *ACS Photonics*, 5(5):1912–1918, May 2018.

[95] Ananias Borges Alencar. *Estudo por primeiros princípios de propriedades eletrônicas e estruturais de talco e calcogenetos de molibdênio.* PhD thesis, UFMG, 2016.

[96] M.L.M. Rodrigues and R.M.F. Lima. Cleaner production of soapstone in the ouro preto region of brazil: a case study. *Journal of Cleaner Production*, 32:149 – 156, 2012.

[97] N. H. Garcia, M. M. L. Rodrigues, M. M. F. Lima, and R. M. F. Lima. Caracterização de talco purificado de resíduos de pedra sabão. *Holos*, 30:69–77, 2014.

[98] Agnieszka Mierczynska-Vasilev and David A. Beattie. The effect of impurities and cleavage characteristics on talc hydrophobicity and polymer adsorption. *International Journal of Mineral Processing*, 118:34 – 42, 2013.

[99] F. Martin and P. Micoud. The structural formula of talc from the trimouns deposit, pyrenees, france. *The Canadian Mineralogist*, 37:997–1006, 1999.

[100] S. Vedanand, P. Sambasiva Rao, and B. J. Reddy. Spectroscopic investigations on different grade samples of talc. *Radiation Effects and Defects in Solids*, 127(2):169–176, 1993.

[101] Talc r040137. http://rruff.info/talc/R040137. Accessed: 2019-03-18.

[102] Talc. https://celestialearthminerals.com/atlas-of-minerals/talc/. Accessed: 2019-03-18.

[103] Chengxiang Li, Rucheng Wang, Xiancai Lu, and Ming Zhang. Mineralogical characteristics of unusual black talc ores in guangfeng county, jiangxi province, china. *Applied Clay Science*, 74:37 – 46, 2013. Clays and clay minerals: geology, properties and uses.

[104] Talc specimens. http://www.galleries.com/scripts/item.exe?ENLARGE+Minerals+Silicates+Talc+TAL-10. Accessed: 2019-03-18.

[105] E Mania, A B Alencar, A R Cadore, B R Carvalho, K Watanabe, T Taniguchi, B R A Neves, H Chacham, and L C Campos. Spontaneous doping on high quality talc-graphene-hBN van der waals heterostructures. *2D Materials*, 4(3):031008, jul 2017.

[106] F. Jelezko and J. Wrachtrup. Single defect centres in diamond: A review. *phys. stat. sol. (a)*, 203(13):3207–3225, October 2006.

[107] Toan Trong Tran, Kerem Bray, Michael J. Ford, Milos Toth, and Igor Aharonovich. Quantum emission from hexagonal boron nitride monolayers. *Nature Nanotechnology*, 11:37–, October 2015.

[108] Sunny Gupta, Ji-Hui Yang, and Boris I. Yakobson. Two-level quantum systems in two-dimensional materials for single photon emission. *Nano Lett.*, 19(1):408–414, January 2019.

[109] Nae-Man Park, Tae-Youb Kim, Kyung-Hyun Kim, Gun Yong Sung, Baek-Hyun Kim, Seong-Ju Park, Kwan Sik Cho, Jung H. Shin, Jung-Kun Lee, and Michael Nastasi. Effect of amorphous Si quantum-dot size on 1.54 μm luminescence of Er. *Journal of The Electrochemical Society*, 152(6):G445–G447, 2005.

[110] Jeffrey M. Pietryga, Young-Shin Park, Jaehoon Lim, Andrew F. Fidler, Wan Ki Bae, Sergio Brovelli, and Victor I. Klimov. Spectroscopic and device aspects of nanocrystal quantum dots. *Chem. Rev.*, 116(18):10513–10622, September 2016.

[111] D Kaplan, Y Gong, K Mills, V Swaminathan, P M Ajayan, S Shirodkar, and E Kaxiras. Excitation intensity dependence of photoluminescence from monolayers of MoS_2 and WS_2/MoS_2 heterostructures. *2D Materials*, 3(1):015005, jan 2016.

[112] Claude Cohen-Tannoudji, Bernard Diu, and Franck Laloe. *Quantum Mechanics*. Hermann, 2005.

[113] David J. Griffiths. *Introduction to Electrodynamics*. Prentice Hall, 3rd edition, 1999.

[114] Gichang Noh, Daebok Choi, Jin-Hun Kim, Dong-Gil Im, Yoon-Ho Kim, Hosung Seo, and Jieun Lee. Stark tuning of single-photon emitters in hexagonal boron nitride. *Nano Lett.*, 18(8):4710–4715, August 2018.

[115] Chitraleema Chakraborty, Kenneth M. Goodfellow, Sajal Dhara, Anthony Yoshimura, Vincent Meunier, and A. Nick Vamivakas. Quantum-confined stark effect of individual defects in a van der waals heterostructure. *Nano Lett.*, 17(4):2253–2258, April 2017.

[116] W. Bludau and E. Wagner. Impact ionization of excitons in gaas. *Phys. Rev. B*, 13:5410–5414, Jun 1976.

[117] M. Ando and Y. A. Ono. Electro and photoluminescent quenching effects imposed by fieldinduced ionization of the Eu2+ luminescent centers in cas:eu thin films. *Journal of Applied Physics*, 69(10):7225–7230, 1991.

[118] Hao Huang, August Dorn, Gautham P. Nair, Vladimir Bulović, and Moungi G. Bawendi. Bias-induced photoluminescence quenching of single colloidal quantum dots embedded in organic semiconductors. *Nano Letters*, 7(12):3781–3786, 2007. PMID: 18034504.

[119] Daniel F. Blossey. Wannier exciton in an electric field. i. optical absorption by bound and continuum states. *Phys. Rev. B*, 2:3976–3990, Nov 1970.

[120] Helge Weman, Qing-Xiang Zhao, and Bo Monemar. Impact ionization and electric field quenching of photoluminescence in silicon. *Solid-State Electronics*, 31:791–794, 03 1988.

[121] D. G. Purdie, N. M. Pugno, T. Taniguchi, K. Watanabe, A. C. Ferrari, and A. Lombardo. Cleaning interfaces in layered materials heterostructures. *Nature Communications*, 9(1):5387–, 2018.

[122] Alian Wang, John J. Freeman, and Bradley L. Jolliff. Understanding the raman spectral features of phyllosilicates. *J. Raman Spectrosc.*, 46(10):829–845, October 2015.

[123] G. J. Rosasco and J. J. Blaha. Raman microprobe spectra and vibrational mode assignments of talc. *Appl. Spectrosc.*, 34(2):140–144, Mar 1980.

[124] M. Ishii, T. Shimanouchi, and M. Nakahira. Far infra-red absorption spectra of layer silicates. *Inorganica Chimica Acta*, 1:387 – 392, 1967.

[125] Manoj Das, A. Shirasaki, K. P. Nayak, M. Morinaga, Fam Le Kien, and K. Hakuta. Measurement of fluorescence emission spectrum of few strongly driven atoms using an optical nanofiber. *Opt. Express*, 18(16):17154–17164, Aug 2010.